SLAC-R-1065

SEARCHING FOR DWARF SPHEROIDAL GALAXIES AND OTHER GALACTIC DARK MATTER SUBSTRUCTURES WITH THE *FERMI* LARGE AREA TELESCOPE

A DISSERTATION
SUBMITTED TO THE DEPARTMENT OF PHYSICS
AND THE COMMITTEE ON GRADUATE STUDIES
OF STANFORD UNIVERSITY
IN PARTIAL FULFILLMENT OF THE REQUIREMENTS
FOR THE DEGREE OF
DOCTOR OF PHILOSOPHY

Alex Drlica-Wagner
August 2013

SLAC National Accelerator Laboratory, Stanford University, Stanford, California 94039, USA
This material is based upon work supported by the U.S. Department of Energy, Office of Science,
Office of Basic Energy Sciences, under Contract No. DE-AC02-76SF00515.

I certify that I have read this dissertation and that, in my opinion, it is fully adequate in scope and quality as a dissertation for the degree of Doctor of Philosophy.

Elliott Bloom, Primary Adviser

I certify that I have read this dissertation and that, in my opinion, it is fully adequate in scope and quality as a dissertation for the degree of Doctor of Philosophy.

Steven Allen

I certify that I have read this dissertation and that, in my opinion, it is fully adequate in scope and quality as a dissertation for the degree of Doctor of Philosophy.

Stefan Funk

Approved for the Stanford University Committee on Graduate Studies.

Patricia J. Gumport, Vice Provost for Graduate Education

Abstract

Over the past century, it has become clear that about a quarter of the known universe is composed of an invisible, massive component termed "dark matter". Some of the most popular theories of physics beyond the Standard Model suggest that dark matter may be a new fundamental particle that could self-annihilate to produce γ rays. Nearby over-densities in the dark matter halo of our Milky Way present some of the most promising targets for detecting the annihilation of dark matter. We used the Large Area Telescope (LAT) on-board the *Fermi Gamma-ray Space Telescope* to search for γ rays produced by dark matter annihilation in Galactic dark matter substructures. We searched for γ-ray emission coincident with Milky Way dwarf spheroidal satellite galaxies, which trace the most massive Galactic dark matter substructures. We also sought to identify nearby dark matter substructures that lack all astrophysical tracers and would be detectable only through γ-ray emission from dark matter annihilation. We found no conclusive evidence for γ-ray emission from dark matter annihilation, and we set stringent and robust constraints on the dark matter annihilation cross section. While γ-ray searches for dark matter substructure are currently the most sensitive and robust probes of dark matter annihilation, they are just beginning to intersect the theoretically preferred region of dark matter parameter space. Thus, we consider future prospects for increasing the sensitivity of γ-ray searches through improvements to the LAT instrument performance and through upcoming wide-field optical surveys.

Acknowledgments

I consider myself extremely lucky to have had the opportunity to work with the talented and nurturing group of people at KIPAC, SLAC, and Stanford. Firstly, I would like to thank my adviser, Elliott Bloom, for giving me the freedom to choose my own projects and the guidance to help me complete them. I would also like to give a special thanks to Eric Charles, Seth Digel, Louie Strigari, and Matthew Wood; I would have learned far less without their mentorship. The insightful and open scientific community of KIPAC is exemplified by the members of my dissertation committee, Steve Allen, Stefan Funk, and Risa Wechsler; I have benefited tremendously from their input over the years. I could not have hoped for better companions than my fellow graduate students, Alice Allafort, Keith Bechtol, Josh Cogan, Steven Ehlert, Joshua Lande, Adam Mantz, Warit Mitthumsiri, and Paul Simeon. My journey through graduate school would have been very different had I not been accompanied by such great friends. The wonderful environment of KIPAC is made possible through the monumental efforts of its administrative staff. I would like to thank Christine Aguilar, Maria Frank, Chris Hall, Ziba Mahdavi, Martha Siegel, and John Skinner for always taking the time to watch out for the graduate students.

None of the work in this dissertation would have been possible without the tireless efforts of the hundreds of people associated with the Fermi-LAT Collaboration. Where original work is presented, I have tried to identify some of my closest collaborators; however, credit is always due to Fermi-LAT Collaboration as a whole. The LAT is an ambitious project, and its flawless performance is a testament to the brilliance of the collaboration that built it. The Fermi-LAT Collaboration acknowledges support from a number of agencies and institutes for both development and the operation of the

LAT as well as scientific data analysis. These include NASA and DOE in the United States, CEA/Irfu and IN2P3/CNRS in France, ASI and INFN in Italy, MEXT, KEK, and JAXA in Japan, and the K. A. Wallenberg Foundation, the Swedish Research Council and the National Space Board in Sweden. Additional support from INAF in Italy and CNES in France for science analysis during the operations phase is also gratefully acknowledged.

I would like to give a special thanks to the members of the `Pass-8` working group within the Fermi-LAT Collaboration. Working on `Pass 8` was particularly rewarding and enjoyable due in large part to the support and encouragement of Bill Atwood, Luca Baldini, Johan Bregeon, Philippe Bruel, Luca Latronico, Melissa Pesce-Rollins, Steve Ritz, Carmelo Sgrò, and Tracy Usher. A special thank you to the group at INFN Sezione di Pisa for being such brilliant hosts and mentors. I would also like to thank the LAT ISOC, INFN Sezione di Pisa, and INFN Sezione di Torino for supporting very productive trips to Italy to work on `Pass 8`.

Additional support for the work in this dissertation was provided by the Department of Energy Office of Science Graduate Fellowship Program (DOE SCGF), made possible in part by the American Recovery and Reinvestment Act of 2009, administered by ORISE-ORAU under contract no. DE-AC05-06OR23100. Being part of the DOE SCGF program was an amazing experience, and it would not have been possible without the tireless efforts of Ping Ge, Cayla Stephenson, and the SCGF team.

Over the years, I have been extraordinarily lucky to be surrounded by an amazing group of roommates, teammates, and friends. David Abram, Henry Adams, Micah Babbit, Tony Chen, Ariel Jackson, Natalie Johnson, Becky Leichtling, Debbie Lin, Vinesh Narayan, Matt McDowell, Toby Sachs-Quintana, Krishna Rao, and Dale Waters, it has always been a pleasure and a privilege to come home to you. To all my teammates, thank you for giving me the opportunity to be a part of something special. To all my dear friends, my feelings for you are unbounded.

Most of all, I will be forever grateful to my family for their unending love, support, and encouragement. I am extremely grateful to my extended family for embracing and supporting me when I recklessly moved across the country. Thank you to my brother for being living proof that many things are more fun and important than graduate school. Thank you to my father for his constant interest and his tireless efforts to make me a better writer (including his help with this dissertation). Finally, thank you to my mother for exposing me to the culture and beauty of the world. I love you all.

Contents

List of Tables

List of Figures

Chapter 1

Introduction

Over the past century, it has become evident that most of the mass of the universe is invisible. The signature of this "dark matter" is imprinted on the large-scale structure of all visible objects [1–3] and on the black-body radiation that permeates the universe [4–6]. In galaxy clusters, the largest gravitationally bound structures, dark matter is found to far out-weigh visible matter [7–9]. The rotational velocities of galaxies strongly suggest that they too possess far more mass than can be accounted for by visible components [10]. Together, the evidence suggests that dark matter makes up $\sim 27\%$ of the energy density and $\sim 85\%$ of the matter density of the universe (more than five times that of normal baryonic matter) [6]. Recently, even more striking evidence for dark matter has been discovered in low-mass objects. Specifically, the velocities of stars in the dwarf spheroidal galaxies surrounding our Milky Way Galaxy suggest that in these objects dark matter out-weighs normal matter by more than a factor of a hundred [11]. Additionally, high-resolution simulations suggest that the clumping of dark matter continues down to considerably smaller mass scales [12, 13]. The distribution of dark matter on small mass scales may hold the key to better understanding the invisible component that dominates the matter density of our universe.

While the existence of missing mass is robustly supported by observation, its microscopic nature and composition are topics of much debate. It was initially believed that dark matter was merely a manifestation of incomplete and inaccurate surveys of normal baryonic matter. Indeed, there were many issues with early measurements;[1] however, improved observational techniques now constrain both the dark component of normal matter [14, 15] and the total number of baryons [6] to a small fraction of the total missing mass. Another early proposal suggested that dark matter could be explained by alterations to the fundamental laws of gravity on large scales [16]. However, such theories of modified gravity are strongly disfavored by observations of colliding clusters of galaxies, where the baryonic matter density and gravitational potential are clearly separated [17, 18]. Thus, any dark matter candidate is constrained to be gravitating, dark (small electromagnetic coupling), non-baryonic, and largely non-interactive. Currently, the most popular theoretical framework for dark matter implies the existence of at least one new, fundamental particle.

Over the past forty years, many dark matter particle candidates have been suggested (e.g., axions [19], sterile neutrinos [20], gravatinos [21], etc.). Here, we focus on one of the most popular candidates for particle dark matter, the weakly interacting massive particle (WIMP). The WIMP paradigm arises from a set of coincidences in cosmology and high energy physics. First, the observed density of dark matter is naturally satisfied by a non-relativistic (i.e., mass in the GeV to TeV range) thermal relic particle with a weak-scale interaction cross section [22, 23]. Second, the low mass scale of the Higgs boson [24, 25] suggests the need for new physics just above the electro-weak scale (i.e., mass in the GeV to TeV range) to stabilize the Higgs mass (known as the hierarchy problem [21]). These two independent theoretical arguments together form compelling evidence for new physics at the weak scale and have motivated a vast amount of theoretical and experimental work to probe physics beyond the Standard Model.

One of the most attractive features of the WIMP scenario is that it provides a host of experimentally testable predictions. WIMPs are expected to have weak-scale scattering cross sections with Standard Model particles. Should this be the case, the nuclear recoil energy from WIMP-nucleon interactions can be directly detected in low-background experiments [26–28]. It should also be possible to produce WIMPs

---

[1] The baryonic component of galaxy clusters is dominated by ionized gas, invisible to optical observations [8, 9]

in accelerators through the collision of Standard Model particles. Such events would have distinctive signatures (e.g., missing transverse energy) that could be detected in collider experiments [29–31]. Moreover, as a thermal relic, WIMPs should possess a weak-scale self-annihilation cross section [23, 32–35]. The *in situ* annihilation (or decay) of WIMPs could be indirectly detected via the Standard Model particles produced (e.g., photons, neutrinos, positrons, etc.). Each search technique probes different (and often orthogonal) characteristics of the WIMP and carries its own benefits, difficulties, and uncertainties. It seems almost certain that the eventual detection, identification, and characterization of dark matter will require input from all three experimental approaches.

Of the three experimental techniques discussed above, only indirect detection can conclusively link new particle physics to the observed distribution of dark matter. While WIMP annihilation generically produces many standard model particles, high-energy photons are of special interest.[2] Photons with energy in the MeV to TeV range (γ rays) are unobstructed by intervening material or magnetic fields as they propagate through the universe. Thus, the spatial and spectral distribution of γ rays carry information about the intrinsic nature of the source that produced them. This provides a mechanism for distinguishing, on a statistical basis, γ rays produced by dark matter annihilation (or decay) from those produced through conventional astrophysical processes. Unfortunately, in many cases astrophysical background emission exceeds the expected signal from dark matter by many orders of magnitude. Thus, it becomes exceedingly important to find regions with high dark matter content and low astrophysical background.

Our Milky Way galaxy sits at the center of a large, smooth, centrally concentrated dark matter halo [36]. Unfortunately, the dark matter signal from this smooth halo peaks at the Galactic center, a region of intense astrophysical activity. However, small, dense, dark matter substructures with little or no baryonic content are distributed throughout the smooth Galactic halo. The largest of these substructures

---

[2] While many of the arguments made for photons apply equally well to neutrinos, the current generation of neutrino instruments are orders of magnitude less sensitive to dark matter annihilation than their photon counterparts.

are traced by sparse stellar populations and are observed as roughly two dozen dark-matter-dominated dwarf spheroidal satellite galaxies [37]. Dark matter substructures with less mass than dwarf spheroidal galaxies may contain no appreciable baryonic component [38]. The relative proximity, high dark matter density, and lack of astrophysical backgrounds make Galactic dark matter substructures some of the most promising targets when searching for dark matter annihilation via γ rays.

Over the past five years, the Large Area Telescope (LAT) on board the *Fermi Gamma-ray Space Telescope* has revolutionized our view of the γ-ray sky [39]. The LAT is a pair conversion telescope possessing unprecedented sensitivity to electromagnetic showers in the energy range from 20 MeV to 1 TeV. Utilizing technology developed in accelerator-based particle detectors, the LAT probes the notoriously difficult GeV energy regime with a level of detail inaccessible to other experiments both on the ground [40–42] and in space [43–46]. The all-sky coverage and unparalleled sensitivity of the LAT make it an ideal instrument for discovering new, faint γ-ray sources and understanding astrophysical γ-ray production. Together, the exceptional sensitivity and increased understanding of astrophysical backgrounds make the LAT a remarkable instrument for studying dark matter annihilation. As will be shown in this dissertation, the LAT makes it possible to robustly probe dark matter annihilation at the level of the thermal relic cross section through observations of Galactic dark matter substructure.

This dissertation begins by investigating the case for indirect dark matter searches via γ-ray emission from Galactic dark matter substructure. We introduce the LAT with special emphasis on the hardware and analysis techniques that yield unprecedented sensitivity to γ-ray emission in the MeV to TeV band. We then utilize the LAT to search for γ-ray emission from dark matter annihilation in dwarf spheroidal satellite galaxies of the Milky Way. We extend this discussion to the study of various theoretically motivated models of dark matter. We also discuss searches for γ rays from dark matter annihilation in Galactic dark matter substructures possessing masses less than those of the dwarf galaxies. Finally, we examine how improvements in the LAT performance and upcoming wide-field optical surveys will increase the sensitivity of future dark matter searches.

Chapter 2

Indirect Detection of Dark Matter Substructure

The purpose of this section is to motivate searches for γ-ray signals from dark matter annihilation in Galactic dark matter substructure. We begin by examining the local distribution of dark matter and the evidence, both observational and theoretical, for the presence of Galactic dark matter substructure. Next we consider the factors that contribute to the predicted strength and detectability of dark matter annihilation signals. Finally, we focus on specific targets in our search for dark matter annihilation.

2.1 Galactic Dark Matter Environment

Our current understanding of the dark matter distribution surrounding the Milky Way Galaxy is constructed from a combination of observation and simulation. Observations of resolved stellar populations orbiting the Milky Way suggest that the Galaxy sits near the center of a dark matter halo with a virial radius of $\sim 300\,\mathrm{kpc}$ and a total mass of ~ 1–$2 \times 10^{12}\,M_\odot$ [36, 47]. Additionally, from the measured velocities of stars in the Galactic disk it can be estimated the the local dark matter density is ~ 0.3–$0.4\,\mathrm{GeV\,cm^{-3}}(\sim 10^{-2}\,M_\odot\,\mathrm{pc^{-3}})$ [48–50]. However, observational constraints on the dark matter content of the inner galaxy are quite weak [51]. Thus, we must rely on simulations to construct a full mass model of the Milky Way.

Numerical simulations in a standard cold dark matter cosmology (ΛCDM) have shown that the density profiles of dark matter halos can be simply parameterized. Navarro, Frenk, and White [52] first proposed a two-parameter density profile for the distribution of dark matter in halos spanning a range of masses from large galaxy clusters to small dwarf galaxies. As the accuracy of simulations has increased, a class of double-power-law profiles has developed. Some of the most popular models for the dark matter distribution are the NFW [52], Burkert [53], and Einasto [54] profiles,

$$\rho(r) = \frac{\rho_0 r_{\rm s}^3}{r(r_{\rm s}+r)^2} \qquad \text{NFW} \tag{2.1}$$

$$\rho(r) = \frac{\rho_0 r_{\rm s}^3}{(r_{\rm s}+r)(r_{\rm s}^2+r^2)} \qquad \text{Burkert} \tag{2.2}$$

$$\rho(r) = \rho_0 \exp\left\{-2n\left(\left(\frac{r}{r_{\rm s}}\right)^{\frac{1}{n}} - 1\right)\right\} \qquad \text{Einasto} \tag{2.3}$$

These density profiles are parameterized by a normalization factor, ρ_0, and a scale radius, $r_{\rm s}$. In the case of the Einasto profile, an additional parameter, n, is used to describe the inner slope of the density profile.[1] It often proves useful to re-parameterize these profiles in terms of the quantities directly measured by simulations, specifically the maximum circular velocity, $V_{\rm max}$, and radius of maximum circular velocity, $R_{V_{\rm max}}$, of a dark matter halo [52]. For example, Kuhlen *et al.* [56] find that the parameters of the NFW profile can be described by,

$$r_{\rm s} = \frac{R_{V_{\rm max}}}{2.163} \tag{2.4}$$

$$\rho_0 = \frac{4.625}{4\pi G}\left(\frac{V_{\rm max}}{r_{\rm s}}\right)^2, \tag{2.5}$$

where $r_{\rm s}$ is in kpc and ρ_0 is in $M_\odot\,{\rm kpc}^{-3}$. Similar relationships can be derived for any of the dark matter profiles discussed above [56].

At intermediate and large radii, the dark matter profiles in Equations (2.1–2.3) are fairly consistent with one another and with observations. However, at small radii these

---

[1] While the Einasto profile may seem out of family, An and Zhao [55] show that the Einasto profile is a limiting case of cored double-power-law models.

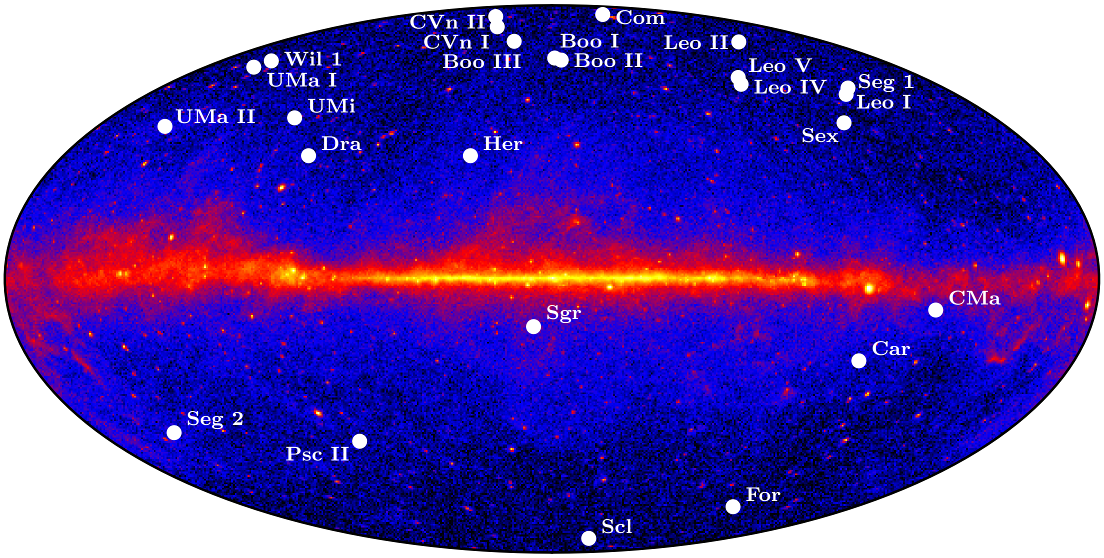

Figure 2.1 Known dwarf spheroidal satellite galaxies of the Milky Way overlaid on a 4-year, HAMMER-AITOFF projected, integrated γ-ray counts map ($E > 1$ GeV). The bright diffuse γ-ray emission associated with the Galactic plane runs horizontally across the center of the image.

profiles diverge rapidly, reflecting a lack of observational constraints. An additional concern is the relevance of dark-matter-only simulations at small radii where baryonic physics can often dominate. Therefore, even with the current generation of high resolution simulations, the distribution of dark matter near the center of the Milky Way remains highly uncertain. Thus, we are motivated to search for other targets where uncertainties in the central shape of the dark matter density profile can be mitigated.

The Milky Way galaxy possesses more than two dozen gravitationally bound satellite galaxies (Figure 2.1). The majority of these satellites are dwarf spheroidal galaxies: collections of pressure supported stars lacking appreciable gas, dust, or star formation. The "classical" dwarf spheroidal satellite galaxies have luminosities ranging from $10^5\,L_\odot$ to $10^7\,L_\odot$, while the more recently discovered "ultra-faint" dwarf spheroidal galaxies can have luminosities as low as $10^3\,L_\odot$ [11]. The population of bound satellite galaxies is expected to distributed spherically symmetrically and to extend to the Milky Way virial radius ($\sim 300\,\mathrm{kpc}$). However, the census of satellite galaxies is far from complete, and the known distribution of dwarf spheroidals is tightly correlated with the coverage of wide-field optical surveys. Since dwarf spheroidal galaxies contain relatively little astrophysical activity they are excellent probes of dark matter on small scales.

The dark matter content of dwarf spheroidal galaxies is determined spectroscopically from the velocities of their member stars. The Milky Way dwarf spheroidal galaxies have been found to contain 10^2 to 10^3 times as much dark matter as baryonic matter, making them some of the most dark matter dominated objects known [57]. Additionally, constraints on the mass within the stellar half-light radius of these objects are robust against changes in the assumed dark matter density profile. The low baryon content of dwarf galaxies suggests that their dark matter profiles will suffer less from baryonic disruption and will agree better with dark-matter-only simulations than those of larger galaxies. Additionally, it may be possible to use multiple stellar populations in some of the larger dwarf spheroidal galaxies to better constrain the inner slope of the dark matter profile [58]. These considerations make the dwarf spheroidal satellite galaxies of the Milky Way some of the best characterized dark matter distributions in the universe.

Simulations suggest that dwarf spheroidal galaxies populate the high-mass tail of an extensive population of Galactic dark matter substructure. Numerical simulations of Milky-Way-sized dark matter halos find $\sim 10^5$ subhalos above a mass resolution of $\sim 10^6\,M_\odot$ (Figure 2.2) [12, 13]. These simulations predict that the distribution of subhalos is fairly isotropic and that the number density of subhalos rises steeply with decreasing mass. While there are still significant difficulties mapping the known dwarf spheroidal galaxies onto the most massive subhalos from simulations (issues known as the "missing satellites" and "too big to fail" problems) [59–62], simulations strongly suggest that additional satellite galaxies remain to be discovered. Additionally, an abundance of lower-mass dark matter subhalos should exist without any astrophysical tracers.

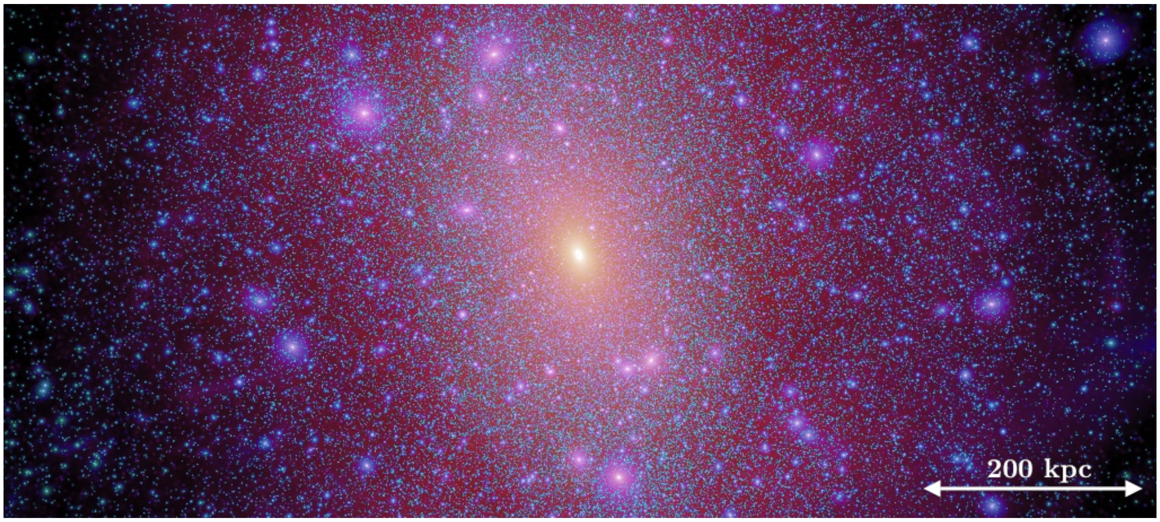

Figure 2.2 A high resolution numerical simulation of a Milky-Way-sized dark matter halo from the Aquarius Project [13]. Thousands of dark matter subhalos can be seen superimposed on the smooth primary halo. The brightness of each pixel is proportional to the logarithm of the squared dark matter density projected along the line of sight. Adapted from Springel *et al.* [13].

2.2 Indirect Detection Formalism

Having discussed the distribution of dark matter in the Galactic environment, we now consider the predicted γ-ray signal from dark matter annihilation. The γ-ray flux from dark matter annihilation depends both on the spatial distribution of dark matter and on the particle physics governing annihilation. The signal flux, $\phi_\gamma(\Delta\Omega)$ ($\mathrm{ph\,cm^{-2}\,s^{-1}\,sr}$), expected from annihilation in a dark matter density distribution, $\rho(\boldsymbol{r})$, can be expressed as

$$\phi_\gamma(\Delta\Omega) = \underbrace{\int_{\Delta\Omega} \Big\{ \int_{\mathrm{l.o.s.}} \rho^2(\boldsymbol{r}) dl \Big\} d\Omega'}_{\text{J-factor}} \cdot \underbrace{\frac{1}{4\pi} \frac{\langle\sigma v\rangle}{2m_{\mathrm{DM}}^2} \int_{E_{\min}}^{E_{\max}} \frac{dN_\gamma}{dE_\gamma} dE_\gamma}_{\Phi_{\mathrm{PP}}} . \tag{2.6}$$

The preceding J-factor represents the line-of-sight integral through the square of the dark matter density integrated over a solid angle $\Delta\Omega$. The second factor, Φ_{PP}, is strictly dependent on the properties of the dark matter particle: the thermally-averaged annihilation cross section, $\langle\sigma v\rangle$, the particle mass, m_{DM}, and the differential photon yield into γ rays, dN_γ/dE_γ, summed over all final states and integrated over the experimental energy range. Qualitatively, the J-factor characterizes the astrophysical distribution of dark matter, while $\Phi_{\rm PP}$ sets the spectral character of the annihilation signal. Both the J-factor and $\Phi_{\rm PP}$ contribute to the normalization of the annihilation flux representing a degeneracy between the amount of dark matter and the annihilation rate. This degeneracy can be broken if the dark matter signal can be spatially resolved.

2.2.1 Astrophysics Factor

The astrophysical J-factor is calculated directly from the distribution of dark matter and follows directly from the discussion in Section 2.1. J-factor calculations are subject to the same sources of uncertainty as calculations of the underlying dark matter distribution. Specifically, in the central regions of dark matter halos, where $r \ll r_{\rm s}$, J-factors tend to be systematics dominated due to uncertainties in the halo profile at these distance scales. This systematic uncertainty is minimized when the J-factor integration angle corresponds to the projected radius at which the integrated mass of the object is best determined [63, 64]. Unfortunately, when performing experimental searches for dark matter annihilation it is not always possible to choose the integration angle *a priori* due to instrumental or astrophysical constraints. For dark matter substructures, the integrated J-factor within 0.5° can reach $\sim 3 \times 10^{19}\,{\rm GeV^2\,cm^{-5}}$ with an uncertainty $\lesssim 0.5$ decades (see Chapter 5).

2.2.2 Particle-Physics Factor

The particle physics factor, $\Phi_{\rm PP}$, describes the dark matter annihilation rate and the spectrum of standard model particles produced. The annihilation rate is set by the factor $\langle\sigma v\rangle/m_{\rm DM}^2$ where $\langle\sigma v\rangle$ is the thermally averaged annihilation cross section and $m_{\rm DM}$ is the mass of the dark matter particle. The cross section represents the probability for two dark matter particles to annihilate, while the factor of $1/m_{\rm DM}^2$ reflects the decreasing number density of dark matter particles with increasing particle mass. The annihilation spectrum is set by the differential photon yield, dN_γ/dE_γ, based on the Standard Model channels through which the annihilation occurs (e.g., $b\bar{b}$, $\tau^+\tau^-$, etc..). The Standard Model branching fraction can be theoretically motivated, chosen *a priori*, or fit to γ-ray data. Differential photon yields are calculated for each annihilation channel either from numerical packages, such as `Pythia` [65], or from analytic fitting formulae [66, 67].

At this point it is important to consider theoretical predictions for the components of the particle physics factor. Under the assumption that dark matter was produced and evolved thermally in the early universe, the thermally averaged annihilation cross section, $\langle \sigma v \rangle$, will dictate the evolution of the dark matter relic density between thermal decoupling and freeze-out [68]. This allows us to relate the annihilation cross section to the current dark matter relic density, $\Omega_{\rm DM} h^2 \approx (3 \times 10^{-27}\,{\rm cm}^3\,{\rm s}^{-1})/\langle \sigma v \rangle$. Current measurements of $\Omega_{\rm DM} h^2 \approx 0.1$ yield a characteristic thermal relic annihilation cross section of $\langle \sigma v \rangle \sim 3 \times 10^{-26}\,{\rm cm}^3\,{\rm s}^{-1}$ [6].[2] This argument is relatively insensitive to the mass of the dark matter particle because the abundance of dark matter after freeze-out is inversely proportional to the dark matter particle mass. Remarkably, this cosmologically motivated cross section is very similar to that derived for a weakly interacting particle, $\langle \sigma v \rangle \sim \alpha^2 / E^2_{\rm weak} \approx 5 \times 10^{-26}\,{\rm cm}^3\,{\rm s}^{-1}$, where α is the coupling constant [21]. This cosmic coincidence, known as the "WIMP Miracle", is one of the foundations for linking the dark matter problem in astrophysics to the hierarchy problem high energy physics [68].

Bounds on the mass of the dark matter particle, $m_{\rm DM}$, can be set through both cosmological and particle physics arguments. The ΛCDM model of cosmology requires that dark matter be non-relativistic at freeze-out and current observations of large-scale structure, the Lyman-α forest, and the presence of dwarf spheroidal galaxies set a lower bound on the dark matter mass at $m_{\rm DM} \gtrsim 1\,{\rm keV}$ [70–72]. Additionally, unitarity arguments can be used to set an upper bound on the dark matter particle mass at $m_{\rm DM} \lesssim 340\,{\rm TeV}$ (assuming the relic abundance is fully saturated by a single particle) [73]. If dark matter is assumed to be weakly interacting, the lower bound on the mass can be increased to $m_{\rm DM} \gtrsim 2\,{\rm GeV}$ [74]. Finally, arguments about new

---

[2] A more rigorous calculation of the thermal relic cross section is performed by Steigman *et al.* [69].

physics beyond the standard model favor particles with mass similar to the weak scale, $m_{\rm DM} \sim 100\,{\rm GeV}$. While the “naturalness” of a dark matter particle with $m_{\rm DM} \sim 100\,{\rm GeV}$ and $\langle\sigma v\rangle \sim 3\times10^{-26}\,{\rm cm^3\,s^{-1}}$ is highly quoted, it should be remembered that these canonical values are only benchmarks. There are many theories, such as axions, sterile neutrinos, gravitinos, or even less simplified supersymmetry that can produce dark matter candidates with particle characteristics that differ from the canonical values by orders of magnitude.

2.3 Targets for Indirect Detection

With a better understanding of the Galactic dark matter distribution and predictions for the γ-ray signal from annihilation, we now focus on specific targets for the indirect detection of dark matter annihilation in Galactic substructure. We separately discuss dwarf galaxies, where stars trace the dark matter potential, and unassociated dark matter substructures, where stellar associations may not exist. Finally, we summarize some of the basic instrumental requirements for probing dark matter annihilation in Galactic dark matter substructures.

2.3.1 Dwarf Spheroidal Galaxies

The dwarf spheroidal satellite galaxies of the Milky Way are some of the most dark-matter dominated objects. Large dark matter content, minimal Galactic foreground emission, and lack of astrophysical γ-ray production mechanisms [75, 76] make dwarf spheroidal galaxies promising targets for the indirect detection of dark matter. Since the same dark matter particle is expected to reside in all dwarf spheroidal galaxies, the γ-ray annihilation spectrum should be shared between these objects. Additionally, since the dark matter content of each dwarf spheroidal galaxy can be determined from stellar kinematic data, it is possible to predict the relative strength and spatial distribution of the annihilation signal expected from each galaxy. These characteristics provide a mechanism for distinguishing a dark matter annihilation signal in dwarf galaxies from conventional astrophysical backgrounds. Finally, the assumption of shared dark matter particle characteristics allows observations of multiple dwarf galaxies to be combined to increase sensitivity to a dark matter annihilation signal.

2.3.2 Unassociated Galactic Substructure

The abundant Galactic dark matter substructure predicted by simulations presents an attractive class of dark matter targets. Massive dark matter subhalos located in the outer regions of the Galactic halo or lower mass subhalos located near to Earth may constitute a significant population of γ-ray sources. These subhalos are expected to have hard γ-ray spectra and to lack counterparts at other wavelengths. Additionally, some nearby substructures may constitute spatially extended sources resolvable by the current generation of γ-ray experiments. Again, since the dark matter particle characteristics should be shared within all subhalos, these subhalos would manifest themselves as a population of unassociated γ-ray sources with similar spectral characteristics.

It should be emphasized that we expect the known dwarf spheroidal galaxies to populate the massive tail of a continuum of dark matter substructure. Since it is clear that current surveys are not complete down to the luminosity of the ultra-faint dwarfs, we expect to find many additional dwarf galaxies [77]. It is also possible that an object first identified as a dark matter subhalo candidate in γ rays may later be found to be coincident with newly discovered ultra-faint dwarf galaxies. The discovery of a population of such sources possessing similar γ-ray spectra and dwarf spheroidal galaxy counterparts would be very suggest a dark matter origin for the γ-ray emission.

2.3.3 Instrumental Requirements

The scientific requirements for a γ-ray instrument able to probe Galactic dark matter substructure are non-trivial and have only recently been met. Firstly, the instrument must be sensitive to γ-rays in the MeV to TeV energy range in order to probe dark matter masses in the GeV to TeV range. The instrument must have good energy resolution in order to distinguish an annihilation spectrum from astrophysical backgrounds and to characterize the dark matter particle (if detected). With sub-degree-scale angular resolution the instrument would be sensitivity to the spatial distribution of dark matter in the nearest substructures. Additionally, a large field-of-view would allow the instrument to observe many targets at once, making it easier to search for shared spectral features. Finally, good timing resolution and a high observing cadence would allow the instrument to identify temporally variable sources such as pulsars (high frequency) or active galactic nuclei (low frequency) and to exclude them as an astrophysical background. The technology required to meet these scientific goals has recently been assembled into the newest generation of space-based γ-ray telescopes.

Chapter 3

The Large Area Telescope

The Large Area Telescope (LAT) on board the *Fermi Gamma-ray Space Telescope* (*Fermi*) has revolutionized the study of the γ-ray sky. The LAT surveys the entire sky every ~ 192 minutes from a low-Earth orbit of $565\,\mathrm{km}$ [39]. Utilizing technology borne out of high-energy particle physics experiments, the LAT out performs its predecessors by orders of magnitude in energy range ($20\,\mathrm{MeV}$ to $1\,\mathrm{TeV}$), field-of-view ($\sim 2.4\,\mathrm{sr}$), and angular resolution ($\sim 0.2^\circ$ above $10\,\mathrm{GeV}$) [43–46]. These features have allowed the LAT to open a new regime in the discovery and study of faint γ-ray sources.

3.1 The LAT Instrument

The LAT is composed of three primary instrumental subsystems: an anticoincidence detector, a precision tracker/converter, and an imaging calorimeter (Figure 3.1). The tracker and calorimeter function together to determine the energy and direction of incident particles while the primary function of the anticoincidence detector is to identify charged particles. The LAT is organized in a 4×4 array of 16 tracker/calorimeter modules. The anticoincidence detector surrounds the tracker and calorimeter, and is itself surrounded by a micrometeorite shield and thermal blanket. The LAT instrument possess nearly 10^6 electronic channels operated on a power budget of $\sim 650\,\mathrm{W}$ (less than that of a toaster) [39]. The LAT has performed nearly flawlessly since

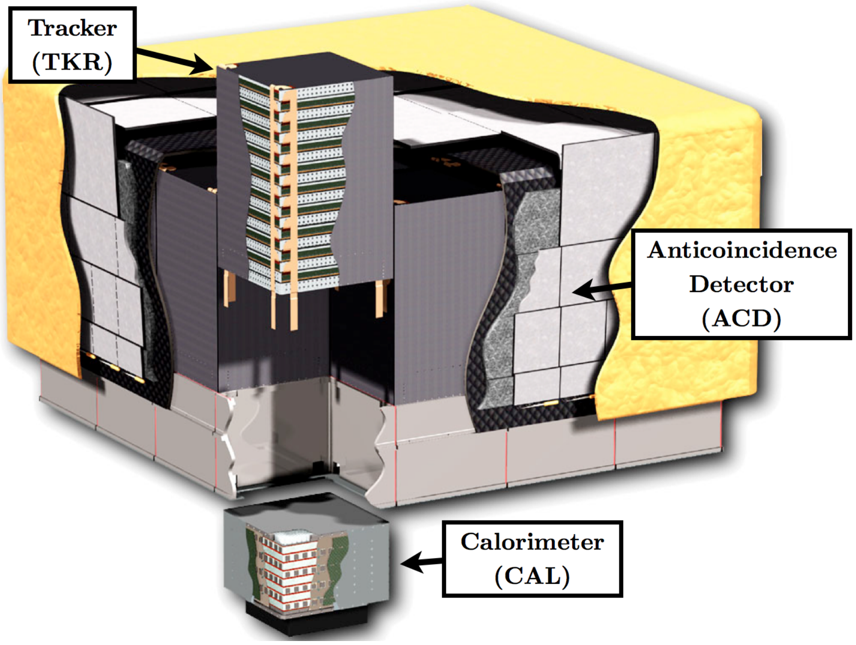

Figure 3.1 A schematic diagram of the Large Area Telescope (LAT). The dimensions of the telescope are 1.8 m × 1.8 m × 0.72 m. A cutaway of a single LAT module shows the tracker and calorimeter components. The anticoincidence detector surrounds the LAT tracker and the upper third of the CAL. Adapted from Atwood *et al.* [39].

launch in 2008, triggering $> 3 \times 10^{11}$ times and collecting $> 3 \times 10^{8}$ high-quality γ rays.

3.1.1 Anticoincidence Detector (ACD)

As the outermost subsystem of the the LAT instrument, the anticoincidence detector (ACD) is faced with the task of identifying singly charged particles with an efficiency of 0.9997 [78]. At the same time, the ACD must avoid “self-vetoes” caused by X-ray and charged-particle backsplash from the interaction of energetic particles with LAT calorimeter. To meet these scientific requirements, the ACD design is segmented into 89 tiles of high-efficiency plastic scintillator. Scintillation light from each tile is collected by wavelength shifting fibers and recorded redundantly by two high-quantum-efficiency photomultiplier tubes. To minimize particle leakage, ACD tiles overlap in one dimension, and gaps in the other dimension are filled by scintillating fiber ribbons. Output signals from the ACD photomultipliers are used to generate two types of signals: (1) fast veto pulses used by on-board LAT trigger electronics, and (2) slower pulse-shaped signals for detailed charged particle rejection on the ground.[1] While the ACD is the outermost active system, it is surrounded by a micrometeorite shield and thermal blanket for protection from the space environment.

3.1.2 The Tracker (TKR)

The primary goal of the LAT tracker/converter (TKR) is to convert incident γ rays into electron-positron pairs and precisely track the resulting daughter particles [79]. The TKR is composed of 18 detector planes, each containing two orthogonal x-y layers of silicon strip detectors for tracking the passage of charged particles. The TKR must strike a delicate balance between the need for thin converters to preserve angular resolution at low energy, and the need for thick converters to maximize γ-ray conversion efficiency at high energy. The design compromise was to segment the TKR into a “FRONT” section, consisting of the top 12 planes that possess thin (0.03 radiation length) tungsten foil converters and a “BACK” section consisting of 4 planes that possess thicker (0.18 radiation length) tungsten converters. In an attempt to preserve triggering efficiency for γ rays converting in the final thick converter, the 2 bottom TKR planes contain no converter. The total on-axis depth of the TKR is 1.5 radiation lengths, which yields a γ-ray conversion probability of $\sim 63\%$ [79]. The thick converters have the additional benefit of partially shielding the FRONT section of the TKR against low-energy calorimeter backsplash. The large acceptance of the LAT does not allow for a time-of-flight system; however, the tracker electronics do provide “time-over-threshold” information for each channel, which can be used to distinguish out-of-time events.

---

[1] The interplay of these two electronic output signals for out-of-time particle rejection is discussed in more detail in Appendix C.

3.1.3 The Calorimeter (CAL)

The primary purpose of the LAT calorimeter (CAL) is to measure the energy deposited by an electromagnetic shower [39]. Each tower contains a CAL module of 96 CsI crystals arranged in a hodoscopic array of 8 layers of 12 crystals. The light yield of each crystal is recorded on each end by both large and small photodiodes. This readout structure provides a large dynamic energy range for each crystal (2 MeV to 70 GeV) and an accurate estimation of the longitudinal shower position (from the differential light yield). Space and weight constraints restricted the depth of the CAL to 8.6 radiation lengths on-axis, and shower maximum occurs outside the active volume of the CAL for a significant fraction of photons with energy $\gtrsim$100 GeV. However, the imaging capability of the CsI crystals allows for an accurate determination of electromagnetic shower shape and energy into the TeV regime [80].

3.2 Reconstruction and Background Rejection

The purpose of the LAT event reconstruction software is to assemble the raw electronic readout into a physical picture of a particle interaction with the LAT instrument (Figure 3.2). Some quantities, such as clusters of hits in the TKR, the sum of the crystal energies in the CAL, or the hits in the ACD can be determined by a single subsystem. However, full characterization of an event relies heavily on correlating and associating information across multiple subsystems. For example, the centroid of the raw CAL energy is often used to seed Kalman track finding in the TKR. Subsequently, the TKR direction is used to correct the raw CAL energy for leakage through the gaps, sides, and back of the CAL. Low-energy γ rays can deposit a significant fraction of their energy in the TKR, which must be incorporated into estimates of the total event energy. Additionally, hits in the ACD are associated with the TKR direction to determine whether they were caused by the incident particle or by backsplash. Thus, event reconstruction combines the LAT subsystems into a set of physical quantities that can be used to determine the key properties of an event: incident direction, total

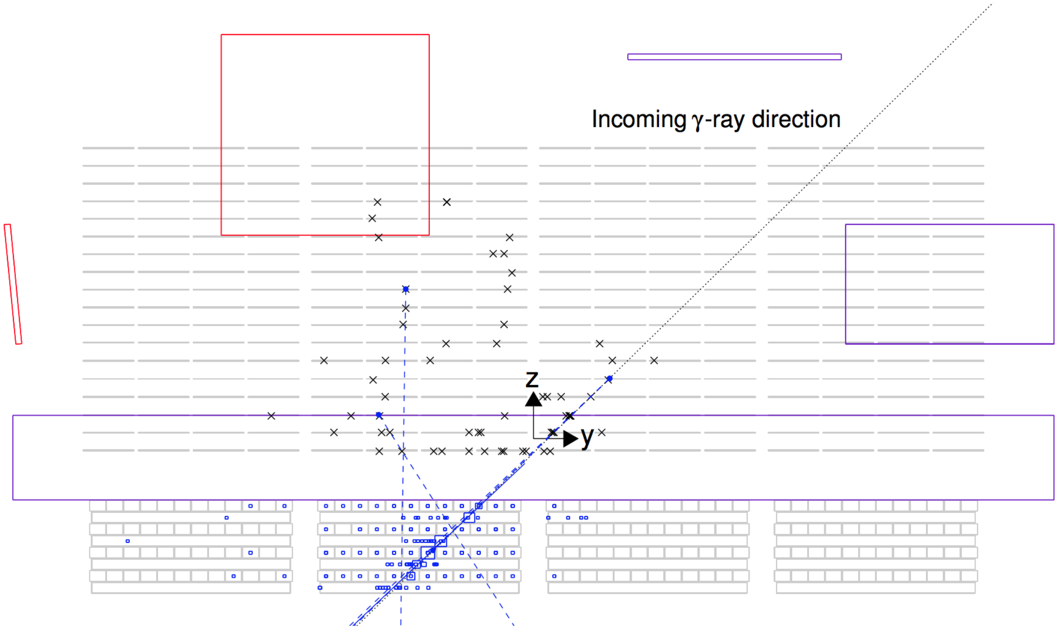

Figure 3.2 Event display of a simulated 27 GeV γ ray interacting with the LAT instrument. Clusters of hit TKR strips are represented by black crosses, while the location and magnitude of energy depositions in the CAL crystals are represented by variable-size blue squares. Hit ACD tiles are represented by colored boxes, with color corresponding to the amount of energy deposited. The dotted line represents the true γ-ray direction, the dashed lines represent reconstructed TKR tracks, and the solid line represents the CAL axis. Figure from Ackermann *et al.* [81].

energy, and particle type.[2]

Event classification is one of the most difficult steps in the event reconstruction process. The LAT orbital environment and science goals require a background reduction of 10^6 for protons and 10^4 for electrons and positrons, while maintaining a γ-ray efficiency of $\sim 75\%$. Background rejection is made especially difficult by the large phase space over which the LAT accepts events (i.e., energy, direction, and event topology). The LAT event classification utilizes a combination of classical cut-based analyses and multivariate classification algorithms, specifically classification trees [82]. Some of the most important topological characteristics for identifying particle type

---

[2] The ongoing effort to utilize flight data to improve the LAT event reconstruction is discussed in Appendix A.

are the associations between TKR tracks and active ACD elements, the disagreement between the reconstructed direction in the TKR and CAL, the presence of extra hits surrounding the tracks in the TKR, and the longitudinal shower profile in the CAL. Classification trees are trained to use these (and other) event characteristics to distinguish γ rays from charged particles via supervised learning on simulated data sets. The wide range of LAT science makes it necessary to generate multiple event selections, each possessing a signal to background ratio suitable for specific science topics.[3]

3.3 LAT Instrument Performance

The performance of the LAT for a given event selection can be represented by a set of instrument response functions (IRFs) that parameterize, in instrument coordinates, the observed event energy, E', and incident direction, $\hat{v}\,'$, as a function of true event energy, E, and incident direction, $\hat{v}$. In practice, the IRFs are factorized into three components:

1. The effective area, $A(E, \hat{v})$, is the product of the cross-sectional geometric collection area, γ-ray conversion probability, and the efficiency of a given event selection.

2. The point-spread function (PSF), $P(\hat{v}\,' \,|\, E, \hat{v})$, is the probability density to reconstruct an event direction for a given true energy and direction.

3. The energy dispersion, $D(E' \,|\, E, \hat{v})$, is the probability density to reconstruct an event energy, for a given true energy and direction.

Note that this formulation assumes that the PSF and energy dispersion are independent.[4] Also note that the LAT pointing history is required to convert from instrument coordinates to sky coordinates. The performance of the "`Pass 7`" iteration of the LAT IRFs can be found in Figure 3.3.

---

[3] Improvements to the LAT background rejection can be found in Appendix B

[4] For the long-duration observations discussed here, the correlation of the PSF and energy dispersion is negligible [81].

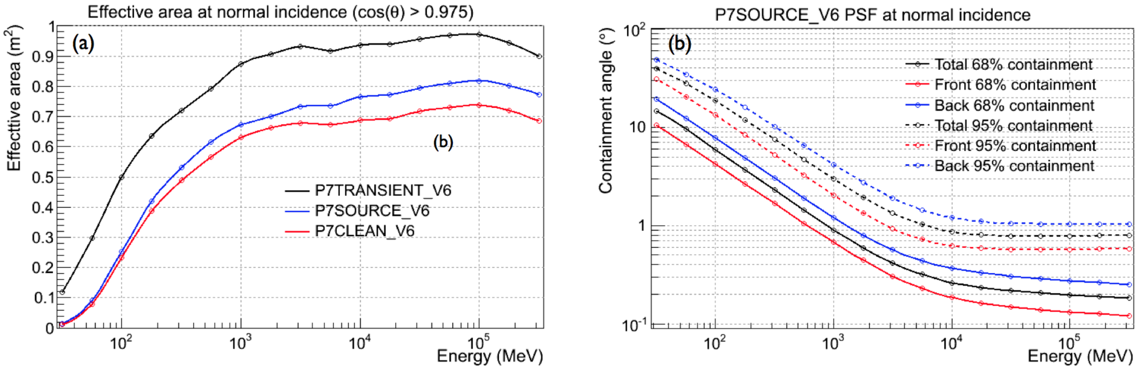

Figure 3.3 Performance at normal incidence of the `Pass 7` reconstruction and event classification scheme as a function of incident photon energy. Shown from left to right are: (a) the effective area and (b) the points spread function. Adapted from Ackermann *et al.* [81].

The LAT IRFs are derived primarily through GEANT4-based Monte Carlo simulations of γ rays interacting with the LAT detector and *Fermi* spacecraft [39]. Observed agreement between flight data and simulations has largely validated this mechanism. However, there do exist some unanticipated features in the flight data that require minor modifications to the Monte-Carlo-derived IRFs (specifically, the PSF). Systematic uncertainties in the instrument performance can bias the characterization of γ-ray sources properties at the level of $\leq 10\%$ [81]. Efforts are ongoing within the Fermi-LAT Collaboration reduce these uncertainties and to improve the performance of the LAT instrument (see Appendix A).

Chapter 4

Likelihood Analysis of LAT Data

4.1 The LAT Likelihood Function

LAT searches for faint γ-ray sources often necessitate the use of a likelihood-based analysis to account for the complicated dependence of the LAT instrument on energy and geometry, the all-sky survey strategy, and the structured diffuse γ-ray backgrounds. The likelihood function, $\mathcal{L}(\boldsymbol{\alpha}\,|\,\mathcal{D}) \equiv \mathcal{P}(\mathcal{D}\,|\,\boldsymbol{\alpha})$, is the probability of obtaining the data, $\mathcal{D}$, given an input model with parameters, $\boldsymbol{\alpha}$. The binned LAT likelihood function is defined as the a product of Poisson likelihoods,

$$\mathcal{L}(\boldsymbol{\alpha}\,|\,\mathcal{D}) = \prod_k \frac{\lambda_k^{n_k} e^{-\lambda_k}}{n_k!} \tag{4.1}$$

where in each bin, k, the observed counts are denoted by $n_k = n_k(\mathcal{D})$ and the expected counts produced by the model are denoted by $\lambda_k = \lambda_k(\boldsymbol{\alpha})$. In the limit that the bin size becomes infinitely small then $n_k \in \{0, 1\}$, and we are left with an unbinned likelihood,

$$\mathcal{L}(\boldsymbol{\alpha}\,|\,\mathcal{D}) = \prod_k \lambda_k e^{-\lambda_k} \tag{4.2}$$

where k now indexes individual photons.

While the likelihood formulation depends explicitly on the model-predicted counts, the physical quantity of interest is the differential γ-ray flux of a source. We write the γ-ray source distribution as $S(E, \hat{p} \,|\, \boldsymbol{\alpha})$, where $\hat{p}$ represents the incident direction of a γ ray in celestial coordinates and can be translated to instrument coordinates via the spacecraft orientation, $\hat{v}(t \,|\, \hat{p})$. To calculate the number of counts predicted by a model in a given pixel, k, we forward-fold the differential flux model of each γ-ray source with the IRFs (Section 3.3),

$$\lambda_k(\boldsymbol{\alpha}) = \sum \iiint S(E, \hat{p} \,|\, \boldsymbol{\alpha}) A(E, \hat{v}) P(\hat{v}' \,|\, E, \hat{v}) D(E' \,|\, E, \hat{v}) d\Omega dE dt. \tag{4.3}$$

In the previous equation, we have summed over all γ-ray sources and explicitly integrated over the observing time, the energy range, and the solid angle in the LAT frame.

A number of simplifying assumptions are often made to reduce the computational cost of this calculation. First, a region of interest (ROI) is defined around the source of interest, and the γ-ray emission model is created from only those sources within a few PSF-widths of this region. Additionally, the observing time and exposure are precomputed discarding the small dependence of the IRFs on azimuthal angle. Lastly, the effects of energy dispersion are often ignored for binned analyses where the bin size is large compared to the scale of the energy dispersion ($\sim$10% over much of the LAT energy range).

When searching for faint γ-ray sources, it is essential to have an accurate model of the diffuse γ-ray background. The diffuse background is generally factorized into two components: (1) a spatially-structured Galactic component corresponding to the γ-ray emission from the interaction of cosmic rays with interstellar gas, dust, and photon fields, and (2) an isotropic component corresponding to the combination of extragalactic γ-ray emission and instrumental charged particle background. The Galactic emission is determined by fitting physically-motivated templates to the all-sky LAT data, while the isotropic emission is fit to the residual between the LAT data and the Galactic diffuse model. When searching for new γ-ray sources, the normalizations of the two diffuse components are often left free while the spectral shapes are fixed.

4.2 The Profile Likelihood

To derive the best-fit model given the data, we maximize the likelihood with respect to the parameters of interest,

$$\hat{\boldsymbol{\alpha}} = \arg\max_{\boldsymbol{\alpha}} \mathcal{L}(\boldsymbol{\alpha} \,|\, \mathcal{D}), \tag{4.4}$$

where $\hat{\boldsymbol{\alpha}}$ represents the maximum likelihood estimator (MLE) of the parameters, $\boldsymbol{\alpha}$. In practice, maximizing a non-linear likelihood for a large set of parameters can be computationally infeasible. A conventional approach to this problem is to partition the set of parameters, $\boldsymbol{\alpha}$, into a set of parameters of interest, $\boldsymbol{\mu}$, and a set of nuisance parameters, $\boldsymbol{\theta}$, such that $\boldsymbol{\alpha} = \{\boldsymbol{\mu}, \boldsymbol{\theta}\}$. For example, the parameters of interest may include the spectral index or flux of a specific γ-ray source, while the nuisance parameters could be background γ-ray sources or constraints on source characteristics derived from independent analyses (e.g., see Section 5.3.3 or Section 5.4.4). The profile likelihood is defined as

$$\mathcal{L}_p(\boldsymbol{\mu} \,|\, \mathcal{D}) = \sup_{\boldsymbol{\theta}} \mathcal{L}(\boldsymbol{\mu}, \boldsymbol{\theta} \,|\, \mathcal{D}). \tag{4.5}$$

The calculation of the profile likelihood reduces the dimensionality of the likelihood by maximizing with respect to the nuisance parameters at each value of $\boldsymbol{\mu}$. While the profile likelihood discards information about the full distribution of the nuisance parameters, it is found to retain many of the statistical properties of the full likelihood [83].

4.3 The Joint Likelihood

Often a population of sources share a common set of physical characteristics (e.g., luminosity, spectral model, etc.). The sensitivity to a given characteristic of the population can be enhanced by combining observations of multiple sources. Within the context of a likelihood-based analysis, this leads naturally to the concept of a joint likelihood. A joint likelihood is formed from the product of the individual likelihoods for each source, i, which are derived in the manner discussed in Section 4.1. Thus, the joint likelihood is defined as

$$L(\boldsymbol{\alpha}_s, \{\boldsymbol{\alpha}_i\} \,|\, \{\mathcal{D}_i\}) = \prod_i \mathcal{L}_i(\boldsymbol{\alpha}_s, \boldsymbol{\alpha}_i \,|\, \mathcal{D}_i) \tag{4.6}$$

where the parameters can be broken into a set of parameters shared by all sources, $\boldsymbol{\alpha}_s$, and a set of parameters dependent on each individual source, $\{\boldsymbol{\alpha}_i\}$. For example, a set of shared parameters may be the intrinsic luminosity or spectral model, while the independent parameters may include the distance to each source, point-like background sources within each ROI, or the normalization of a diffuse background near each source. Once formed, the joint likelihood can be treated analogously to the likelihood of a single source, including the construction of a profile joint likelihood.

The joint likelihood formulation has significant advantages over simple counts stacking, which sums the observations and exposures of each individual source. Counts stacking severs the link between individual source characteristics and the data set associated with them. For example, simple counts stacking weights events associated with fainter sources equally to events associated with brighter sources. Additionally, with counts stacking, high-background regions can dilute the sensitivity of low-background regions. Counts stacking can be modified to mitigate these issues, but the simple and rigorous statistical framework associated with the joint likelihood formalism often makes it the more attractive approach.

4.4 Hypothesis Testing

The likelihood formalism provides a robust statistical framework for hypothesis testing. A common hypothesis is that the parameters of interest, $\boldsymbol{\mu}$, deviate from their nominal expected values, $\boldsymbol{\mu}_0$. We can utilize the likelihood ratio test to define a "test statistic", TS, from the ratio of the maximum likelihood assuming two hypotheses [84],

$$\mathrm{TS} = 2\ln\left(\frac{\mathcal{L}(\hat{\boldsymbol{\mu}} \,|\, \mathcal{D})}{\mathcal{L}(\boldsymbol{\mu}_0 \,|\, \mathcal{D})}\right) = 2\left(\ln\mathcal{L}(\hat{\boldsymbol{\mu}} \,|\, \mathcal{D}) - \ln\mathcal{L}(\boldsymbol{\mu}_0 \,|\, \mathcal{D})\right). \tag{4.7}$$

Under suitable asymptotic boundary conditions, theorems by Wilks [85] and Chernoff [86] state that the distribution of TS values under the null hypothesis (i.e., $\boldsymbol{\mu} = \boldsymbol{\mu}_0$) should follow a χ^2_n-distribution, where n represents the dimensionality of $\boldsymbol{\mu}$. Thus, the probability of incorrectly rejecting the null hypothesis can be derived analytically from,

$$p = \int_{\mathrm{TS}}^{\infty} \chi^2_n(x)dx. \tag{4.8}$$

In practice, the asymptotic conditions are not always satisfied, and it is necessary to empirically derive the p-value from simulations. Often, a significance in terms of Gaussian sigma, $N\sigma$, is quoted rather than a p-value where $N = \sqrt{2}\,\mathrm{erf}^{-1}(1-p)$.

A common application of the likelihood ratio test is to assign a discovery significance to a γ-ray source. In this case, the parameter of interest is the flux of the putative source and the null hypothesis assumes that the putative source flux is zero. Following Equation (4.7), we can define a TS by maximizing the likelihood both with the putative source flux free to vary and with the the putative source flux fixed to zero. The conventional threshold for source detection is set at TS ≥ 25, which corresponds to a Gaussian significance of 5σ for a single free parameter (the putative source flux). However, often the spectral index of the putative source is also left free in the fit, decreasing the detection signficance to $\sim 4.2\sigma$ [87].

The likelihood formalism not only yields a best-fit value for the parameters of interest but can also be used to ascribe an uncertainty to those parameters [88]. In this case, the shape of the likelihood function is used to determine the uncertainty in the best-fit parameters. In the regime where the null hypothesis is excluded at high significance, this procedure results in a two-sided interval bracketing the maximum likelihood estimate. However, in the case where the null hypothesis cannot be robustly excluded, it is common practice to set a one-sided confidence limit on the maximum deviation from the null hypothesis allowed by the data. Unfortunately, this situation often occurs in the low-counts regime where the asymptotic formulae for determining the significance of such a limit are invalid. Solutions to this problem have been suggested by many authors [89–92], and in subsequent analyses we utilize the delta-log-likelihood method of Rolke *et al.* [92] due to its treatment of nuisance parameters.

Chapter 5

Search for Gamma-ray Signals from Dwarf Spheroidal Galaxies[†]

5.1 Overview

This chapter focuses on LAT searches for γ-ray signals coincident with Milky Way dwarf spheroidal satellite galaxies. As discussed in Chapter 2, dwarf spheroidal galaxies are excellent targets in the search for dark matter due to their relative proximity, their lack of astrophysical contamination, and their large, well-characterized dark matter content. Since the launch of the LAT, γ-ray observations of dwarf spheroidal galaxies have become a topic of much study [93–100]. In this chapter, we present two recent searches for γ-ray emission coincident with dwarf spheroidal galaxies. Because the determination of J-factors is essential for interpreting γ-ray searches in the context of dark matter, we begin this chapter by discussing the dynamical modeling of dwarf spheroidal systems. In Section 5.3 we present a search for γ-ray signals coincident with the location of 10 dwarf spheroidal galaxies using 2 years of LAT data. This 2-year search robustly accounts for uncertainties in the J-factors of the dwarf galaxies and combines observations of 10 dwarf galaxies into a single joint likelihood

---

[†] This chapter represents work done with the Fermi-LAT Collaboration. Section 5.3 is published as Ackermann *et al.* [93], while Section 5.4 is being prepared for publication. Special thanks to E. Bloom, J. Cohen-Tanugi, J. Conrad, M. Llena-Garde, G. Martinez, L. Strigari, and M. Wood.

function for improved sensitivity. In Section 5.4 we expand and improve upon the previous analysis utilizing 4 years of LAT data, the full population of 25 Milky Way dwarf spheroidal galaxies with updated dynamical modeling, an increased γ-ray acceptance, and an improved LAT instrument performance. Additionally, we present a combined analysis of 15 dwarf spheroidal galaxies and a spectrally-independent analysis for each of the 25 dwarf galaxy. The analyses discussed in this chapter represent the first time that γ-ray observations have been used to robustly constrain the generic thermal relic cross section for s-wave annihilation processes ($\sim 3 \times 10^{-26}\,\mathrm{cm}^3\,\mathrm{s}^{-1}$).

5.2 Dynamical Modeling

Robust J-factor determinations are essential for interpreting γ-ray observations in the context of dark matter searches. Since a variety of techniques are used to calculate the J-factors of dwarf spheroidal galaxies, we start by describing the principles of dynamical modeling in dwarf spheroidal systems. The precise techniques used to calculate the J-factors in this chapter are discussed in more detail in Section 5.3.2 and Section 5.4.3.

In principle, the six-dimensional collisionless Boltzmann equation can be used to fully describe the gravitational potential of dwarf spheroidal systems through the phase-space distributions of their member stars. In practice, stellar data is only available in three dimensions: two spatial dimensions orthogonal to the line of sight, and one velocity dimension along the line of sight. Thus, it is often necessary to integrate the collisionless Boltzmann equation over velocity space to form the spherical Jeans equations [101],

$$\frac{1}{\nu}\frac{d}{dr}(\nu\overline{v_r^2}) + \frac{2}{r}(\overline{v_r^2} - \overline{v_\theta^2}) = -\frac{GM(r)}{r^2}. \tag{5.1}$$

Here, the mass profile, $M(r)$, is specified in terms of the stellar density profile, $\nu(r)$, and the stellar velocity dispersion, $\overline{v^2}$. Because velocity measurements are performed only along the line of sight, the anisotropy parameter, $\beta = 1 - \overline{v_\theta^2}/\overline{v_r^2}$, is often poorly constrained [57]. The poor constraints on the anisotropy parameter ultimately limit the ability of a Jeans analysis to constrain the mass profile in a manner that is completely independent of the assumed dark matter density profile. Solutions to the Jeans equations are generally found through Bayesian parameter estimation using Markov Chain Monte Carlo (MCMC) and marginalized over uncertainties in the anisotropy parameter and the parameters of the dark matter distribution [57, 102].

Recent studies have shown that the the Milky Way dwarf spheroidal galaxies possess a common mass-scale that is independent of assumptions about the form of the dark matter profile or the anisotropy parameter [11, 63, 64]. This result suggests that dwarf galaxies reside in dark matter halos of similar mass regardless of their stellar luminosity; thus, a simple analytic relationship should exist between the dwarf galaxy half-light radius, stellar velocity dispersion, and dynamical mass. Walker *et al.* [63] show that by fitting the stellar density profile of the dwarf spheroidals to a Plummer profile ($\nu(r) \propto [1 + r^2/r_{\rm h}^2]$) with projected half-light radius, $r_{\rm h}$, isotropic velocity distribution, $\beta = 0$, and constant velocity dispersion, $\overline{v_r^2}(r) = \sigma_\star^2$, the Jeans equations give

$$M(r) = -\frac{r^2 \overline{v_r^2}}{G\nu}\frac{d\nu}{dr} = \frac{5 r_{\rm h} \sigma_\star^2 (r/r_{\rm h})^3}{G[1 + r^2/r_{\rm h}^2]} \,. \tag{5.2}$$

At the half-light radius this provides a convenient estimate of the enclosed mass,

$$M_{\rm h} \equiv M(r_{\rm h}) = \frac{5 r_{\rm h} \sigma_\star^2}{2G} \,. \tag{5.3}$$

Walker *et al.* [63] find that this simple analytic estimator for $M_{\rm h}$ is in excellent agreement with computationally intensive solution to the full Jeans equations. The agreement between the Jeans analysis and the simple $M_{\rm h}$ estimator supports the claim that the mass within the half-light radius is well-constrained, independent of the assumed dark matter density profile. Additionally, as can be seen in Table 5.1, this simple estimator shows that even with the $r_{\rm h}$, some dwarfs can have a mass-to-light ratio of $\sim 100\, M_\odot/\, L_\odot$.

J-factors are determined for Milky Way dwarf spheroidal galaxies by fitting an assumed dark matter profile to the dynamical constraints imposed by either a full Jeans analysis or the $M_{\rm h}$ estimator. Due to uncertainties in the dark matter profile

Table 5.1. Physical properties of Milky Way dwarf spheriodal galaxies.

(1) Name	(2) ℓ (deg)	(3) b (deg)	(4) D (kpc)	(5) L_V ($10^5\,L_\odot$)	(6) $\sigma_\star$ ($\mathrm{km\,s^{-1}}$)	(7) α_h (deg)	(8) r_h (pc)	(9) M_h ($10^5\,M_\odot$)
Bootes I	358.1	69.6	66	0.29	2.4	0.21	242	0.81
Bootes II	353.7	68.9	42	0.01	10.5	0.07	51	3.3
Bootes III	35.4	75.4	47	0.17	14.0	–	–	–
Canes Venatici I	74.3	79.8	218	2.3	7.6	0.15	564	19
Canes Venatici II	113.6	82.7	160	0.079	4.6	0.03	74	0.91
Canis Major	240.0	-8.0	7	490	20.0	–	–	–
Carina	260.1	-22.2	105	3.8	6.6	0.14	250	6.3
Coma Berenices	241.9	83.6	44	0.037	4.6	0.1	77	0.94
Draco	86.4	34.7	76	2.8	9.1	0.17	221	11
Fornax	237.1	-65.7	147	200	11.7	0.28	710	56
Hercules	28.7	36.9	132	0.37	3.7	0.14	330	2.6
Leo I	226.0	49.1	254	55	9.2	0.06	251	12
Leo II	220.2	67.2	233	7.4	6.6	0.04	176	4.5
Leo IV	265.4	56.5	154	0.19	3.3	0.08	206	1.3
Leo V	261.9	58.5	178	0.11	3.7	0.04	135	1.1
Pisces II	79.2	-47.1	182	0.086	–	0.02	58	–
Sagittarius	5.6	-14.2	26	210	11.4	5.7	2587	190
Sculptor	287.5	-83.2	86	23	9.2	0.19	283	14
Segue 1	220.5	50.4	23	0.003	3.9	0.07	29	0.26
Segue 2	149.4	-38.1	35	0.009	3.4	0.06	35	0.23
Sextans	243.5	42.3	86	4.4	7.9	0.46	695	25
Ursa Major I	159.4	54.4	97	0.14	7.6	0.19	319	11
Ursa Major II	152.5	37.4	32	0.041	6.7	0.27	149	3.9
Ursa Minor	105.0	44.8	76	2.8	9.5	0.14	181	9.5
Willman 1	158.6	56.8	38	0.01	4.3	0.04	25	0.27

Column Definitions. — (1) Galaxy name, (2) Galactic longitude, (3) Galactic latitude, (4) distance, (5) visible luminosity, (6) stellar velocity dispersion, (7) stellar half-light angle, (8) stellar half-light radius, and (9) dynamical mass within the half-light radius (calculated using the formalism of Walker *et al.* [63]). Table adapted from McConnachie [37].

and the sparse stellar data sets associated with the ultra-faint dwarf galaxies, there have been many independent attempts to determine J-factors [57, 102–105]. These approaches can differ in the functional form and prior probabilities assumed for the dark matter distribution. However, the strong observational constraints on $M_{\rm h}$ generally lead to consistency in the resulting J-factors as long as they are calculated over angular sizes comparable to the projected half-light radius. In the following sections, we utilize two different techniques for estimating J-factors. For the analysis of 2 years of LAT data (Section 5.3), we calculated J-factors from a full Jeans analysis assuming an NFW profile and derived priors for the dark matter distribution from ΛCDM simulations (Table 5.2). For the analysis of 4 years of LAT data (Section 5.4), we calculated J-factors from the $M_{\rm h}$ estimator for both NFW and Burkert profiles, and we derived priors for the dark matter distribution from the ensemble of Local Group dwarf spheroidal galaxies (Table 5.7). We find that these two analyses are broadly consistent when calculating J-factors within a solid angle cone with a radius of 0.5°.

5.3 2-Year LAT Analysis

In this section we present a search for γ-ray signals coincident with the location of 10 dwarf spheroidal galaxies using 2 years of LAT data. In this analysis, we made two major advances compared to previous γ-ray studies. First, statistical uncertainties in the J-factors of the dwarf galaxies were incorporated as nuisance parameters when fitting for the dark matter annihilation cross section. Second, observations of 10 dwarf galaxies were combined into a single joint likelihood function for improved sensitivity. The resulting constraints represent the first time that γ-ray observations have been used to probe the most generic thermal relic cross section for purely s-wave processes ($\sim 3 \times 10^{-26}\,{\rm cm^3\,s^{-1}}$).

5.3.1 Data Selection

We searched for γ-ray signals coincident with the location of 10 dwarf spheroidal galaxies in 2 years of LAT data recorded between 2008-08-04 and 2010-08-04. We utilized the `Pass-6` event reconstruction and selected `DIFFUSE` class events with energy between 200 MeV and 100 GeV. We analyzed these data with the associated `P6_DIFFUSE_V3` instrument response functions. We rejected events with zenith angles larger than 100° to avoid contamination from Earth limb γ rays, and we discarded time intervals when the observed sky position was occulted by the Earth. We extracted regions of interest (ROIs) of radius 10° around the position of each dwarf galaxy (Table 5.2).

5.3.2 J-factor Determinations

We derived J-factors for 10 dwarf spheroidal galaxies assuming that the dark matter distribution in these dwarfs followed an NFW profile. We used the available velocity dispersion data in radial bins for the 6 classical dwarfs [63], while we used the individual stellar velocities for the ultra-faint dwarfs [106, 107]. We formed a likelihood function by assuming that the line-of-sight velocity measurements were drawn from a Gaussian distribution, adding intrinsic velocity dispersion and measurement error in quadrature (see Equation (13) of Martinez *et al.* [103]). For the binned velocity dispersion data, we used a similar Gaussian likelihood for the velocities but assumed that the intrinsic velocity dispersion dominated over the average measurement error (see Equation (14) of Martinez *et al.* [103]). We found that this approximation could introduce a bias of $\sim 50\%$ to the most probable value of individual J-factors. Since other approximate likelihoods resulted in biases of similar magnitude when compared to the Gaussian likelihood for the individual velocities, we deemed this bias acceptable. Following Section 2.1, we parameterized the NFW profile in terms of $V_{\max}$ and $R_{V_{\max}}$. We assumed a flat prior in $\log(V_{\max})$ and a prior for $R_{V_{\max}}$ given $V_{\max}$ consistent with the Aquarius and Via Lactea II simulations [13, 108]. For the dwarf galaxies with the largest and most accurate stellar data sets (e.g., Draco and Ursa Minor), the resulting J-factors were found to be insensitive to changes in the $\log(V_{\max})$ and $\log(R_{V_{\max}})$ priors [103]. However, for dwarf spheroidals with sparse data sets (e.g., Ursa Major II and Segue 1), the resulting J-factors were prior dependent. For example, adopting the ΛCDM prior for $V_{\max}$ decreased the median J-factor by a factor of ~ 2 for both

Table 5.2. J-factors for the 10 Milky Way dwarf spheroidal galaxies analyzed using 2 years of LAT data.

(1) Name	(2) ℓ (deg)	(3) b (deg)	(4) D (kpc)	(5) $\overline{\log_{10}(J)}$ ($\log_{10}[\,\mathrm{GeV}^2\,\mathrm{cm}^{-5}]$)	(6) Ref.
Bootes I	358.08	69.62	60	17.7 ± 0.34	[106]
Carina	260.11	-22.22	101	18.0 ± 0.13	[63]
Coma Berenices	241.9	83.6	44	19.0 ± 0.37	[107]
Draco	86.37	34.72	80	18.8 ± 0.13	[63]
Fornax	237.1	-65.7	138	17.7 ± 0.23	[63]
Sculptor	287.15	-83.16	80	18.4 ± 0.13	[63]
Segue 1	220.48	50.42	23	19.6 ± 0.53	[109]
Sextans	243.4	42.2	86	17.8 ± 0.23	[63]
Ursa Major II	152.46	37.44	32	19.6 ± 0.40	[107]
Ursa Minor	104.95	44.80	66	18.5 ± 0.18	[63]

Note. — Locations of the dwarf galaxies differ slightly from those listed in Table 5.1 primarily due to inconsistencies in the literature. J-factors were calculated over a solid angle $\Delta\Omega = 2.4 \times 10^{-4}\,\mathrm{sr}$ from a full Jeans analysis assuming an NFW profile (for more details, see Section 5.3.2).

Column Definitions. — (1) Galaxy name, (2) Galactic longitude, (3) Galactic latitude, (4) heliocentric distance, (5) mode and 68% containment of the posterior distribution of $\log_{10}(J)$, and (6) stellar kinematic reference.

Ursa Major II and Segue 1. J-factors were calculated within angular cones of radius 0.5° ($\Delta\Omega = 2.4 \times 10^{-4}\,\mathrm{sr}$) and are listed in Table 5.2. To be conservative, we assumed no boost from dark matter substructure within the dwarf spheroidals. The posterior distributions, as well as the likelihood functions for each J-factor, were well-described by a log-normal function, which we used to include the J-factor uncertainty in the constraints on the dark matter annihilation cross section.

5.3.3 Methods

The Fermi-LAT Collaboration analysis package, `ScienceTools`, was used to perform a binned Poisson likelihood fit over 30 energy bins logarithmically spaced from 200 MeV to 100 GeV and a $10^\circ \times 10^\circ$ square ROI with 0.1° pixels. The diffuse backgrounds were modeled by the standard diffuse emission templates derived from one year of data.[1] Background point-like sources were included from the First LAT Source Catalog [87]. The normalizations of the Galactic and isotropic diffuse γ-ray background components were left free in all ROIs, together with the normalizations of the point sources within 5° of the dwarf galaxy positions. We performed a combined analysis across the dwarfs assuming that the characteristics of the dark matter particle ($m_{\rm DM}$, $\langle\sigma v\rangle$, and annihilation channel branching ratios) were shared. Dark matter annihilation spectra were generated using the `DMFIT` package [110]. Additionally, we incorporated uncertainties on the J-factors into the fitting procedure by adding another term to the likelihood that represents the measurement uncertainties. With this addition, we defined the following joint likelihood

$$\begin{aligned}\tilde{\mathcal{L}}(\boldsymbol{\mu}, \{\boldsymbol{\alpha}\}_i \,|\, \{\mathcal{D}\}_i) = & \prod_i \mathcal{L}_i(\boldsymbol{\mu}, \boldsymbol{\theta}_i \,|\, \mathcal{D}_i) \\ & \times \frac{1}{\ln(10) J_i \sqrt{2\pi}\sigma_i} e^{-\left(\log_{10}(J_i) - \overline{\log_{10}(J_i)}\right)^2 / 2\sigma_i^2} \,,\end{aligned} \tag{5.4}$$

where i indexes the ROIs; $\mathcal{L}_i$ denotes the standard LAT binned Poisson likelihood for a single ROI; $\mathcal{D}_i$ represents the binned γ-ray data in each ROI; $\boldsymbol{\mu}$ represents the set of ROI-independent DM parameters (e.g., $\langle\sigma v\rangle$ and $m_{\rm DM}$); and $\{\boldsymbol{\alpha}\}_i$ are the ROI-dependent model parameters. In this analysis, $\{\boldsymbol{\alpha}\}_i$ included the normalizations of the nearby point and diffuse sources, $\boldsymbol{\theta}_i$, and the J-factor, J_i. The distribution of $\log_{10}(J_i)$ was well modeled by a Gaussian distribution with mean, $\overline{\log_{10}(J_i)}$, and standard deviation, σ_i, given in Table 5.2. When analyzing the LAT data, we approximated the 10 dwarf spheroidal galaxies as point-like γ-ray sources.

For given fixed values of the dark matter mass and annihilation channel, we optimized $\ln\tilde{\mathcal{L}}$, with $\tilde{\mathcal{L}}$ given in Equation (5.4). Nuisance parameters in the likelihood

---

[1] http://fermi.gsfc.nasa.gov/ssc/data/access/lat/BackgroundModels.html

were accounted for using the "profile likelihood" technique (Section 4.2), which involved calculating the profile likelihood $\ln \tilde{\mathcal{L}}_p(\langle \sigma v \rangle)$ by maximizing $\ln \tilde{\mathcal{L}}$ with respect to all other parameters for each fixed value of $\langle \sigma v \rangle$ and m_{DM}. Confidence intervals on $\langle \sigma v \rangle$ were obtained for each m_{DM} by requiring $2\Delta \ln \tilde{\mathcal{L}}_p = 2.71$ for a one-sided 95% confidence level (CL). Both the MINUIT subroutine MINOS [111] and internal Fermi-LAT Collaboration tools were used to implement this technique. Note that statistical uncertainties in the J-factors were treated identically to the uncertainties in the background fit (diffuse and nearby sources). To summarize, the free parameters of the fit were $\langle \sigma v \rangle$, the J-factors, and the normalizations of the nearby point-like and diffuse γ-ray background sources. The coverage of this profile joint likelihood method for calculating confidence intervals was verified using toy Monte Carlo simulations for a Poisson process with known background and LAT simulations of Galactic and isotropic diffuse γ-ray emission. To facilitate convergence of the MINOS fit, the parameter range for $\langle \sigma v \rangle$ was restricted to a lower bound of zero; this resulted in slight over-coverage for small signal strengths [92].

5.3.4 Results

No significant signal was found when analyzing the dwarf galaxies either individually or jointly, and we report upper limits on the annihilation cross section in Figure 5.1 and Figure 5.2. Upper limits derived including J-factor uncertainties were higher than those derived using nominal J-factors. When averaged over the dark matter mass range, the upper limits for individual dwarf galaxies increased by at most a factor of 12 (Segue 1) and at least a factor of 1.2 (Draco). The impact of the J-factor uncertainties was mitigated in the combined limit, where incorporating J-factor uncertainties increased the upper limit by a factor of 1.3 compared to the nominal J-factors.

The combined upper limit curve shown in Figure 5.1 includes Segue 1 and Ursa Major II, two ultra-faint satellites with sparse stellar data sets and correspondingly large J-factor uncertainties. Excluding these objects from the combined analysis increased the upper limit by a factor ~ 1.5, illustrating the robustness of the combined

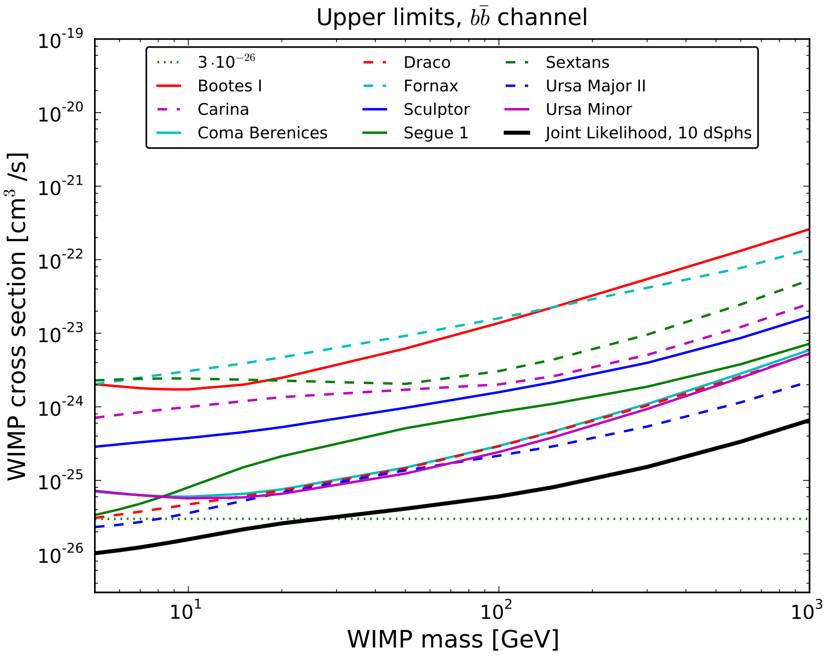

Figure 5.1 Derived 95% CL upper limits on the dark matter annihilation cross section for all 10 dwarf spheroidal galaxies and for the joint likelihood analysis for annihilation into the $b\bar{b}$ final state. The most generic cross section for a purely s-wave annihilation process ($\sim 3 \times 10^{-26}\,\mathrm{cm}^3\,\mathrm{s}^{-1}$) is plotted as a reference. Uncertainties in the J-factor are included.

fit.

We recalculated our combined limits replacing the J-factors of the classical dwarf galaxies with those presented in Charbonnier *et al.* [104], who allowed for dark matter distributions with shallower inner density profiles. The combined limits derived with this replacement agree with those derived from the J-factors in Table 5.2 to about 10%, demonstrating the insensitivity of the combined limits to the assumed dark matter density profile.

Finally, Figure 5.2 shows the combined limits derived for the $b\bar{b}$, $\tau^+\tau^-$, $\mu^+\mu^-$, and W^+W^- annihilation channels. The dark matter particle mass ranges from 5 GeV to 1 TeV, except for the W^+W^- channel, where the lower bound is 100 GeV. The joint likelihood procedure allows us to rule out dark matter annihilation with a cross section predicted by the most generic cosmological calculation up to a mass of $\sim$27 GeV for

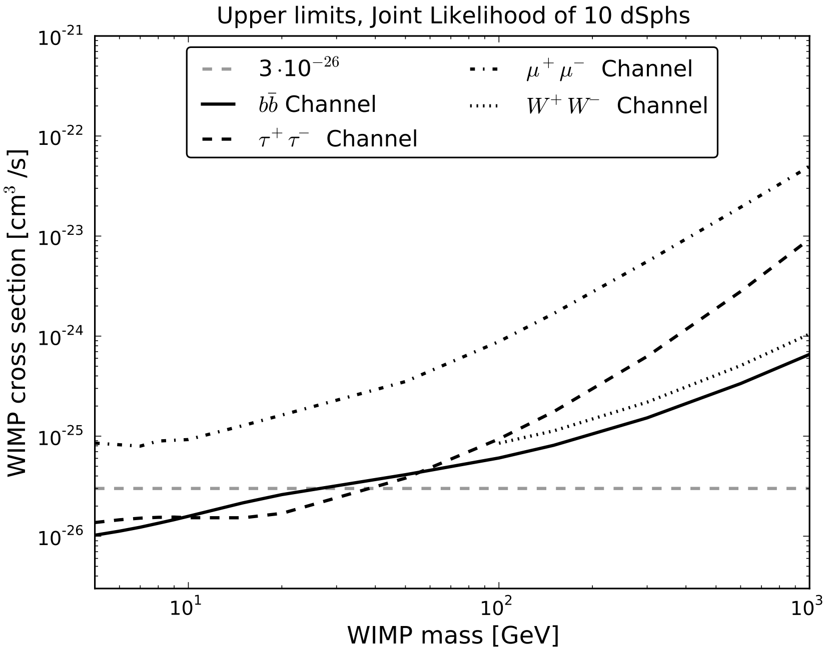

Figure 5.2 Upper limits on the dark matter annihilation cross section for the $b\bar{b}$, $\tau^+\tau^-$, $\mu^+\mu^-$, and W^+W^- channels derived at 95% CL. The most generic cross section for a purely s-wave annihilation process ($\sim 3 \times 10^{-26}\,\mathrm{cm}^3\,\mathrm{s}^{-1}$) is plotted as a reference. Uncertainties in the J-factor are included.

the $b\bar{b}$ channel and up to a mass of $\sim 37\,\mathrm{GeV}$ for the $\tau^+\tau^-$ channel. This is the first time that the most generic annihilation cross section ($\sim 3 \times 10^{-26}\,\mathrm{cm}^3\,\mathrm{s}^{-1}$ for pure s-wave annihilation) has been ruled out using γ-ray observations without assuming additional boost factors from astrophysics or particle physics. For large dark matter particle mass ($\gtrsim 1\,\mathrm{TeV}$), the radiation of soft electro-weak bosons leads to additional γ rays in the LAT energy range [112, 113]. This emission mechanism is not included in the Monte Carlo simulations for the photon yield we employ here [110]. While massive gauge boson radiation is virtually irrelevant for dark matter masses below 100 GeV, our results for the heaviest dark matter masses can be viewed as conservative due to the exclusion of radiative electro-weak corrections.

Table 5.3. LAT 2-year limits on $\langle \sigma v \rangle$ at 95% CL for the $\mu^+\mu^-$ channel (cm^3 s^{-1}).

	5 GeV	10 GeV	50 GeV	100 GeV	150 GeV	300 GeV	600 GeV	1000 GeV
Bootes I	9.62e-24	2.54e-23	1.44e-22	3.34e-22	6.20e-22	2.01e-21	6.92e-21	1.77e-20
Carina	2.87e-24	2.92e-24	1.33e-23	3.90e-23	7.71e-23	2.64e-22	9.40e-22	2.43e-21
Coma Berenices	2.25e-25	5.28e-25	3.21e-24	8.80e-24	1.71e-23	5.76e-23	2.03e-22	5.23e-22
Draco	2.09e-25	3.61e-25	2.87e-24	7.18e-24	1.36e-23	4.45e-23	1.55e-22	3.96e-22
Fornax	1.57e-23	2.57e-23	7.59e-23	1.70e-22	3.12e-22	1.01e-21	3.46e-21	8.80e-21
Sculptor	1.47e-24	2.74e-24	8.57e-24	2.26e-23	4.67e-23	1.59e-22	5.62e-22	1.45e-21
Segue 1	1.00e-24	1.37e-24	3.81e-24	9.41e-24	1.78e-23	5.87e-23	2.04e-22	5.23e-22
Sextans	3.19e-24	4.84e-24	2.80e-23	8.41e-23	1.65e-22	5.65e-22	2.01e-21	5.19e-21
Ursa Major II	2.84e-25	3.65e-25	1.18e-24	2.92e-24	5.51e-24	1.82e-23	6.32e-23	1.62e-22
Ursa Minor	2.05e-25	4.19e-25	2.90e-24	8.14e-24	1.59e-23	5.40e-23	1.91e-22	4.92e-22
Combined	8.52e-26	9.25e-26	3.51e-25	8.82e-25	1.68e-24	5.56e-24	1.94e-23	4.97e-23

Table 5.4. LAT 2-year limits on $\langle \sigma v \rangle$ at 95% CL for the $\tau^+\tau^-$ channel (cm^3 s^{-1}).

	5 GeV	10 GeV	50 GeV	100 GeV	150 GeV	300 GeV	600 GeV	1000 GeV
Bootes I	8.83e-25	1.92e-24	1.72e-23	4.14e-23	7.12e-23	2.20e-22	8.93e-22	2.86e-21
Carina	5.75e-25	4.58e-25	1.24e-24	3.66e-24	7.71e-24	3.25e-23	1.61e-22	5.65e-22
Coma Berenices	3.08e-26	4.60e-26	3.35e-25	9.84e-25	1.97e-24	7.42e-24	3.37e-23	1.13e-22
Draco	3.22e-26	3.98e-26	3.17e-25	8.37e-25	1.53e-24	5.13e-24	2.16e-23	7.03e-23
Fornax	1.88e-24	2.80e-24	6.89e-24	1.49e-23	2.69e-23	9.25e-23	4.05e-22	1.35e-21
Sculptor	1.94e-25	2.66e-25	8.80e-25	2.06e-24	4.02e-24	1.62e-23	8.04e-23	2.83e-22
Segue 1	1.08e-25	2.00e-25	3.92e-25	9.29e-25	1.74e-24	6.27e-24	2.81e-23	9.44e-23
Sextans	9.59e-25	5.46e-25	2.62e-24	8.39e-24	1.81e-23	7.59e-23	3.65e-22	1.25e-21
Ursa Major II	3.04e-26	5.00e-26	1.26e-25	3.01e-25	5.59e-25	1.98e-24	8.77e-24	2.93e-23
Ursa Minor	2.61e-26	3.76e-26	2.93e-25	9.16e-25	1.88e-24	7.27e-24	3.34e-23	1.12e-22
Combined	1.37e-26	1.53e-26	3.81e-26	9.37e-26	1.76e-25	6.27e-25	2.79e-24	9.33e-24

Table 5.5. LAT 2-year limits on $\langle\sigma v\rangle$ at 95% CL for the $b\bar{b}$ channel (cm^3 s^{-1}).

	5 GeV	10 GeV	50 GeV	100 GeV	150 GeV	300 GeV	600 GeV	1000 GeV
Bootes I	2.03e-24	1.73e-24	6.21e-24	1.38e-23	2.26e-23	5.45e-23	1.32e-22	2.60e-22
Carina	7.10e-25	9.95e-25	1.71e-24	2.02e-24	2.61e-24	5.08e-24	1.21e-23	2.53e-23
Coma Berenices	7.05e-26	6.01e-26	1.49e-25	2.95e-25	4.64e-25	1.09e-24	2.82e-24	5.93e-24
Draco	3.08e-26	4.70e-26	1.46e-25	2.91e-25	4.58e-25	1.04e-24	2.58e-24	5.26e-24
Fornax	2.03e-24	3.06e-24	9.23e-24	1.60e-23	2.26e-23	4.14e-23	7.72e-23	1.39e-22
Sculptor	2.87e-25	3.77e-25	9.69e-25	1.58e-24	2.17e-24	3.96e-24	8.62e-24	1.68e-23
Segue 1	3.38e-26	8.05e-26	5.11e-25	8.48e-25	1.10e-24	1.88e-24	3.79e-24	7.20e-24
Sextans	2.29e-24	2.42e-24	2.05e-24	3.06e-24	4.41e-24	9.57e-24	2.46e-23	5.28e-23
Ursa Major II	2.32e-26	3.59e-26	1.37e-25	2.17e-25	2.92e-25	5.40e-25	1.15e-24	2.21e-24
Ursa Minor	7.22e-26	5.71e-26	1.24e-25	2.43e-25	3.87e-25	9.35e-25	2.48e-24	5.31e-24
Combined	1.02e-26	1.58e-26	4.12e-26	6.05e-26	8.10e-26	1.52e-25	3.36e-25	6.57e-25

Table 5.6. LAT 2-year limits on $\langle\sigma v\rangle$ at 95% CL for the W^+W^- channel (cm^3 s^{-1}).

	100 GeV	150 GeV	300 GeV	600 GeV	1000 GeV
Bootes I	1.95e-23	3.25e-23	7.92e-23	2.04e-22	4.28e-22
Carina	3.00e-24	3.81e-24	7.49e-24	1.87e-23	4.14e-23
Coma Berenices	4.16e-25	6.66e-25	1.63e-24	4.51e-24	1.02e-23
Draco	4.17e-25	6.59e-25	1.54e-24	4.01e-24	8.69e-24
Fornax	2.31e-23	3.26e-23	5.79e-23	1.06e-22	1.91e-22
Sculptor	2.31e-24	3.08e-24	5.66e-24	1.27e-23	2.61e-23
Segue 1	1.17e-24	1.51e-24	2.67e-24	5.63e-24	1.11e-23
Sextans	4.47e-24	6.41e-24	1.44e-23	3.90e-23	8.98e-23
Ursa Major II	3.01e-25	4.05e-25	7.69e-25	1.72e-24	3.47e-24
Ursa Minor	3.46e-25	5.59e-25	1.41e-24	4.00e-24	9.32e-24
Combined	8.50e-26	1.13e-25	2.19e-25	5.08e-25	1.05e-24

5.4 4-Year LAT Analysis

This section presents 4-year LAT observations of all 25 know Milky Way dwarf spheroidal galaxies, improving upon the analysis in Section 5.3 in a number of ways. (1) We used a four-year γ-ray data sample that was extended to a photon energy of 500 GeV and reprocessed with an improved instrument response. (2) We used a novel technique to determine the J-factors of dwarf spheroidal galaxies using prior probabilities for the dark matter distribution derived directly from the population of Local Group dwarf galaxies. (3) We derived J-factors for an expanded set of 18 dwarf spheroidal galaxies, and increased the number of dwarf galaxies included in the combined analysis from 10 to 15. (4) We developed a bin-by-bin likelihood technique which allowed us to set flux limits on all 25 known dwarf spheroidal satellite galaxies in a spectrally-independent manner. (5) We utilized spatially extended γ-ray intensity profiles to model the γ-ray emission from the dwarf spheroidals in a manner that was consistent with their dark matter profiles. (6) We performed an extended study of systematics effects arising from uncertainties in the instrument performance, diffuse background modeling, and dark matter distribution. (7) We developed a more advanced statistical treatment to produce expected sensitivity curves from both simulations and random blank fields within the LAT data. (8) We examined six prototypical annihilation channels and extended the dark matter mass range down to 2 GeV and up to 10 TeV. The analysis in this section again constrains the generic thermal relic cross section for low-mass dark matter and greatly expands our understanding of the statistical and systematic issues at play.

5.4.1 Data Selection and Preparation

We selected a data sample corresponding to events collected during the first four years of LAT operation (2008-08-04 to 2012-08-04). We used the `P7REP` data set, which utilized the `Pass-7` event reconstruction and classification scheme [81], but was reprocessed with improved calibrations for the light yield and asymmetry in the calorimeter crystals [114]. The new calorimeter calibrations improved the in-flight point spread function (PSF) above ~ 3 GeV and corrected for the small ($\sim 1\%$ per year), expected degradation in the light yield of the calorimeter crystals measured in flight data. Consequently, the absolute energy scale was shifted upwards by a few percent in an energy- and time-dependent manner. In addition, the re-calibration of the calorimeter light asymmetry led to a statistical re-shuffling of the events classified as photons.

We selected events from the `P7REP CLEAN` class in the energy range from 500 MeV to 500 GeV and within 14° × 14° ROIs centered on the 25 dwarf spheroidal satellite galaxies in Table 5.1. The `CLEAN` event class was chosen to minimize particle backgrounds while preserving effective area. At high Galactic latitudes in the energy range from 1 GeV to 500 GeV, the particle background contamination in the `CLEAN` class is $\sim 30\%$ of the extragalactic diffuse γ-ray background [81], while between 500 MeV and 1 GeV the particle background is subdominant to systematic uncertainties in the diffuse Galactic γ-ray emission. At energies greater than 500 GeV analyses of the extragalactic γ-ray background suggest that the `P7REP CLEAN` class suffers from increased particle contamination [115]. To reduce γ-ray contamination from the bright limb of the Earth, we rejected events with zenith angles larger than 100° and events collected during time periods when the rocking angle of the LAT was greater than 52°.

We created 14° × 14° ROIs by binning the LAT data surrounding each of the 25 dwarf galaxies into spatial pixels of 0.1° and into 24 logarithmically-spaced bins of energy from 500 MeV to 500 GeV. We modeled the diffuse background with a structured Galactic γ-ray emission model (*gll_iem_v05.fit*) and an isotropic contribution from extragalactic γ rays and charged particle contamination (*iso_clean_v05.txt*).[2] We built a model of point-like γ-ray background sources within 15° of each dwarf galaxy beginning with the second LAT source catalog (2FGL) [116]. We then followed the procedure of the 2FGL to find additional point-like background sources that were not yet significantly detected in two years of data and included them in our background model. No new sources were found within 1° of any dwarf galaxy. We used the `P7REP_CLEAN_V15` instrument response functions (IRFs) corresponding to the LAT data set selected above.

---

[2] http://fermi.gsfc.nasa.gov/ssc/data/access/lat/BackgroundModels.html

5.4.2 Methods

The strong dependence of the LAT instrument response on event energy and incident direction motivates the use of a maximum likelihood-based analysis to optimize the sensitivity to faint γ-ray sources. Following the formalism in Chapter 4, we defined a standard LAT binned Poisson likelihood,

$$\mathcal{L}(\boldsymbol{\mu}, \boldsymbol{\theta} \,|\, \mathcal{D}) = \prod_k \frac{\lambda_k^{n_k} e^{-\lambda_k}}{n_k!}, \tag{5.5}$$

as a function of the photon data, $\mathcal{D}$, a set of signal parameters, $\boldsymbol{\mu}$, and a set of background nuisance parameters, $\boldsymbol{\theta}$. The number of observed counts in each energy and spatial bin, indexed by k, depends on the data, $n_k = n_k(\mathcal{D})$, while the number of model-predicted counts depends on the input parameters, $\lambda_k = \lambda_k(\boldsymbol{\mu}, \boldsymbol{\theta})$. This global likelihood function encapsulates information about the observed counts, instrument performance, exposure, and background fluxes, but is heavily dependent on the spectral model assumed for the γ-ray source of interest (Section 4.1).

Since the putative γ-ray signal from dark matter annihilation in dwarf galaxies is not well constrained *a priori*, it is useful to describe the data in a manner that is largely independent of spectral assumptions. Within each energy bin, j, we defined a conditional LAT likelihood function, $\mathcal{L}_j(\boldsymbol{\mu}_j, \hat{\boldsymbol{\theta}} \,|\, \mathcal{D}_j)$, where the nuisance parameters (i.e., the background normalizations) were fixed to their optimal values, $\hat{\boldsymbol{\theta}}$, as derived from the global maximum likelihood fit. The differential signal flux within each bin was modeled by a power law ($\mathrm{d}N/\mathrm{d}E \propto E^{-2}$), and the differential flux normalizations were allowed to vary independently from bin to bin. The set of likelihood functions, $\{\mathcal{L}_j(\boldsymbol{\mu}_j, \hat{\boldsymbol{\theta}} \,|\, \mathcal{D}_j)\}$, or "bin-by-bin" likelihood function, created by allowing the signal flux normalization to vary freely in each bin is largely insensitive to the assumed signal spectrum.[3] A spectrally dependent global likelihood function can be easily re-formed from the bin-by-bin likelihood function by tying the signal normalizations,

---

[3] A second order spectral dependence arises from the convolution of source spectral model *within* each bin with the energy dependent exposure; however, this effect was found to be $\sim 2\%$ for the energy bin size considered here.

$\boldsymbol{\mu} = \{\boldsymbol{\mu}_j\}$, in each bin according to the spectral model of the putative source,

$$\mathcal{L}(\boldsymbol{\mu}, \hat{\boldsymbol{\theta}} \,|\, \mathcal{D}) = \prod_j \mathcal{L}_j(\boldsymbol{\mu}_j, \hat{\boldsymbol{\theta}} \,|\, \mathcal{D}_j). \tag{5.6}$$

Computing a single bin-by-bin likelihood function for each dwarf allowed us to rapidly test many specific spectral models. Note that Equation (5.6) differs from Equation (5.5) due to the fact that the nuisance parameters in Equation (5.6) were fixed at their best fit values.

For each of the 25 dwarf galaxies listed in Table 5.1, we constructed a bin-by-bin likelihood function. In each bin, we set a 95% CL upper limit on the energy flux from the putative signal source using the delta-log-likelihood technique [83, 92]. We compared the observed limits to those expected from 2000 realistic background-only simulations. These simulations included all diffuse and point-like background sources surrounding the dwarf galaxies, and they utilized the in-flight pointing history and instrument response of the LAT. We found that the observed limits were consistent with simulations of the null hypothesis. In Figure 5.3, we show the detailed bin-by-bin LAT likelihood result for the Draco dwarf spheroidal galaxy, while in Figure 5.4 we show the flux upper limits for all 25 dwarf spheroidal galaxies. We emphasize that these bin-by-bin limits are powerful because they make no assumptions about the physical properties of the dark matter particle (e.g., annihilation cross section, decay channel, or mass).

While the bin-by-bin likelihood function is essentially independent of spectral assumptions, it does depend on the spatial model of the target source. The dark matter distribution of some nearby dwarf galaxies may be spatially resolvable by the LAT [104]. Thus, for dwarf galaxies that possess stellar kinematic data sets, we modeled the γ-ray intensity from the line-of-sight integral through the best-fit NFW dark matter distribution derived from stellar kinematic data. Dwarf galaxies that lack stellar kinematic data sets were modeled as point-like γ-ray sources. The modeling of stellar kinematic data is discussed in more detail in Section 5.4.3, and systematic uncertainty associated with the form and spatial extent of the dark matter profile are discussed in Section 5.4.5.

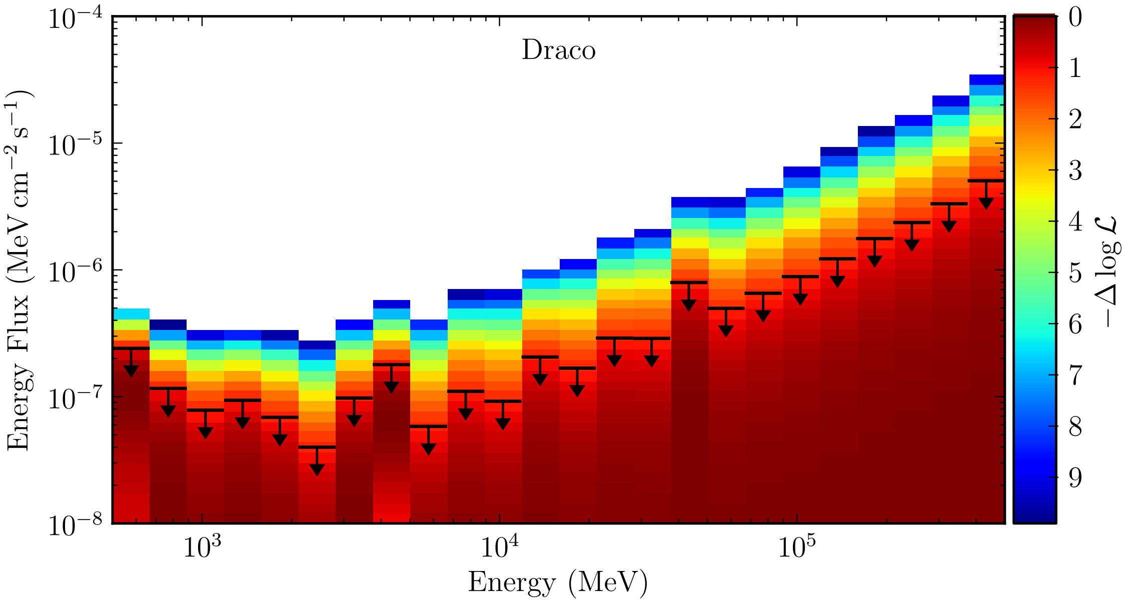

Figure 5.3 Histogram of the bin-by-bin LAT likelihood function used to test for a putative γ-ray source at the position of the Draco dwarf spheroidal galaxy. The bin-by-bin likelihood is calculated by scanning the integrated energy flux of the putative source within each energy bin (equivalent to scanning in the spectral normalization of the source). When performing this scan, the flux normalizations of the background sources are fixed to their optimal values as derived from a maximum likelihood fit over the full energy range. Within each bin, the color scale denotes the variation of the logarithm of the likelihood with respect to the best fit value of the putative source flux. Upper limits on the integrated energy flux are set at 95% CL within each bin using the delta-log-likelihood technique and are largely independent of the putative source spectrum.

5.4.3 J-factor Determinations

J-factors were calculated for a subset of 18 dwarf galaxies possessing dynamical mass estimates constrained by stellar kinematic data sets. Dynamical masses were estimated from the average stellar velocity dispersion and half-light radius of each dwarf galaxy (Section 5.2). We constructed a likelihood function for each individual dwarf galaxy from the observed luminosity, half-light radius, r_{h}, and mass within the half-light radius, M_{h}, together with their associated uncertainties. We derived priors on the relationships between the luminosity, L, maximum circular velocity, $V_{\max}$, and

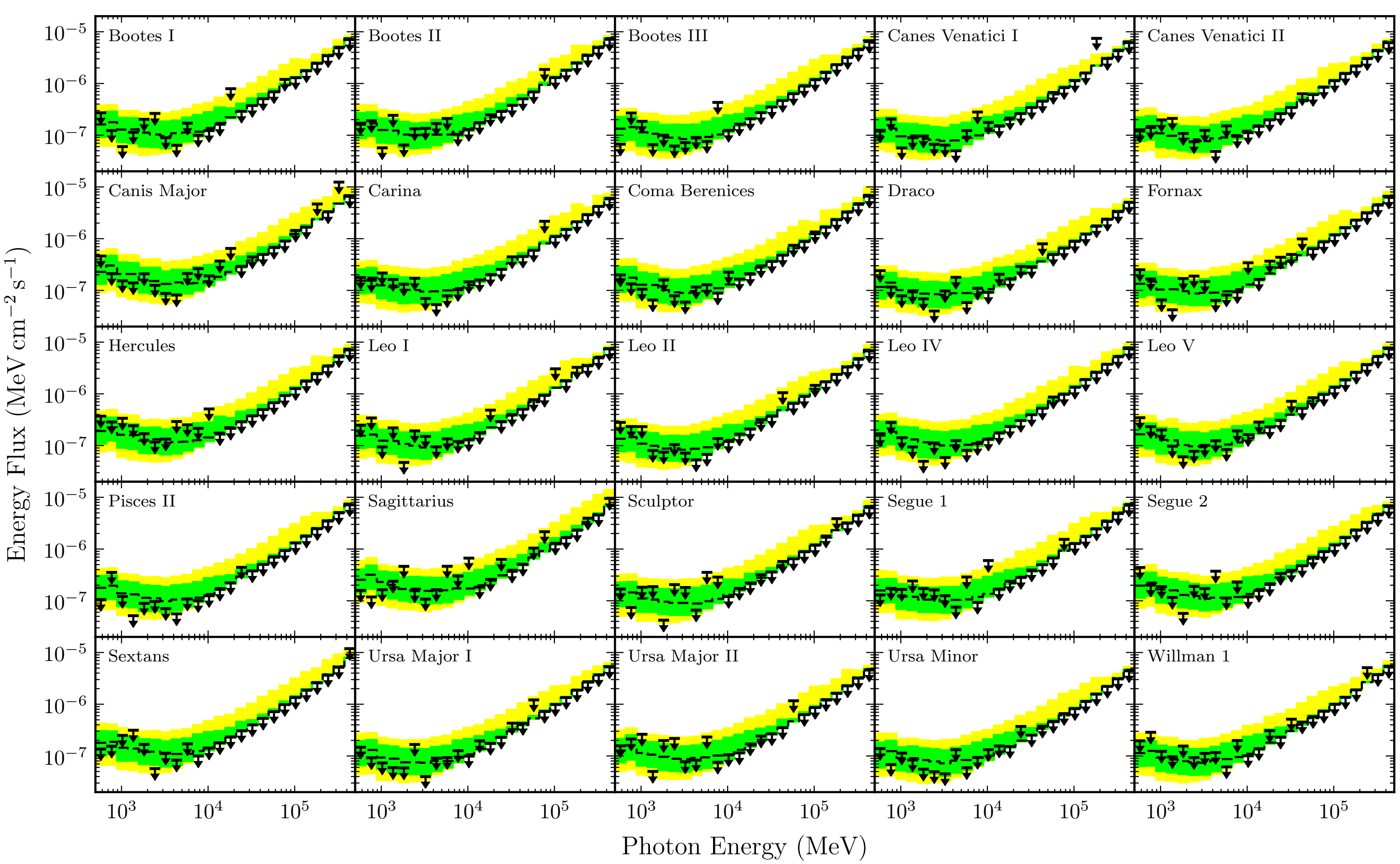

Figure 5.4 Bin-by-bin integrated energy-flux upper limits and expected sensitivity at 95% CL for each dwarf spheroidal galaxy. The expected sensitivity is calculated from 2000 realistic Monte Carlo simulations of the null hypothesis. The median sensitivity is shown by the dashed black line while the 68% and 95% containment regions are indicated by the green and yellow bands, respectively.

radius of maximum circular velocity, $R_{V_{\max}}$, from the ensemble of Local Group dwarf galaxies [11]. By implementing this analysis as a two-level Bayesian hierarchical model [117], we were able to simultaneously constrain both the priors and the resulting likelihoods [105]. This approach utilized all available knowledge of the dark matter distribution in the observed population of dwarf galaxies while mitigating systematic differences between observations and ΛCDM simulations.

While priors on the relationships between, L, $V_{\max}$, and $R_{V_{\max}}$ can be derived from the data, their form must be chosen *a priori.* Motivated by simulations [13, 118], we assumed a prior on the relationship between $R_{V_{\max}}$ and $V_{\max}$ that follows a linear form between $\log(R_{V_{\max}})$ and $\log(V_{\max})$ with some intrinsic Gaussian scatter $\mathcal{N}(\mu, \sigma)$,

$$\mathcal{P}(\log(R_{V_{\max}}) \,|\, \log(V_{\max})) \approx \mathcal{N}(\alpha_{rv} \log(V_{\max}) + \beta_{rv}, \sigma_{rv}). \tag{5.7}$$

Similarly, we assumed that the prior in $\log(V_{\max})$ is linearly related to $\log(L)$ with Gaussian scatter,

$$\mathcal{P}(\log(V_{\max}) \,|\, \log(L)) \approx \mathcal{N}(\alpha_{vl} \log(L) + \beta_{vl}, \sigma_{vl}). \tag{5.8}$$

Finally, we assumed a power-law prior on the galaxy luminosity function [119],

$$\mathcal{P}(L) \approx L^{\alpha_L}. \tag{5.9}$$

The 7 free parameters of these priors, $\{\alpha_{rv}, \beta_{rv}, \sigma_{rv}, \alpha_{vl}, \beta_{vl}, \sigma_{vl}, \alpha_L\}$, were derived from a fit to the full Local Group dwarf galaxy sample. Additionally, each individual dwarf was described by its measured half-light radius, the mass within this radius, the total luminosity, and the associated errors on these quantities. We constrain the full set of parameters with a metropolis nested sampling algorithm with approximately 500,000 points per chain [120].

The inner slope of the dark matter density profile in dwarf galaxies remains a topic of debate (Chapter 2). Thus, we repeated the above procedure for both the cuspy NFW dark matter profile described in Equation (2.1) and the cored Burkert profile described in Equation (2.2). After deriving the halo parameters for each form of the dark matter density profile, we performed the line-of-sight integral (Section 2.2) to calculate the intensity profile and integrated J-factor within an angular radius of 0.5° ($\Delta\Omega \sim 2.4 \times 10^{-4}\,\mathrm{sr}$). Values of the integrated J-factor and spatial extension parameter (defined as the angular size of the scale radius) are listed in Table 5.7. We cross checked these results with those derived from an analysis using priors derived from ΛCDM simulations [57, 93, 103] and flat, "non-informative" priors [11, 104]. We found that the resulting J-factors were consistent within their stated uncertainties. By testing both NFW and Burkert profiles, we confirmed that the integrated J-factor with 0.5° is fairly insensitive to the choice of dark matter profile for central values of the slope < 1.5 [57]. Additionally, the choice of spatial profile had little impact on the γ-ray analysis due to the size of the LAT PSF (see Section 5.4.5).

5.4.4 Constraints on Dark Matter

Individual Dwarf Galaxies

For each of the 25 dwarf galaxies listed in Table 5.1, we created global likelihood functions for six prototypical dark matter annihilation channels (e^+e^-, $\mu^+\mu^-$, $\tau^+\tau^-$, $b\bar{b}$, W^+W^-, and $t\bar{t}$) and a range of particle masses from 2 GeV to 10 TeV (when kinematically allowed). This increased range of dark matter particle masses was made possible through upgrades to the `DMFIT` package [110]. Following Section 4.4, we defined a test statistic (TS) for source detection as the difference in the global log-likelihood between the null ($\boldsymbol{\mu} = \boldsymbol{\mu}_0$) and alternative hypotheses ($\boldsymbol{\mu} = \hat{\boldsymbol{\mu}}$) [116, 121],

$$\mathrm{TS} = -2\ln\left(\frac{\mathcal{L}(\boldsymbol{\mu}_0, \hat{\boldsymbol{\theta}}\,|\,\mathcal{D})}{\mathcal{L}(\hat{\boldsymbol{\mu}}\,, \hat{\boldsymbol{\theta}}\,|\,\mathcal{D})}\right)\,. \tag{5.10}$$

We found that the TS distribution from simulations was well matched to a $\chi^2/2$ distribution with one degree of freedom, as predicted by the theorems of Wilks [85] and Chernoff [86] (Figure 5.6). However, the study of random high-latitude blank fields suggests that the significance calculated from simulations overestimates the true source significance (Section 5.4.5). No significant γ-ray excess was found coincident with any of the dwarfs for any annihilation channel or mass.

Table 5.7. J-factors for the 18 Milky Way dwarf spheroidal galaxies analyzed using 4 years of LAT data.

(1)	(2)	(3)	(4)	(5)	(6)	(7)	(8)	(9)
Name	ℓ (deg)	b (deg)	D (kpc)	$\overline{\log_{10}(\mathrm{J}^{\mathrm{NFW}})}$ ($\log_{10}$[GeV^2 cm^{-5} sr])	$\overline{\alpha_{\mathrm{s}}^{\mathrm{NFW}}}$ (deg)	$\overline{\log_{10}(\mathrm{J}^{\mathrm{Burkert}})}$ ($\log_{10}$[GeV^2 cm^{-5} sr])	$\overline{\alpha_{\mathrm{s}}^{\mathrm{Burkert}}}$ (deg)	Reference
Bootes I	358.1	69.6	66	18.8 ± 0.22	0.22	18.6 ± 0.17	0.08	[126]
Canes Venatici I	74.3	79.8	218	17.7 ± 0.26	0.05	17.6 ± 0.17	0.02	[107]
Canes Venatici II	113.6	82.7	160	17.9 ± 0.25	0.07	17.8 ± 0.19	0.02	[107]
Carina	260.1	-22.2	105	18.1 ± 0.23	0.09	18.1 ± 0.16	0.03	[127]
Coma Berenices	241.9	83.6	44	19.0 ± 0.25	0.23	18.9 ± 0.21	0.07	[107]
Draco	86.4	34.7	76	18.8 ± 0.16	0.26	18.7 ± 0.17	0.10	[128]
Fornax	237.1	-65.7	147	18.2 ± 0.21	0.17	18.1 ± 0.22	0.07	[127]
Hercules	28.7	36.9	132	18.1 ± 0.25	0.08	17.9 ± 0.19	0.03	[107]
Leo I	226.0	49.1	254	17.7 ± 0.18	0.09	17.6 ± 0.17	0.03	[129]
Leo II	220.2	67.2	233	17.6 ± 0.18	0.07	17.5 ± 0.15	0.01	[130]
Leo IV	265.4	56.5	154	17.9 ± 0.28	0.07	17.8 ± 0.21	0.02	[107]
Sculptor	287.5	-83.2	86	18.6 ± 0.18	0.25	18.5 ± 0.17	0.09	[127]
Segue 1	220.5	50.4	23	19.5 ± 0.29	0.36	19.4 ± 0.24	0.11	[109]
Sextans	243.5	42.3	86	18.4 ± 0.27	0.13	18.4 ± 0.16	0.06	[127]
Ursa Major I	159.4	54.4	97	18.3 ± 0.24	0.11	18.2 ± 0.18	0.04	[107]
Ursa Major II	152.5	37.4	32	19.3 ± 0.28	0.32	19.2 ± 0.21	0.11	[107]
Ursa Minor	105.0	44.8	76	18.8 ± 0.19	0.35	18.7 ± 0.20	0.13	[128]
Willman 1	158.6	56.8	38	19.1 ± 0.31	0.25	19.0 ± 0.28	0.07	[131]

Note. — J-factors were calculated over a solid angle $\Delta\Omega = 2.4 \times 10^{-4}$ sr using the velocity dispersion and half-light radius as an estimator for the mass within the half-light radius (for more details, see Section 5.4.3).

Column Definitions. — (1) Galaxy name, (2) Galactic longitude, (3) Galactic latitude, (4) heliocentric distance, (5) mode and 68% containment of the posterior distribution of $\log_{10}(J)$ for an NFW profile, (6) mode of the projected half-light radius assuming an NFW profile, (7) mode and 68% containment of the posterior distribution of $\log_{10}(J)$ for a Burkert profile, (8) mode of the projected half-light radius assuming a Burkert profile, and (9) stellar kinematic reference.

The largest deviation from the null hypothesis was found when fitting the Sagittarius dwarf spheroidal galaxy. This fit yielded a TS ~ 7 across all channels with a preferred dark matter mass ranging from $25\,\mathrm{GeV}$ ($\tau^+\tau^-$) to $100\,\mathrm{GeV}$ ($b\bar{b}$). However, it must be noted that the Sagittarius dwarf is located in a region of intense Galactic foreground emission and is coincident with jet-like structures associated with the Fermi Bubbles [122, 123]. We find that systematic changes to the diffuse modeling methodolgy (Section 5.4.5) can bias the fit of Sagittarius and lead to TS changes of ~ 5. We found that the γ-ray analysis of the Sagittarius region is strongly biased by the modeling of the Galactic diffuse emission. While some authors have suggested a large dark matter component in the Sagittarius dwarf [124], tidal stripping of this system leads to complicated stellar kinematics [125]. For these reasons, we have omitted Sagittarius from the subsequent dark matter constraints.

Using the J-factors derived assuming an NFW profile (Table 5.7), we constrained the thermally-averaged dark matter annihilation cross section for 18 dwarf spheroidal galaxies. We incorporated the statistical uncertainty in the J-factor of each dwarf galaxy as a nuisance parameter in the maximum likelihood formulation. Thus, the likelihood function for each dwarf galaxy, i, was described by

$$\begin{aligned}\tilde{\mathcal{L}}_i(\boldsymbol{\mu}, \boldsymbol{\alpha}_i \,|\, \mathcal{D}_i) =& \mathcal{L}_i(\boldsymbol{\mu}, \hat{\boldsymbol{\theta}}_i \,|\, \mathcal{D}_i) \\ & \times \frac{1}{\ln(10) J_i \sqrt{2\pi}\sigma_i} e^{-(\log_{10}(J_i) - \overline{\log_{10}(J_i)})^2/2\sigma_i^2}.\end{aligned} \tag{5.11}$$

Here, $\mathcal{L}_i$ denotes the individual LAT likelihood function for a single ROI (Equation (5.5)) and $\boldsymbol{\alpha}_i$ includes both the flux normalizations of background γ-ray sources (diffuse and point-like) and the associated dwarf J-factors and their statistical uncertainties.[4] We profiled over the J-factor uncertainties as nuisance parameters to construct a 1-dimensional likelihood function for the annihilation cross section [92]. We note that the J-factor uncertainties must be incorporated as nuisance parameters

---

[4] The likelihood function in Equation (5.11) formally differs from the likelihood function for a single ROI in Equation (5.4) because the background γ-ray source normalizations were fixed to their globally preferred values; however, this choice has a negligible impact on the analysis results.

at the level of the global maximum likelihood fit and not on a bin-by-bin basis. Incorporating J-factor uncertainties on a bin-by-bin basis would result in multi-counting these uncertainties when creating the global likelihood function.

For each of the 18 dwarf galaxies with kinematically determined J-factors, we created global likelihood functions and derived 95% CL upper limits on the dark matter annihilation cross section using the delta-log-likelihood technique (Tables 5.9-5.14). From realistic sky simulations of the regions surrounding each dwarf galaxy, we confirm the well-documented coverage behavior of the delta-log-likelihood technique, making this limit somewhat conservative in most regimes [92]. As can be seen from Table 5.11 and Table 5.12, several dwarf galaxies (i.e. Draco, Coma Berenices, Ursa Major II, and Ursa Minor) independently probe the canonical thermal relic cross section of $3 \times 10^{-26}\,\mathrm{cm}^3\,\mathrm{s}^{-1}$ for low dark matter masses.

Combined Analysis

Assuming that the characteristics of the dark matter particle are shared across the dwarf galaxies, it is possible to increase the sensitivity to weak signals through a combined analysis. We created a joint likelihood function from the product of the individual likelihood functions for each dwarf galaxy,

$$\tilde{\mathcal{L}}(\boldsymbol{\mu}, \{\boldsymbol{\alpha}_i\} \,|\, \mathcal{D}) = \prod_i \tilde{\mathcal{L}}_i(\boldsymbol{\mu}, \boldsymbol{\alpha}_i \,|\, \mathcal{D}_i) \tag{5.12}$$

This joint likelihood function ties the dark matter particle characteristics (i.e., mass, cross section, branching ratio, and thus spectrum) across the individual dwarf galaxies. To select dwarf galaxies for inclusion in the combined analysis, we started from the set of all 25 known dwarf spheroidal galaxies and eliminated the 7 galaxies that lacked kinematically determined J-factors: Bootes II, Bootes III, Canis Major, Leo V, Pisces II, Sagittarius, and Segue 2. To ensure statistical independence between the dwarf observations, when the ROIs of multiple dwarf galaxies overlapped, we retained only the dwarf galaxy with the largest J-factor. This choice eliminated 3 additional dwarfs: Canes Venatici I in favor of Canes Venatici II, Leo I in favor of Segue 1, and Ursa Major I in favor of Willman 1. Thus, we were left with a subset of 15 dwarf spheroidal galaxies as input to the joint likelihood analysis: Bootes I, Canes Venatici II, Carina, Coma Berenices, Draco, Fornax, Hercules, Leo II, Leo IV, Sculptor, Segue 1, Sextans, Ursa Major II, Ursa Minor, and Willman 1.

We estimated the sensitivity of the combined analysis with both a suite of realistic sky simulations (Section 5.4.2) and a set of random high-latitude blank fields in the LAT data (Section 5.4.5). When calculating the expected sensitivity for each dwarf galaxy, we randomized the nominal J-factor in accord with its measurement uncertainty to form an unconditional ensemble [132, 133]. As expected, the sensitivity of the combined analysis depended most heavily on the observations of the dwarf galaxies with the largest J-factors. Specifically, the results of the combined analysis were found to be dominated by Coma Berenices, Draco, Ursa Minor, Segue 1, and Willman 1. The largest deviation from the null hypothesis occured for the $b\bar{b}$ channel and dark matter particle masses between 10 GeV and 25 GeV. This excess corresponds to a local p-value of $p \approx 1.3 \times 10^{-3}$ (Gaussian significance of $\sim 2.9\sigma$). Testing multiple dark matter spectral models introduced a trials factor, which was calculated from simulations. Incorporating this trials factor, the global p-value was found to be $p \approx 2.4 \times 10^{-2}$ (Gaussian significance of $\sim 2.0\sigma$). Additionally, we found that the LAT data do not perfectly match the expected null distribution from simulations and that the global p-value calculated from random blank high-Galactic-latititude sky positions is $p \approx 8.3 \times 10^{-2}$ (Gaussian significance of $\sim 1.4\sigma$). The study of random blanck sky positions is discussed in more detail in Section 5.4.5. The primary contributors to the deviation of the combined analysis from the null hypothesis were the ultra-faint dwarf galaxies, Segue 1, Ursa Major II, and Willman 1. We investigate the impact of removing the ultra-faint dwarf galaxies in Section 5.4.5. Since no significant excess was found, we calculated 95% CL constraints on $\langle \sigma v \rangle$ using the delta-log-likelihood procedure described above.

5.4.5 Systematic Studies

We briefly summarize the procedure for determining the impact of systematic uncertainties on the results of the combined analysis. Specifically, we examine the impact

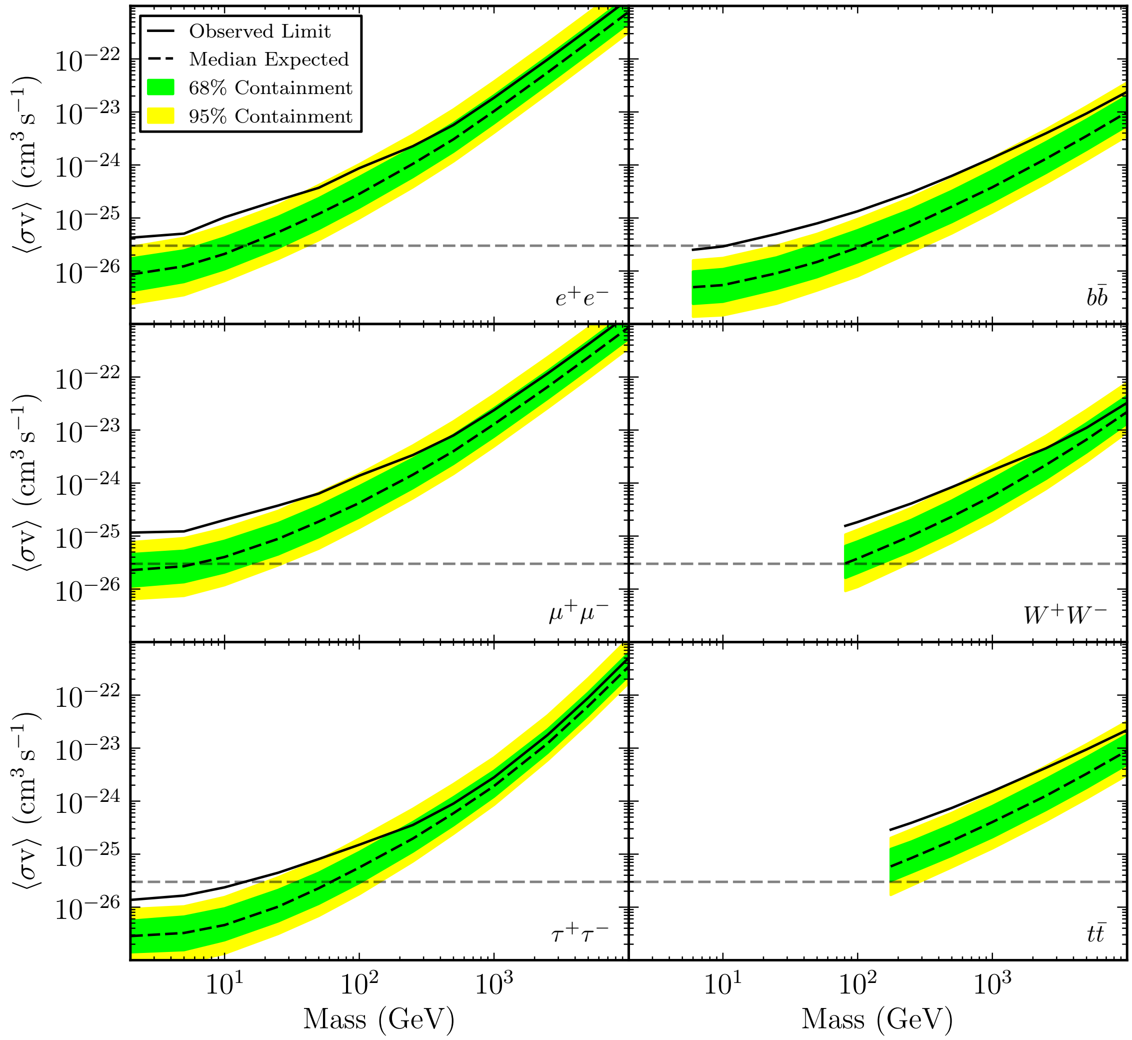

Figure 5.5 Observed limits and expected sensitivity for the dark matter annihilation cross section at 95% CL calculated from a combined analysis of 15 dwarf spheroidal galaxies assuming NFW profiles. The expected sensitivity is derived from 2000 realistic Monte Carlo simulations of the null hypothesis. For each simulation, J-factors are randomly sampled according to the distribution derived from stellar kinematics of each dwarf galaxy. The median sensitivity is shown by the dashed black line while the 68% and 95% containment regions are indicated by the green and yellow bands, respectively.

of uncertainties in the LAT instrument performance, the diffuse interstellar γ-ray emission model, and the assumed dark matter density profile of the dwarf galaxies. A quantitative summary of these results can be found in Table 5.8. Additionally, we discuss the analysis of random blank sky locations to validate the sensitivity and significance determined in Section 5.4.4.

We followed the “bracketing IRF” prescription of Ackermann *et al.* [81] to quantify the impact of uncertainties on the instrument performance. We re-analyzed the LAT data using two sets of IRFs, one meant to maximize the sensitivity of the LAT instrument, and the other meant to minimize it. When creating these bracketing IRFs, we utilized constraints on the systematic uncertainty consistent with Ackermann *et al.* [81]: 10% uncertainty on the effective area, 15% uncertainty on the PSF, and a 5% uncertainty on the energy dispersion. The maximized IRFs increased the effective area, decreased the PSF, and neglected the treatment of the energy dispersion. Conversely, the minimized IRFs decreased the effective area, increased the PSF, and incorporated the energy dispersion into the analysis. For each IRF set we re-ran the full LAT data analysis re-fitting the normalizations of all background sources. The resulting changes in the constraints on the annihilation cross section are shown in Table 5.8.

To quantify the impact of uncertainties on the interstellar emission modeling, we created a set of 8 alternative diffuse models [134]. Following the prescription of Ackermann *et al.* [135], we generated templates for the HI, CO, and inverse Compton (IC) emission using the `GALPROP` cosmic ray (CR) propagation and interaction code.[5] To create 8 reasonably extreme diffuse emission models, we varied the 3 most influential `GALPROP` input parameters as determined by Ackermann *et al.* [135]: the HI spin temperature, the CR source distribution, and the CR propagation halo height. We simultaneously fit the spectral normalizations of the `GALPROP` intensity maps, an isotropic component, and all 2FGL sources to 2 years of LAT data. Additionally, a log-parabola spectral correction was fit to each intensity map in various Galactocentric annuli. When performing the fit, we included templates for Loop I [136] and the Fermi Bubbles [122]. The template for Loop I was based on the geometrical model

---

[5] http://galprop.stanford.edu

of Wolleben [137], while the Fermi Bubbles were assumed to be uniform with edges defined by $R = R_0|\cos\theta|$, where θ is the Galactic polar angle. We re-analyzed the LAT data surrounding the dwarf spheroidals with each of the 8 alternative models, and we recorded the most extreme differences in the upper limits in Table 5.8. Because these diffuse models were constructed using a different methodology than the standard LAT interstellar emission model, the resulting uncertainty should be considered an estimate of the systematic uncertainty due to the interstellar emission modeling process. While these 8 models were chosen to be reasonably extreme, we note that they do not span the full systematic uncertainty involved in modeling the interstellar emission. We also note that these 8 models do not bracket the official LAT interstellar emission model since the methodologies used to create the models differed. While variations between the 8 alternative diffuse models have only a few percent impact on the combined limits (Table 5.8), they can alter the TS of the low-mass excess by as much as 50%.

Stellar kinematic data currently do little to constrain the inner slope of the dark matter density profile in dwarf spheroidal galaxies. In Section 5.4.3 we confirmed that the integrated J-factor within an angular radius of 0.5° is relatively insensitive to the shape of the inner profile [57]. We found that re-analyze the dwarf galaxies assuming a Burkert profile for the dark matter distribution increases the cross section limits by $\sim 15\%$. Additionally, we examined the impact of changing the spatial extension of the NFW profiles used to model the dwarf galaxies. Taking the $\pm 1\sigma$ value of the scale radius (as determined in Section 5.4.3) led to a change of $< 20\%$ in the LAT sensitivity (Table 5.8).

The combined limits presented in Section 5.4.4 include the ultra-faint dwarf galaxies Segue 1, Ursa Major II, and Willman 1. Removing these three dwarf galaxies had a $\pm 20\%$ impact on the combined limits for soft (i.e., $b\bar{b}$) annihilation spectra. However, for hard spectral models (i.e., dark matter particles with $m_{\mathrm{DM}} \gtrsim 500\,\mathrm{GeV}$ annihilating into $\tau^+\tau^-$) removing these dwarfs increased the limits by a factor of ~ 2. As mentioned in Section 5.4.4, these ultra-faint dwarf galaxies contributed heavily to the TS excess observed in the combined analysis. After removing all three ultra-faint dwarfs, the maximum excess was reduced to $\mathrm{TS} \approx 0.5$.

We compared the expected sensitivity derived from simulations (Figure 5.5) to that derived from a control sample of randomly selected blank sky locations (Figure 5.7). Blank sky locations were chosen randomly at high Galactic latitude ($|b| > 30^{\circ}$) and far from any 2FGL catalog sources ($> 1^{\circ}$ from point-like sources and $> 5^{\circ}$ from spatially extended sources). Sets of 25 blank-sky locations were chosen to correspond to the 25 dwarf galaxies (separated by $> 7^{\circ}$). The local point-like and diffuse background sources were fit in each blank sky location and bin-by-bin and global likelihood functions were calculated. Each set of random sky locations were mapped one-to-one to the dwarf galaxies, and nominal J-factors were randomized according to the uncertainty derived from kinematic measurements. We formed a joint likelihood function from sets of 15 random locations to conform to the 15 dwarfs used in the combined analysis of Section 5.4.4.

In Figure 5.7 we show the expected sensitivity from 300 combined analyses on randomly selected locations. It can be seen that the observed limits are more consistent with the expected sensitivity calculated from blank sky regions (Figure 5.7) than the expected sensitivity calculated from simulations (Figure 5.5). Additionally, we plot the distribution of TS values for both simulations and random sky locations in Figure 5.6. It is clear that the TS distribution in the random sky locations deviates from the expectation derived from asymptotic theorems. The analysis of LAT data is known to be complicated by un-resolved point-like background sources, an imperfect model of the diffuse background emission, and percent-level inconsistencies in the determination of the instrument acceptance. Each of these systematic effects is a plausible contributor to deviations from the asymptotic expectations and suggest that the asymptotic significance calculated in Section 5.4.4 overestimates the true significance. While the study of random sky locations suffers from limited statistics, increasing the number of randomly selected locations would reduce the independence of each trial.

Table 5.8. Systematic uncertainties on the 4-year LAT dwarf spheroidal analysis.

		10 GeV	100 GeV	1000 GeV	10000 GeV
ee	IRFs	+14%/-12%	+12%/-10%	+11%/-9%	+11%/-9%
	Diffuse	+3%/-4%	+3%/-3%	+1%/-1%	+1%/-1%
	Extension	+7%/-5%	+17%/-11%	+11%/-6%	+10%/-6%
$\mu^+\mu^-$	IRFs	+15%/-12%	+12%/-10%	+11%/-9%	+11%/-9%
	Diffuse	+4%/-5%	+3%/-4%	+2%/-1%	+1%/-1%
	Extension	+7%/-5%	+15%/-10%	+11%/-6%	+10%/-6%
$\tau^+\tau^-$	IRFs	+15%/-13%	+12%/-10%	+13%/-11%	+12%/-10%
	Diffuse	+5%/-5%	+1%/-5%	+1%/-1%	+1%/-1%
	Extension	+6%/-4%	+14%/-9%	+13%/-7%	+6%/-3%
$b\bar{b}$	IRFs	+15%/-13%	+14%/-12%	+12%/-10%	+11%/-9%
	Diffuse	+10%/-3%	+4%/-5%	+2%/-4%	+2%/-3%
	Extension	+3%/-2%	+8%/-6%	+12%/-8%	+12%/-7%
W^+W^-	IRFs	–	+14%/-12%	+12%/-10%	+13%/-11%
	Diffuse	–	+4%/-4%	+2%/-4%	+1%/-1%
	Extension	–	+8%/-6%	+13%/-8%	+14%/-8%
$t\bar{t}$	IRFs	–	–	+12%/-11%	+11%/-9%
	Diffuse	–	–	+2%/-3%	+2%/-3%
	Extension	–	–	+11%/-8%	+13%/-8%

Note. — Systematic uncertainties have been decomposed into contributions from the instrument response functions (IRFs), diffuse modeling (Diffuse), and spatial extension of the dark matter distribution (Extension). Entries represent the percentage change to the observed upper limits on the dark matter annihilation cross section from varying each component individually.

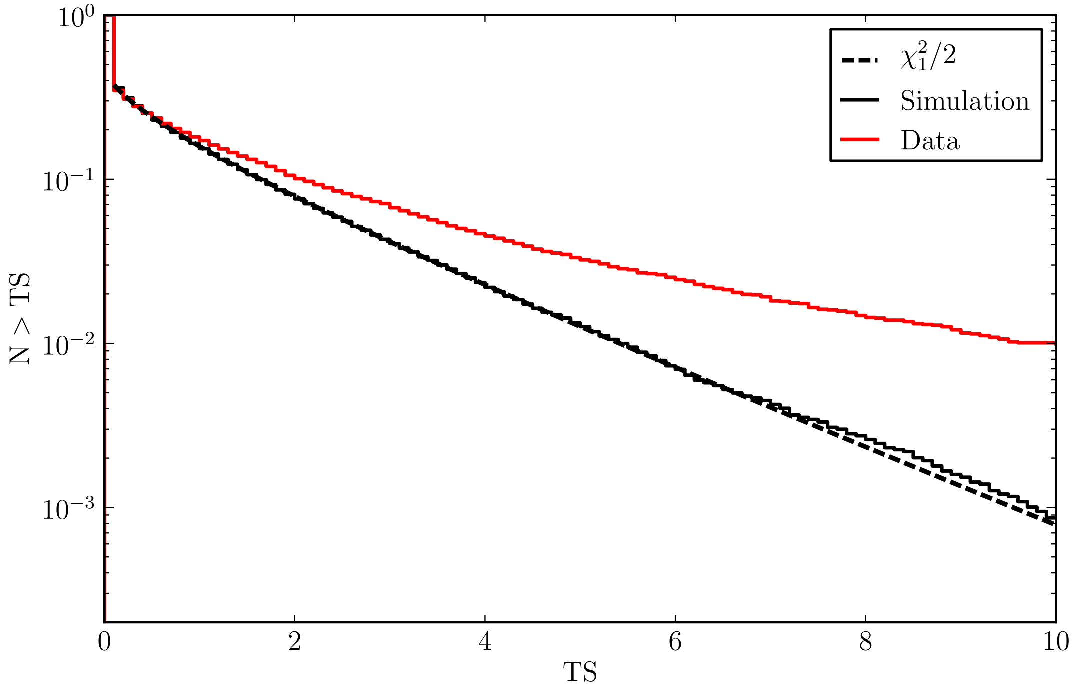

Figure 5.6 Distribution of TS values for fits of a 25 GeV $b\bar{b}$ annihilation spectrum to the null hypothesis generated from 50000 realistic Monte Carlo simulations and 7500 random high-latitude blank-sky locations. The dashed line shows the expectation from the asymptotic theorems of Chernoff [86] and Wilks [85].

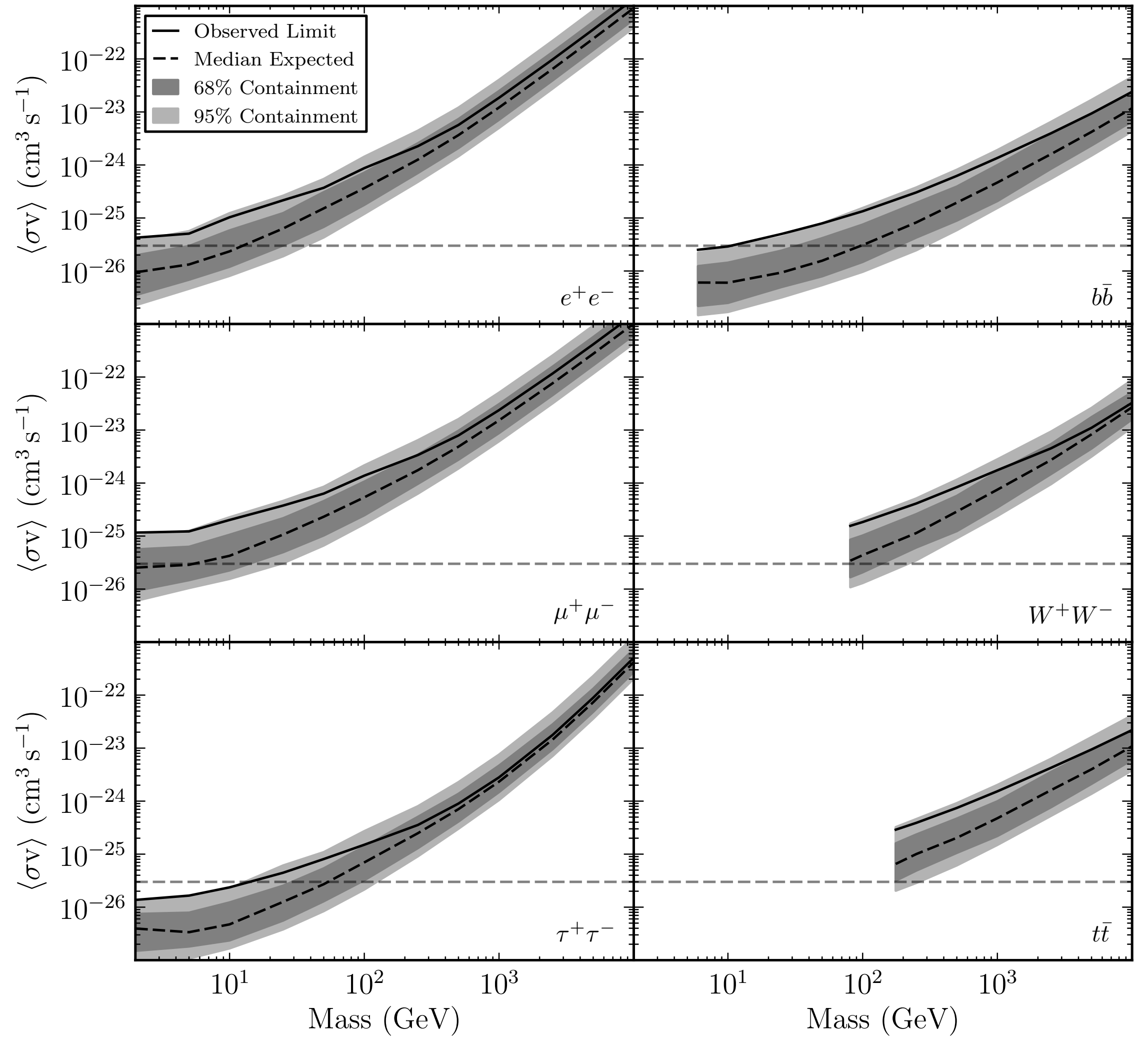

Figure 5.7 Observed limits and expected sensitivity for the dark matter annihilation cross section at 95% CL calculated from a combined analysis of 15 dwarf spheroidal galaxies assuming NFW profiles. The expected sensitivity is derived from 300 randomly-selected high-Galactic-latitude blank data fields. For each random location, J-factors are randomly sampled according to the distribution derived from stellar kinematics of each dwarf galaxy. The median sensitivity from blank fields is shown by the dashed black line while the 68% and 95% containment regions are indicated by the dark and light gray bands, respectively.

Table 5.9. LAT 4-year limits on $\langle \sigma v \rangle$ at 95% CL for the e^+e^- channel ($\mathrm{cm}^3\ \mathrm{s}^{-1}$).

	2 GeV	5 GeV	10 GeV	25 GeV	50 GeV	100 GeV	250 GeV	500 GeV	1000 GeV	2500 GeV	5000 GeV	10000 GeV
Bootes I	1.49e-25	2.12e-25	3.26e-25	1.68e-24	3.80e-24	9.81e-24	3.74e-23	1.09e-22	3.71e-22	2.01e-21	7.45e-21	2.82e-20
Bootes II	–	–	–	–	–	–	–	–	–	–	–	–
Bootes III	–	–	–	–	–	–	–	–	–	–	–	–
Canes Venatici I	1.35e-24	1.20e-24	5.51e-24	1.51e-23	3.58e-23	9.33e-23	4.18e-22	1.28e-21	4.46e-21	2.47e-20	9.23e-20	3.50e-19
Canes Venatici II	2.42e-24	2.21e-24	3.16e-24	5.42e-24	1.20e-23	3.05e-23	1.23e-22	3.84e-22	1.34e-21	7.47e-21	2.79e-20	1.06e-19
Canis Major	–	–	–	–	–	–	–	–	–	–	–	–
Carina	1.06e-24	9.76e-25	9.94e-25	2.10e-24	4.99e-24	3.65e-23	1.54e-22	4.86e-22	1.71e-21	9.53e-21	3.57e-20	1.35e-19
Coma Berenices	7.90e-26	8.25e-26	1.43e-25	3.72e-25	8.71e-25	2.34e-24	9.75e-24	3.08e-23	1.09e-22	6.05e-22	2.26e-21	8.60e-21
Draco	6.26e-26	1.41e-25	2.11e-25	5.23e-25	1.35e-24	3.21e-24	1.18e-23	3.46e-23	1.19e-22	6.49e-22	2.41e-21	9.14e-21
Fornax	3.76e-25	1.05e-24	1.43e-24	3.80e-24	1.01e-23	2.34e-23	8.50e-23	2.49e-22	8.53e-22	4.66e-21	1.73e-20	6.56e-20
Hercules	2.33e-24	3.34e-24	7.95e-24	1.71e-23	3.40e-23	7.75e-23	2.68e-22	7.54e-22	2.51e-21	1.34e-20	4.96e-20	1.87e-19
Leo I	1.75e-24	3.14e-24	4.01e-24	9.14e-24	1.90e-23	5.03e-23	2.19e-22	6.79e-22	2.38e-21	1.32e-20	4.93e-20	1.87e-19
Leo II	2.78e-24	1.80e-24	2.26e-24	5.52e-24	1.48e-23	4.12e-23	1.79e-22	5.74e-22	2.03e-21	1.14e-20	4.26e-20	1.62e-19
Leo IV	5.89e-25	7.87e-25	1.22e-24	3.42e-24	8.82e-24	2.54e-23	1.13e-22	3.68e-22	1.31e-21	7.37e-21	2.77e-20	1.05e-19
Leo V	–	–	–	–	–	–	–	–	–	–	–	–
Pisces II	–	–	–	–	–	–	–	–	–	–	–	–
Sagittarius	–	–	–	–	–	–	–	–	–	–	–	–
Sculptor	1.36e-25	3.24e-25	1.16e-24	2.76e-24	5.98e-24	1.36e-23	4.64e-23	1.27e-22	4.23e-22	2.27e-21	8.39e-21	3.17e-20
Segue 1	7.38e-26	9.73e-26	2.81e-25	7.46e-25	1.57e-24	3.85e-24	1.30e-23	3.46e-23	1.13e-22	5.97e-22	2.19e-21	8.25e-21
Segue 2	–	–	–	–	–	–	–	–	–	–	–	–
Sextans	1.18e-24	7.97e-25	9.34e-25	1.76e-24	3.94e-24	1.04e-23	4.32e-23	1.39e-22	4.91e-22	2.75e-21	1.03e-20	3.92e-20
Ursa Major I	1.35e-25	2.96e-25	5.08e-25	1.24e-24	3.02e-24	9.20e-24	3.79e-23	1.18e-22	4.13e-22	2.29e-21	8.57e-21	3.25e-20
Ursa Major II	9.92e-26	1.49e-25	2.73e-25	3.92e-25	6.69e-25	2.42e-24	8.47e-24	2.41e-23	8.20e-23	4.45e-22	1.65e-21	6.24e-21
Ursa Minor	5.80e-26	8.27e-26	1.30e-25	4.03e-25	9.83e-25	2.50e-24	9.78e-24	2.98e-23	1.03e-22	5.71e-22	2.13e-21	8.08e-21
Willman 1	2.00e-25	2.79e-25	4.52e-25	1.10e-24	2.65e-24	6.45e-24	2.36e-23	6.81e-23	2.29e-22	1.23e-21	4.56e-21	1.72e-20
Combined	4.24e-26	5.07e-26	1.03e-25	2.16e-25	3.71e-25	8.71e-25	2.26e-24	5.68e-24	1.85e-23	9.78e-23	3.59e-22	1.35e-21

Table 5.10. LAT 4-year limits on $\langle\sigma v\rangle$ at 95% CL for the $\mu^+\mu^-$ channel (cm^3 s^{-1}).

	2 GeV	5 GeV	10 GeV	25 GeV	50 GeV	100 GeV	250 GeV	500 GeV	1000 GeV	2500 GeV	5000 GeV	10000 GeV
Bootes I	3.59e-25	5.05e-25	6.64e-25	2.64e-24	5.69e-24	1.39e-23	5.04e-23	1.43e-22	4.59e-22	2.36e-21	8.49e-21	3.14e-20
Bootes II	–	–	–	–	–	–	–	–	–	–	–	–
Bootes III	–	–	–	–	–	–	–	–	–	–	–	–
Canes Venatici I	3.66e-24	2.74e-24	9.59e-24	2.38e-23	5.35e-23	1.32e-22	5.44e-22	1.62e-21	5.40e-21	2.86e-20	1.04e-19	3.89e-19
Canes Venatici II	6.31e-24	5.51e-24	6.77e-24	9.63e-24	1.87e-23	4.39e-23	1.64e-22	4.87e-22	1.62e-21	8.62e-21	3.15e-20	1.18e-19
Canis Major	–	–	–	–	–	–	–	–	–	–	–	–
Carina	2.81e-24	2.53e-24	2.10e-24	3.57e-24	7.57e-24	4.99e-23	1.99e-22	6.09e-22	2.05e-21	1.10e-20	4.02e-20	1.50e-19
Coma Berenices	2.02e-25	1.77e-25	2.61e-25	6.01e-25	1.31e-24	3.28e-24	1.28e-23	3.88e-23	1.30e-22	6.96e-22	2.55e-21	9.54e-21
Draco	1.87e-25	2.83e-25	3.88e-25	8.60e-25	2.00e-24	4.61e-24	1.60e-23	4.49e-23	1.46e-22	7.57e-22	2.74e-21	1.02e-20
Fornax	9.70e-25	2.21e-24	2.81e-24	6.30e-24	1.49e-23	3.37e-23	1.15e-22	3.23e-22	1.05e-21	5.43e-21	1.97e-20	7.31e-20
Hercules	6.53e-24	7.46e-24	1.49e-23	2.93e-23	5.47e-23	1.17e-22	3.77e-22	1.02e-21	3.17e-21	1.59e-20	5.69e-20	2.09e-19
Leo I	5.62e-24	7.04e-24	8.27e-24	1.54e-23	2.96e-23	7.14e-23	2.88e-22	8.58e-22	2.87e-21	1.52e-20	5.56e-20	2.08e-19
Leo II	8.61e-24	4.91e-24	4.55e-24	9.03e-24	2.15e-23	5.64e-23	2.31e-22	7.14e-22	2.43e-21	1.30e-20	4.79e-20	1.79e-19
Leo IV	1.87e-24	1.65e-24	2.24e-24	5.38e-24	1.28e-23	3.46e-23	1.44e-22	4.55e-22	1.56e-21	8.43e-21	3.10e-20	1.16e-19
Leo V	–	–	–	–	–	–	–	–	–	–	–	–
Pisces II	–	–	–	–	–	–	–	–	–	–	–	–
Sagittarius	–	–	–	–	–	–	–	–	–	–	–	–
Sculptor	3.99e-25	7.06e-25	2.07e-24	4.55e-24	9.38e-24	2.06e-23	6.63e-23	1.72e-22	5.34e-22	2.69e-21	9.61e-21	3.55e-20
Segue 1	1.84e-25	2.27e-25	5.06e-25	1.24e-24	2.48e-24	5.71e-24	1.85e-23	4.79e-23	1.45e-22	7.13e-22	2.53e-21	9.28e-21
Segue 2	–	–	–	–	–	–	–	–	–	–	–	–
Sextans	2.97e-24	2.12e-24	2.02e-24	3.03e-24	6.08e-24	1.47e-23	5.67e-23	1.74e-22	5.88e-22	3.16e-21	1.16e-20	4.34e-20
Ursa Major I	3.80e-25	6.19e-25	9.30e-25	2.01e-24	4.50e-24	1.26e-23	4.94e-23	1.48e-22	4.97e-22	2.64e-21	9.66e-21	3.61e-20
Ursa Major II	2.64e-25	3.55e-25	5.52e-25	7.49e-25	1.13e-24	3.50e-24	1.16e-23	3.17e-23	1.01e-22	5.21e-22	1.88e-21	6.96e-21
Ursa Minor	1.61e-25	1.65e-25	2.34e-25	6.22e-25	1.45e-24	3.53e-24	1.30e-23	3.80e-23	1.25e-22	6.62e-22	2.41e-21	8.98e-21
Willman 1	5.43e-25	6.50e-25	9.06e-25	1.85e-24	4.07e-24	9.44e-24	3.26e-23	9.08e-23	2.87e-22	1.46e-21	5.21e-21	1.93e-20
Combined	1.16e-25	1.22e-25	2.01e-25	3.77e-25	6.33e-25	1.38e-24	3.38e-24	7.92e-24	2.37e-23	1.17e-22	4.13e-22	1.52e-21

Table 5.11. LAT 4-year limits on $\langle \sigma v \rangle$ at 95% CL for the $\tau^+\tau^-$ channel (cm^3 s^{-1}).

	2 GeV	5 GeV	10 GeV	25 GeV	50 GeV	100 GeV	250 GeV	500 GeV	1000 GeV	2500 GeV	5000 GeV	10000 GeV
Bootes I	4.04e-26	6.74e-26	9.99e-26	2.17e-25	6.34e-25	1.78e-24	7.46e-24	2.19e-23	6.71e-23	4.02e-22	2.01e-21	1.15e-20
Bootes II	–	–	–	–	–	–	–	–	–	–	–	–
Bootes III	–	–	–	–	–	–	–	–	–	–	–	–
Canes Venatici I	5.54e-25	4.20e-25	7.48e-25	2.62e-24	6.66e-24	1.78e-23	6.86e-23	2.22e-22	8.41e-22	6.05e-21	3.17e-20	1.81e-19
Canes Venatici II	5.25e-25	8.30e-25	9.41e-25	1.15e-24	2.00e-24	4.86e-24	2.16e-23	7.62e-23	2.97e-22	2.17e-21	1.12e-20	6.21e-20
Canis Major	–	–	–	–	–	–	–	–	–	–	–	–
Carina	2.87e-25	4.24e-25	3.54e-25	4.10e-25	8.23e-25	3.96e-24	2.90e-23	1.06e-22	4.15e-22	2.98e-21	1.52e-20	8.25e-20
Coma Berenices	3.15e-26	2.26e-26	2.99e-26	7.01e-26	1.61e-25	4.24e-25	1.88e-24	6.58e-24	2.55e-23	1.85e-22	9.56e-22	5.25e-21
Draco	3.35e-26	1.95e-26	4.18e-26	1.04e-25	2.26e-25	5.78e-25	2.23e-24	6.80e-24	2.37e-23	1.59e-22	8.12e-22	4.53e-21
Fornax	1.94e-25	2.37e-25	3.51e-25	7.10e-25	1.47e-24	4.01e-24	1.65e-23	5.05e-23	1.74e-22	1.16e-21	5.86e-21	3.26e-20
Hercules	7.94e-25	8.17e-25	1.39e-24	3.52e-24	6.82e-24	1.42e-23	4.23e-23	1.03e-22	3.20e-22	2.09e-21	1.10e-20	6.56e-20
Leo I	9.35e-25	8.84e-25	1.10e-24	1.70e-24	3.34e-24	8.25e-24	3.83e-23	1.41e-22	5.51e-22	3.90e-21	1.98e-20	1.08e-19
Leo II	1.51e-24	9.68e-25	6.13e-25	9.51e-25	2.22e-24	6.75e-24	3.55e-23	1.32e-22	5.18e-22	3.74e-21	1.91e-20	1.04e-19
Leo IV	5.03e-25	2.06e-25	2.54e-25	5.96e-25	1.49e-24	4.47e-24	2.28e-23	8.53e-23	3.44e-22	2.56e-21	1.32e-20	7.15e-20
Leo V	–	–	–	–	–	–	–	–	–	–	–	–
Pisces II	–	–	–	–	–	–	–	–	–	–	–	–
Sagittarius	–	–	–	–	–	–	–	–	–	–	–	–
Sculptor	4.51e-26	8.13e-26	2.03e-25	5.42e-25	1.17e-24	2.48e-24	6.33e-24	1.70e-23	5.84e-23	4.05e-22	2.13e-21	1.24e-20
Segue 1	1.19e-26	2.97e-26	4.91e-26	1.38e-25	2.96e-25	6.70e-25	1.89e-24	4.40e-24	1.34e-23	8.73e-23	4.56e-22	2.69e-21
Segue 2	–	–	–	–	–	–	–	–	–	–	–	–
Sextans	1.89e-25	3.51e-25	3.35e-25	3.58e-25	6.77e-25	1.72e-24	7.83e-24	2.82e-23	1.13e-22	8.61e-22	4.55e-21	2.53e-20
Ursa Major I	7.77e-26	7.12e-26	1.06e-25	2.40e-25	5.40e-25	1.54e-24	7.63e-24	2.69e-23	1.00e-22	6.90e-22	3.48e-21	1.90e-20
Ursa Major II	3.30e-26	4.68e-26	7.17e-26	1.05e-25	1.43e-25	3.25e-25	1.44e-24	4.72e-24	1.63e-23	1.05e-22	5.17e-22	2.86e-21
Ursa Minor	2.23e-26	1.66e-26	2.49e-26	6.60e-26	1.76e-25	4.91e-25	2.01e-24	6.36e-24	2.29e-23	1.57e-22	8.04e-22	4.45e-21
Willman 1	7.05e-26	7.91e-26	1.09e-25	1.93e-25	4.15e-25	1.07e-24	3.65e-24	9.61e-24	3.13e-23	2.11e-22	1.11e-21	6.53e-21
Combined	1.37e-26	1.65e-26	2.37e-26	4.46e-26	8.08e-26	1.50e-25	3.55e-25	9.00e-25	2.81e-24	1.78e-23	8.93e-23	5.06e-22

Table 5.12. LAT 4-year limits on $\langle \sigma v \rangle$ at 95% CL for the $b\bar{b}$ channel (cm^3 s^{-1}).

	6 GeV	10 GeV	25 GeV	50 GeV	100 GeV	250 GeV	500 GeV	1000 GeV	2500 GeV	5000 GeV	10000 GeV
Bootes I	7.83e-26	9.41e-26	1.78e-25	3.08e-25	6.29e-25	1.94e-24	4.62e-24	1.16e-23	4.30e-23	1.18e-22	3.40e-22
Bootes II	–	–	–	–	–	–	–	–	–	–	–
Bootes III	–	–	–	–	–	–	–	–	–	–	–
Canes Venatici I	8.66e-25	7.99e-25	1.40e-24	2.88e-24	6.10e-24	1.80e-23	4.38e-23	1.14e-22	4.31e-22	1.24e-21	3.69e-21
Canes Venatici II	1.18e-24	1.38e-24	2.13e-24	3.00e-24	4.42e-24	8.26e-24	1.67e-23	3.90e-23	1.39e-22	3.86e-22	1.12e-21
Canis Major	–	–	–	–	–	–	–	–	–	–	–
Carina	5.83e-25	6.87e-25	9.33e-25	1.08e-24	1.42e-24	3.53e-24	1.11e-23	3.72e-23	1.54e-22	4.47e-22	1.33e-21
Coma Berenices	4.59e-26	4.21e-26	5.86e-26	9.38e-26	1.73e-25	4.65e-25	1.09e-24	2.76e-24	1.03e-23	2.94e-23	8.67e-23
Draco	4.87e-26	4.52e-26	7.47e-26	1.32e-25	2.53e-25	6.82e-25	1.62e-24	3.95e-24	1.40e-23	3.83e-23	1.09e-22
Fornax	2.97e-25	3.49e-25	6.35e-25	1.09e-24	2.00e-24	5.28e-24	1.18e-23	2.89e-23	1.02e-22	2.76e-22	7.78e-22
Hercules	1.42e-24	1.55e-24	2.95e-24	5.33e-24	9.74e-24	2.32e-23	4.94e-23	1.12e-22	3.66e-22	9.68e-22	2.69e-21
Leo I	1.57e-24	1.63e-24	2.37e-24	3.48e-24	5.48e-24	1.22e-23	2.62e-23	6.32e-23	2.34e-22	6.61e-22	1.94e-21
Leo II	2.29e-24	2.09e-24	2.16e-24	2.16e-24	3.06e-24	7.30e-24	1.72e-23	4.53e-23	1.77e-22	5.14e-22	1.53e-21
Leo IV	5.70e-25	4.39e-25	5.16e-25	7.93e-25	1.48e-24	4.17e-24	1.04e-23	2.76e-23	1.10e-22	3.21e-22	9.68e-22
Leo V	–	–	–	–	–	–	–	–	–	–	–
Pisces II	–	–	–	–	–	–	–	–	–	–	–
Sagittarius	–	–	–	–	–	–	–	–	–	–	–
Sculptor	8.90e-26	1.18e-25	3.05e-25	6.34e-25	1.31e-24	3.59e-24	8.18e-24	1.94e-23	6.55e-23	1.74e-22	4.81e-22
Segue 1	3.13e-26	4.36e-26	9.39e-26	1.80e-25	3.62e-25	9.68e-25	2.17e-24	5.22e-24	1.77e-23	4.71e-23	1.31e-22
Segue 2	–	–	–	–	–	–	–	–	–	–	–
Sextans	4.82e-25	5.76e-25	8.54e-25	1.04e-24	1.30e-24	2.52e-24	5.33e-24	1.28e-23	4.68e-23	1.32e-22	3.89e-22
Ursa Major I	1.11e-25	1.13e-25	1.87e-25	3.15e-25	5.90e-25	1.61e-24	3.87e-24	1.01e-23	3.89e-23	1.12e-22	3.30e-22
Ursa Major II	5.87e-26	7.36e-26	1.38e-25	2.17e-25	3.43e-25	6.92e-25	1.37e-24	3.09e-24	1.05e-23	2.82e-23	7.85e-23
Ursa Minor	3.46e-26	3.27e-26	4.75e-26	7.98e-26	1.59e-25	4.65e-25	1.15e-24	2.94e-24	1.08e-23	3.01e-23	8.75e-23
Willman 1	1.22e-25	1.38e-25	2.37e-25	3.69e-25	6.21e-25	1.51e-24	3.40e-24	8.29e-24	2.94e-23	8.03e-23	2.27e-22
Combined	2.52e-26	2.90e-26	5.00e-26	7.91e-26	1.34e-25	3.03e-25	6.23e-25	1.36e-24	3.96e-24	9.37e-24	2.40e-23

Table 5.13. LAT 4-year limits on $\langle \sigma v \rangle$ at 95% CL for the W^+W^- channel ($\mathrm{cm}^3\ \mathrm{s}^{-1}$).

	81 GeV	100 GeV	250 GeV	500 GeV	1000 GeV	2500 GeV	5000 GeV	10000 GeV
Bootes I	6.82e-25	8.97e-25	2.76e-24	6.78e-24	1.82e-23	7.66e-23	2.46e-22	8.12e-22
Bootes II	–	–	–	–	–	–	–	–
Bootes III	–	–	–	–	–	–	–	–
Canes Venatici I	6.61e-24	8.38e-24	2.56e-23	6.60e-23	1.86e-22	8.17e-22	2.62e-21	9.00e-21
Canes Venatici II	5.43e-24	6.06e-24	1.11e-23	2.27e-23	5.56e-23	2.28e-22	7.71e-22	2.90e-21
Canis Major	–	–	–	–	–	–	–	–
Carina	1.75e-24	1.95e-24	5.77e-24	1.94e-23	6.07e-23	2.89e-22	1.03e-21	4.00e-21
Coma Berenices	1.94e-25	2.38e-25	6.55e-25	1.62e-24	4.43e-24	1.95e-23	6.70e-23	2.52e-22
Draco	2.79e-25	3.44e-25	9.71e-25	2.36e-24	6.11e-24	2.38e-23	7.37e-23	2.53e-22
Fornax	2.25e-24	2.77e-24	7.35e-24	1.70e-23	4.25e-23	1.67e-22	5.30e-22	1.85e-21
Hercules	1.11e-23	1.33e-23	3.17e-23	6.78e-23	1.58e-22	5.36e-22	1.43e-21	4.07e-21
Leo I	6.51e-24	7.50e-24	1.66e-23	3.69e-23	9.47e-23	4.05e-22	1.39e-21	5.29e-21
Leo II	3.73e-24	4.27e-24	1.03e-23	2.53e-23	7.19e-23	3.43e-22	1.25e-21	4.95e-21
Leo IV	1.64e-24	2.02e-24	5.99e-24	1.58e-23	4.64e-23	2.25e-22	8.23e-22	3.27e-21
Leo V	–	–	–	–	–	–	–	–
Pisces II	–	–	–	–	–	–	–	–
Sagittarius	–	–	–	–	–	–	–	–
Sculptor	1.41e-24	1.77e-24	5.02e-24	1.18e-23	2.85e-23	8.91e-23	2.24e-22	6.67e-22
Segue 1	3.99e-25	4.97e-25	1.35e-24	3.08e-24	7.48e-24	2.54e-23	6.21e-23	1.70e-22
Segue 2	–	–	–	–	–	–	–	–
Sextans	1.65e-24	1.78e-24	3.44e-24	7.44e-24	1.91e-23	8.20e-23	2.84e-22	1.09e-21
Ursa Major I	6.53e-25	8.03e-25	2.29e-24	5.85e-24	1.65e-23	7.51e-23	2.62e-22	9.93e-22
Ursa Major II	4.08e-25	4.67e-25	9.39e-25	1.86e-24	4.22e-24	1.54e-23	4.80e-23	1.68e-22
Ursa Minor	1.73e-25	2.18e-25	6.68e-25	1.72e-24	4.76e-24	2.04e-23	6.71e-23	2.40e-22
Willman 1	7.27e-25	8.67e-25	2.11e-24	4.74e-24	1.18e-23	4.44e-23	1.24e-22	3.74e-22
Combined	1.56e-25	1.84e-25	4.12e-25	8.37e-25	1.75e-24	4.52e-24	1.10e-23	3.27e-23

Table 5.14. LAT 4-year limits on $\langle \sigma v \rangle$ at 95% CL for the $t\bar{t}$ channel (cm^3 s^{-1}).

	176 GeV	250 GeV	500 GeV	1000 GeV	2500 GeV	5000 GeV	10000 GeV
Bootes I	1.36e-24	2.10e-24	4.82e-24	1.15e-23	3.98e-23	1.08e-22	3.04e-22
Bootes II	–	–	–	–	–	–	–
Bootes III	–	–	–	–	–	–	–
Canes Venatici I	1.26e-23	1.92e-23	4.47e-23	1.10e-22	3.95e-22	1.10e-21	3.22e-21
Canes Venatici II	9.78e-24	1.19e-23	2.03e-23	4.15e-23	1.29e-22	3.42e-22	9.69e-22
Canis Major	–	–	–	–	–	–	–
Carina	3.19e-24	4.25e-24	1.04e-23	3.18e-23	1.33e-22	3.86e-22	1.15e-21
Coma Berenices	3.67e-25	5.28e-25	1.15e-24	2.72e-24	9.49e-24	2.62e-23	7.61e-23
Draco	5.30e-25	7.75e-25	1.71e-24	4.00e-24	1.33e-23	3.51e-23	9.70e-23
Fornax	4.32e-24	6.15e-24	1.30e-23	2.94e-23	9.62e-23	2.51e-22	6.94e-22
Hercules	2.07e-23	2.87e-23	5.69e-23	1.21e-22	3.64e-22	9.03e-22	2.38e-21
Leo I	1.20e-23	1.56e-23	3.00e-23	6.52e-23	2.15e-22	5.82e-22	1.68e-21
Leo II	6.75e-24	8.93e-24	1.83e-23	4.33e-23	1.57e-22	4.46e-22	1.33e-21
Leo IV	3.12e-24	4.57e-24	1.04e-23	2.60e-23	9.73e-23	2.80e-22	8.44e-22
Leo V	–	–	–	–	–	–	–
Pisces II	–	–	–	–	–	–	–
Sagittarius	–	–	–	–	–	–	–
Sculptor	2.71e-24	4.02e-24	8.83e-24	2.03e-23	6.46e-23	1.62e-22	4.24e-22
Segue 1	7.60e-25	1.11e-24	2.39e-24	5.39e-24	1.72e-23	4.37e-23	1.16e-22
Segue 2	–	–	–	–	–	–	–
Sextans	2.91e-24	3.51e-24	6.22e-24	1.32e-23	4.31e-23	1.17e-22	3.37e-22
Ursa Major I	1.25e-24	1.81e-24	4.02e-24	9.73e-24	3.51e-23	9.86e-23	2.90e-22
Ursa Major II	7.52e-25	9.63e-25	1.72e-24	3.44e-24	1.01e-23	2.54e-23	6.89e-23
Ursa Minor	3.31e-25	5.00e-25	1.16e-24	2.85e-24	1.01e-23	2.74e-23	7.81e-23
Willman 1	1.35e-24	1.86e-24	3.79e-24	8.46e-24	2.76e-23	7.23e-23	1.99e-22
Combined	2.89e-25	3.89e-25	7.44e-25	1.53e-24	4.25e-24	9.44e-24	2.20e-23

5.5 Discussion

We have reported both 2-year γ-ray observations of 10 dwarf spheroidal galaxies and 4-year γ-ray observations of 25 dwarf spheroidal galaxies. No significant γ-ray excess was found coincident with any of the dwarf galaxies in either analysis. We performed combined analyses of 10 dwarf galaxies with 2 years of data and 15 dwarf galaxies with 4 years of data under the assumption that the characteristics of the dark matter particle are shared among the dwarf galaxies. Again, no globally significant excess was found for any of the spectral models tested. We set 95% CL limits on the thermally averaged annihilation cross section for dark matter particle masses in the range from 2 GeV to 10 TeV. These constraints incorporate statistical uncertainties in the J-factors derived from fits to stellar kinematic data. For dark matter particles with masses less than ~ 30 GeV, these studies begin to constrain the annihilation cross section to be less than the thermal relic prediction for s-wave annihilation processes. This is the first time that constraints on the thermal relic annihilation cross section have been robustly set using γ rays.

The analyses presented here greatly improve upon our understanding of the statistical and systematic issues involved in the search for dwarf spheroidal galaxies. Comparing the 2-year and 4-year maximum likelihood analyses, we find that the 4-year constraints are a factor of ~ 2 higher for soft spectral models and a factor of > 2 lower for hard spectral models. These changes can by attributed to updated J-factors, the increased threshold on photon energy, the inclusion of more dwarf spheroidal galaxies (specifically Willman 1), and a statistical reshuffling of events classified as photons when moving from `Pass 6` to `P7REP`. The overlap in events classified as photons by `Pass 6` and `P7REP` is $\sim 70\%$ at energies > 1 GeV [81]. At energies > 10 GeV, this event overlap can drop to 50% in the high-Galactic-latitude ROIs coincident with the dwarf galaxies. Simulations support the naive expectation that on average the 4-year analysis is more sensitive than the 2-year analysis. However, these same simulations show that the magnitude of statistical fluctuations in both the 2-year and the 4-year analyses are comparable to the expected increase in sensitivity.

The 4-year analysis greatly improves our understanding of the potential systematic issues associated with the search for dark matter in dwarf spheroidal galaxies. We find that uncertainties in the LAT instrument performance, the diffuse modeling, and the assumed dark matter individually contribute on the $\lesssim 15\%$ level. This contribution is small compared to the statistical uncertainty both on the LAT photon data and on the J-factor determinations for the dwarfs. Both systematic and statistical uncertainties should decrease with upcoming improvements to the LAT instrument performance (Appendix A), and we expect the combined observations of dwarf spheroidal galaxies to remain one of the most sensitive and robust methods for probing dark matter annihilation throughout the LAT mission.

Chapter 6

Supersymmetric Implications of Dwarf Galaxy Observations†

6.1 Overview

Over the past several decades, supersymmetry (SUSY) has become the most widely-studied, and arguably the best-motivated, theoretical framework for physics beyond the Standard Model (SM) [21]. The most attractive forms of SUSY possess an extra matter parity ("R-parity") that simultaneously explains the stability of the proton and of the Lightest Supersymmetric Particle (LSP). In viable SUSY models, the LSP is often the lightest neutralino, χ, which is one of the most widely studied examples of WIMP dark matter. Generic predictions of SUSY are difficult to obtain, since the minimal consistent SUSY extension of the SM, the Minimal Supersymmetric Standard Model (MSSM), introduces more than 100 free parameters. A typical strategy for overcoming this difficulty is to constrain this set of parameters by employing aesthetic assumptions about the physical origin of SUSY at very high energy (i.e., mSUGRA [139] or CMSSM [140]). In this chapter, we study a broader and more comprehensive subset of the MSSM, the phenomenological-MSSM (pMSSM)

[†] This chapter represents work done with the Fermi-LAT Collaboration and the SLAC Theory Group. It is published as Cotta *et al.* [138]. Special thanks to E. Bloom, R. Cotta, J. Hewett, S. Murgia, and T. Rizzo.

[141]. The pMSSM is derived from the MSSM by using experimental data to eliminate parameters that are free in theory, but highly constrained by observations (e.g., sources of flavor violation in the new physics flavor sector). Thus, the pMSSM provides a compromise between the need to remain flexible and somewhat agnostic in assumptions about yet-undiscovered physics and the need to categorize the range of predictions made by well-motivated theories. The pMSSM model set exhibits a much broader array of phenomenology than can be seen in highly-constrained model sets, whose dark matter phenomenology falls into a few representative classes (i.e., "Focus Point", "Stau Coannihilation", "Bulk Region", and "Higgs Funnel" models). The LSPs of the pMSSM are viable candidates to comprise some or all of dark matter, and they may be probed through a variety of experimental approaches.

In this chapter, we examine the implications of the 2-year LAT combined dwarf limits for the pMSSM. We begin by briefly discussing the techniques employed to generate ~ 71k pMSSM models and the various constraints imposed in their selection. We compare the 2-year LAT cross section limits to the true cross section for each pMSSM model and study the SUSY model dependence in detail. Because the pMSSM models annihilate through a wide range of SM channels, this study provides a much deeper understanding of the theoretical implications of the results in Chapter 5.

6.2 Generation of the pMSSM Model Set

The 19-dimensional parameter space of the pMSSM results from imposing the following minimal set of assumptions on the general R-parity conserving MSSM [142]: (*i*) the soft parameters are taken to be real, allowing no new CP-violating sources beyond those in the CKM matrix; (*ii*) Minimal Flavor Violation [143] is taken to be valid at the TeV scale; (*iii*) the first two generations of sfermions having the same quantum numbers are taken to be degenerate and to have negligible Yukawa couplings; and (*iv*) the LSP is taken to be the lightest neutralino and is assumed to be a stable thermal WIMP. No assumptions are made about physics at high energy scales or the SUSY-breaking mechanisms. Conditions (*i*)–(*iii*) are applied to avoid issues associated with constraints from the flavor sector. These minimal assumptions reduce the

SUSY parameter space to 19 free soft-breaking parameters that are given by three gaugino masses, $M_{1,2,3}$, ten sfermion masses, $m_{\tilde{Q}_1,\tilde{Q}_3,\tilde{u}_1,\tilde{d}_1,\tilde{u}_3,\tilde{d}_3,\tilde{L}_1,\tilde{L}_3,\tilde{e}_1,\tilde{e}_3}$, three A-terms associated with the third generation, $A_{b,t,\tau}$, and the usual Higgs sector parameters μ, M_A and $\tan\beta$.

We selected SUSY models with viable LSPs by numerically scanning the 19-dimensional parameter space of the pMSSM (see Berger *et al.* [141] for more details). Here, we simply note that two scans were performed: the first employed a flat prior on the LSP mass scanning 10^7 points, and the second employed a logarithmic prior on the LSP mass scanning 2×10^6 points. The relevant differences between these two scans were that (*i*) all SUSY mass parameters were restricted to be $\leq 1\,\text{TeV}$ for the flat-prior case, while for the log-prior case this restriction was raised to $\leq 3\,\text{TeV}$, and (*ii*) the choice of the logarithmic prior generally led to more compressed sparticle spectra than did the flat-prior case. The upper mass limit for both scans was chosen to ensure relatively large production cross sections at the LHC. The purpose of our scans was *not* to convey a probabilistic interpretation of the SUSY model space (i.e., it is *not* a Bayesian "posterior distribution"). Instead, we attempted to sample the wide variety of physical characteristics that arises from the phenomenologically-viable pMSSM, and the results that we present are intended to describe the underlying physics governing SUSY dark matter.

After scanning the 19-dimensional parameter space, we subjected the resulting points to the following set of theoretical and experimental constraints.[1] (*i*) Our theoretical constraints required that spectra be tachyon free, that color and charge breaking minima be avoided, and that a bounded Higgs potential exist (leading to radiative electroweak symmetry breaking). (*ii*) We employed experimental constraints from the flavor sector and precision electroweak data arising from the measurements of $(g-2)_\mu$, $b \to s\gamma$, $B \to \tau\nu$, $B_S \to \mu^+\mu^-$, meson–anti-meson mixing, the invisible width of the Z and $\Delta\rho$. (*iii*) We imposed restrictions from numerous direct searches at LEP for both the SUSY particles and the extended SUSY-Higgs sector.[2] (*iv*) We also imposed null results from the set of Tevatron SUSY sparticle and Higgs searches.

---

[1] For full details, see Berger *et al.* [141]

[2] Some of these searches needed to be re-evaluated in detail to remove SUSY model-dependent assumptions [141].

While these bounds have been superseded by LHC analyses, we note that collider searches have been found to be largely uncorrelated with the most important dark matter observables (relic density, annihilation and scattering cross-sections) [144], and we expect the results presented here to accurately represent the prospects for indirect detection in the context of the pMSSM. (v) Finally, we required that the LSP contribution to the dark matter relic density not exceed the 5-year WMAP bound [145] and that the LSP scattering cross sections obey recent constraints from direct detection experiments [141].

After imposing these theoretical and experimental constraints, ∼68.4k models from the flat-prior sample and ∼2.9k models from the log-prior sample remain for study. Because the LSPs of the pMSSM were not required to saturate the relic density, many models allow for multicomponent dark matter. For example, dark matter composed in part by a pMSSM neutralino and in part by an axion that solves the strong CP problem. The distribution of LSP relic density found in our flat- and log-prior model sets are shown in Figure 6.1. We find that a small subset of pMSSM models saturate the WMAP bound (with $\Omega_{\rm LSP}h^2 > 0.1$). We corrected for the fractional abundance of each LSP when calculating the expected γ-ray flux from annihilation (Section 6.4).

6.3 Methods

We calculated γ-ray annihilation spectra for the LSPs of all ∼71k surviving pMSSM models using the computational package DarkSUSY 5.0.5 [146]. We used DarkSUSY to calculate the total γ-ray yield from annihilation, as well as the rates into each of 27 final state channels. We omitted contributions from the loop-suppressed monochromatic channels $\gamma\gamma$ and γZ^0 which, although distinctive, are typically tiny in our model set. These γ-ray spectra were tested for consistency with 2 years of LAT γ-ray data associated with the 10 dwarf spheroidal galaxies in Table 5.2.

We followed the procedure presented in Section 5.3 to constrain the γ-ray signal from 10 dwarf spheroidal galaxies with a joint likelihood analysis of the LAT data. Our data sample and event selection were identical to those described in Section 5.3.1,

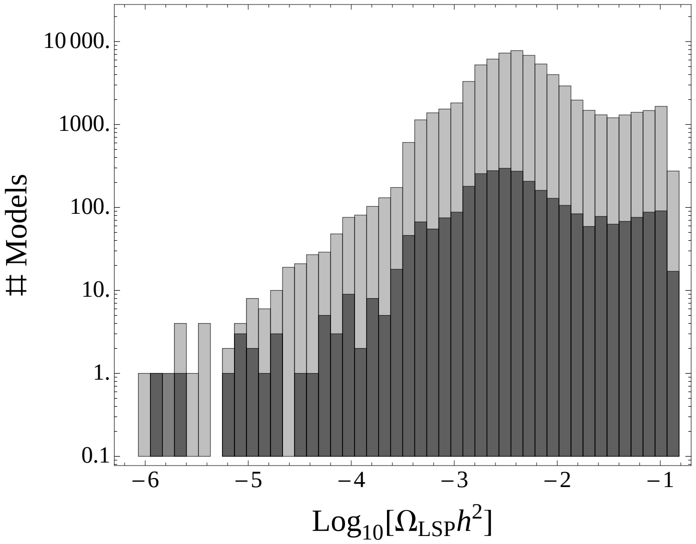

Figure 6.1 Logarithm of the LSP relic density, $\Omega_{\mathrm{LSP}}h^2$, for the flat-prior selected pMSSM models (gray bars) and log-prior selected pMSSM models (black bars).

and our analysis was similar to that described in Section 5.3.3. J-factors and associated statistical uncertainties for the 10 dwarf galaxies were taken from Table 5.2, where they were calculated using line-of-sight stellar velocities and the Jeans equation. Our procedure for constraining the total annihilation cross section differed from that described in Section 5.3.3 in that we modeled the γ-ray emission from the dwarf galaxies with spectra generated from the ~ 71k pMSSM models rather than prototypical annihilation channels (i.e., $b\bar{b}$, $\tau^+\tau^-$, $\mu^+\mu^-$, and W^+W^-). We calculated a joint likelihood for each pMSSM model by tying the pMSSM model parameters across the regions of interest (ROIs) surrounding the 10 dwarf spheroidals using Equation (5.4). We found no significant γ-ray signal from any of the dwarf galaxies when analyzed individually or jointly for any of the pMSSM models. For each of the ~ 71k pMSSM models, we calculated the maximum annihilation cross section, $\langle\sigma v\rangle_{\mathrm{max}}$, consistent with the null detection in the LAT data using the delta-log-likelihood technique [92].

6.4 Results

6.4.1 Model Constraints

We calculated the “boost” factor, $\mathcal{B}$, as the ratio between the cross section upper limit, $\langle\sigma v\rangle_{\rm max}$, and the thermal cross section, $\langle\sigma v\rangle_{\rm T}$, predicted for the model

$$\mathcal{B} \equiv \langle\sigma v\rangle_{\rm max}/\langle\sigma v\rangle_{\rm T} \ . \tag{6.1}$$

The boost represents the multiplicative factor that must be applied either to the J-factor or to the cross section in order for the predicted γ-ray flux to exceed the LAT sensitivity. Here, $\langle\sigma v\rangle_{\rm T} \equiv \langle\sigma v\rangle R^2$ represents the annihilation cross section rescaled by the fraction of dark matter for which the particular LSP is responsible,

$$R \equiv \frac{\Omega_{\rm LSP}}{\Omega_{\rm WMAP}} \tag{6.2}$$

where $\Omega_{\rm WMAP}h^2 = 0.1143$ [145]. When expressing the predicted γ-ray flux from dark matter annihilation, R is often assumed to be unity (Equation (2.6)). Thus, we identify pMSSM models with LSPs that nearly saturate the WMAP relic density, $\Omega_{\rm LSP}h^2 > 0.10$ ($R > 0.875$), and investigate this subset of models in more detail below. Deviations from the scaling in Equation (6.2) are appropriate for models where non-standard cosmology or other non-standard mechanisms sever the relationship between the relic density and the present-day annihilation cross section.

The boost factor, $\mathcal{B}$, was calculated for each pMSSM model and is displayed in Figure 6.2. Models with $\mathcal{B} \leq 1$ would be excluded at $\geq 95\%$ confidence, while models with $\mathcal{B} > 1$ evade this limit by a factor of $\mathcal{B}$. None of the pMSSM models were excluded at 95% confidence by this analysis; however, values of $\mathcal{B}$ reach $\sim$1.5 for many of the models with LSP masses $\sim 40\,$GeV, relic densities that nearly saturating the WMAP measurement ($R > 0.875$), and annihilations predominantly to $\tau^+\tau^-$ (as is further discussed in Section 6.4.2).

In Figure 6.2 we observe, as expected, that the relic density of a given pMSSM model is important in determining the γ-ray signal strength. Despite this, we see

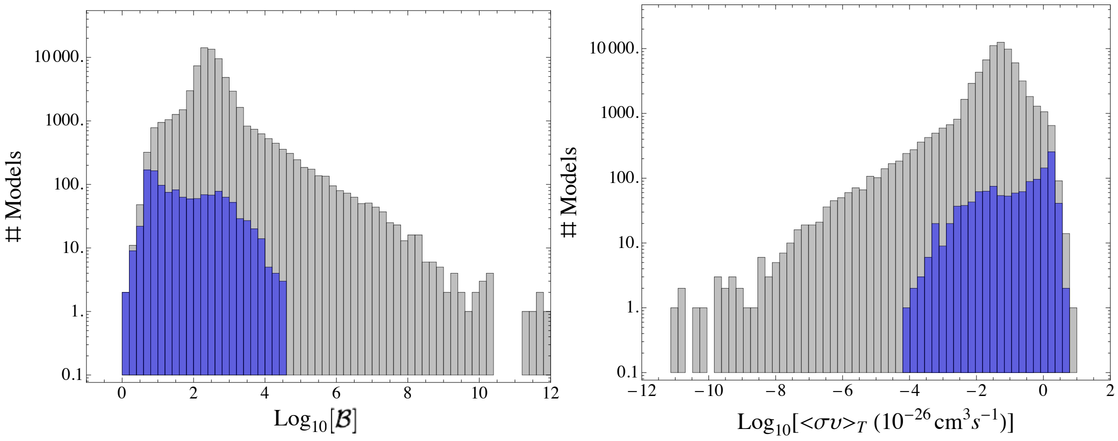

Figure 6.2 Boost factor, $\mathcal{B}$, for all flat-prior selected pMSSM models (gray bars) and flat-prior models with $R > 0.875$ (blue bars). We similarly histogram $\langle\sigma v\rangle_{\mathrm{T}}$ and note that the $\mathcal{B}$ distribution is largely driven by the $\langle\sigma v\rangle_{\mathrm{T}}$ distribution.

that the range of predictions in either subset of models is quite large, spanning many orders of magnitude. We note the surprising fact that, among models with $\mathcal{B} < 10$, nearly 40% do not saturate the WMAP bound.

We find that the shape of the $\mathcal{B}$ distribution is largely determined by the shape of the $\langle\sigma v\rangle_{\mathrm{T}}$ distribution, and one can verify that the difference in $\mathcal{B}$ distributions between flat- and log-prior cases is echoed in their $\langle\sigma v\rangle_{\mathrm{T}}$ distributions. Models with such large $\mathcal{B}$ values are seen to be special cases, involving a finely tuned relationship between the LSP mass and the mass of one or more of the SUSY Higgs states (so-called "Higgs Funnel" models with $m_\chi \sim m_h/2$), that annihilate so efficiently in the early universe as to have minuscule relic density.

6.4.2 SUSY Model Dependence

In discussing the SUSY model dependence of these results, we first note that most of the span in $\mathcal{B}$ arises from the wide ranging values of the quantity $\langle\sigma v\rangle_{\mathrm{T}}/m_\chi^2$ and that for a given value of $\langle\sigma v\rangle_{\mathrm{T}}/m_\chi^2$ there is only about an order of magnitude span in $\mathcal{B}$ (Figure 6.3). To understand this dependence we return to Equation (2.6) (replicated here with $\langle\sigma v\rangle_{\rm T}$ and m_χ inserted appropriately)

$$\phi_\gamma(\Delta\Omega) = \int_{\Delta\Omega}\Big\{\int_{\rm l.o.s.}\rho^2(\vec{r})dl\Big\}d\Omega'\cdot\frac{1}{4\pi}\frac{\langle\sigma v\rangle_{\rm T}}{2m_\chi^2}\int_{E_{\rm min}}^{E_{\rm max}}\frac{dN_\gamma}{dE_\gamma}dE_\gamma. \tag{6.3}$$

We focus now on the particle physics-dependent piece, which is proportional to $\langle\sigma v\rangle_{\rm T}/m_\chi^2$ and the integral over the total γ-ray continuum yield curve,

$$\frac{dN_\gamma}{dE_\gamma} = \sum_i B_i\Big\{\frac{dN_{\gamma,i}^{\rm SEC}}{dE_\gamma}+\frac{dN_{\gamma,i}^{\rm FSR}}{dE_\gamma}+\frac{dN_{\gamma,i}^{\rm VIB}}{dE_\gamma}\Big\}. \tag{6.4}$$

Here, the sum is over annihilation final-state channels with terms describing the γ-ray yield from secondary hadronization (SEC), final-state radiation (FSR), and virtual internal bremsstrahlung (VIB).[3] As previously noted, monochromatic γ-ray contributions are negligible here. The previous results shows that the value of $\mathcal{B}$ is predominantly determined by the total thermally-averaged annihilation cross section, the relic density (implicit in $\langle\sigma v\rangle_{\rm T}$), the LSP mass, and to a much lesser extent by the shape of the γ-ray spectrum.

We next discuss the SUSY model dependence of the spectral shape of the annihilation signal. It is useful to remove the large prefactor, $\langle\sigma v\rangle_{\rm T}/m_\chi^2$, and focus instead on the quantity,

$$\phi_s\times(m_\chi^2/\langle\sigma v\rangle_{\rm T})\propto\int_{E_{\rm min}}^{E_{\rm max}}\frac{dN_\gamma}{dE_\gamma}dE_\gamma\,. \tag{6.5}$$

Here, we integrate the total continuum yield curve over the experimental energy range from $E_{\rm min} = 200\,{\rm MeV}$ to $E_{\rm max} = 100\,{\rm GeV}$. In translating to $\phi_s\times(m_\chi^2/\langle\sigma v\rangle_{\rm T})$, we have removed the explicit dependence on the total annihilation rate $\langle\sigma v\rangle_{\rm T}$ and most of the dependence on the LSP mass. What remains is a quantity that depends on the relative annihilation rates into SM final state channels, which is useful for comparing models with similar $\langle\sigma v\rangle_{\rm T}$ and LSP mass. A small residual LSP mass dependence remains in $\phi_s\times(m_\chi^2/\langle\sigma v\rangle_{\rm T})$, via the relationship between the LSP mass and the limits of integration in Equation (6.5).

---

[3] We use the language of [147] in discriminating FSR and VIB, although it has been pointed out that such a distinction is somewhat artificial (and not even gauge invariant) [148].

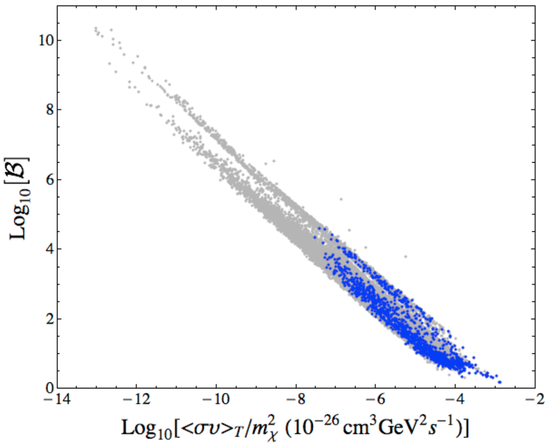

Figure 6.3 Flat-prior pMSSM models represented in the $\mathcal{B}$ vs. $\langle\sigma v\rangle_{\mathrm{T}}/m_\chi^2$ plane. Gray points represent generic models in this set while the subset of models with $R > 0.875$ are highlighted in blue. One observes that the wide range of $\mathcal{B}$ values corresponds directly to the wide range of $\langle\sigma v\rangle_{\mathrm{T}}/m_\chi^2$ values in our model set, and that at a given value of $\langle\sigma v\rangle_{\mathrm{T}}/m_\chi^2$ there is about an order of magnitude span in $\mathcal{B}$ values. It can also be noted that $\sim 40\%$ of models with $\mathcal{B} < 10$ have $R < 0.875$.

The supersymmetric origin of our γ-ray spectra is reflected in the distribution of annihilations into distinct SM final states (f). In SUSY, due to the Majorana nature of the annihilating LSPs and the fact that LSPs are non-relativistic in current dark matter halos, the annihilation rates for processes such as $\chi\chi \to f\bar{f}$ are proportional to $(m_f/m_\chi)^2$, a fact that is often referred to as helicity suppression [149]. The ratio of rates into distinct channels (say $f\bar{f}$ and $f'\bar{f}'$) is thus $\propto (m_f/m_{f'})^2$ so that annihilation rates into channels with heavy final-state SM particles often dominate those with lighter final-state SM particles. These ratios are complicated by the fact that the rates $\chi\chi \to f\bar{f}$ are coherent sums of subprocesses with varying couplings, mixing angles, and exchanged particle masses. In our pMSSM model set, we see a small set of models that rebel against the expectations from highly-constrained SUSY frameworks (e.g., pMSSM models that annihilate to $\mu^+\mu^-$ via a light $\tilde{\mu}$); however, the dominant annihilation final states for most models are in accord with the helicity suppression intuition. For the vast majority of models in our set, annihilations are predominantly composed of a kinematically viable ($m_\chi > m_f$) mixture of the $b\bar{b}$, $\tau^+\tau^-$, W^+W^-,

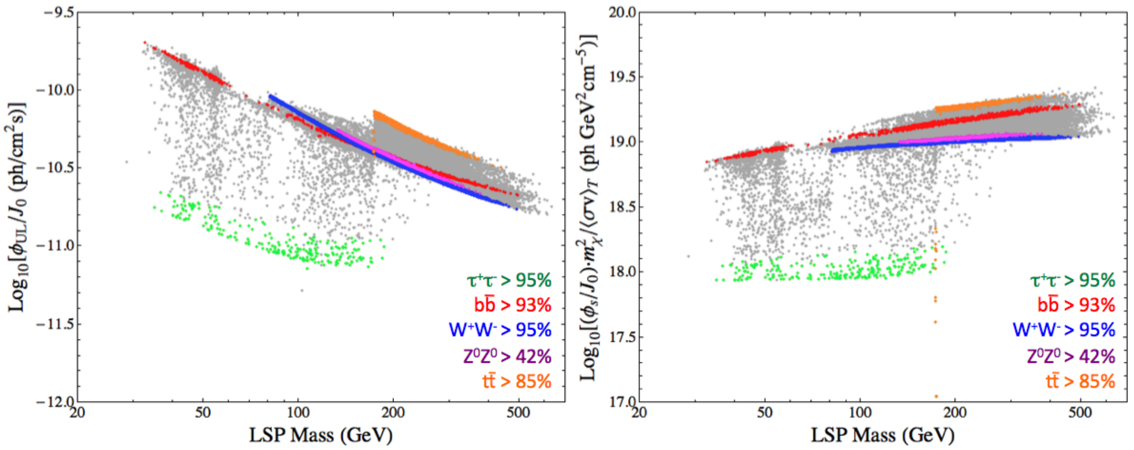

Figure 6.4 Flat-prior pMSSM models in the LAT flux upper limit vs. LSP mass (left panel) and scaled signal flux vs. LSP mass (right panel) planes (taking $J_0 = 10^{19}\,\mathrm{GeV}^2\,\mathrm{cm}^{-5}$ as a reference J-factor). The full flat-prior model set is displayed as gray points and models whose annihilations occur predominantly through a given final state channel are overlaid in other colors. Models with $\langle \sigma v\rangle_{\tau\bar{\tau}}/\langle \sigma v\rangle > 0.95$ (green), with $\langle \sigma v\rangle_{b\bar{b}}/\langle \sigma v\rangle > 0.93$ (red), with $\langle \sigma v\rangle_{W^+W^-}/\langle \sigma v\rangle > 0.95$ (blue), with $\langle \sigma v\rangle_{Z^0Z^0}/\langle \sigma v\rangle > 0.42$ (magenta) and with $\langle \sigma v\rangle_{t\bar{t}}/\langle \sigma v\rangle > 0.85$ (orange) are shown. Purities are chosen to obtain model subsets of similar size.

Z^0Z^0, and $t\bar{t}$ channels. We observe a number of cases where the loop-level annihilation to gluons, $\chi\chi \to gg$, is dominant[4] and a small number of cases where there are sizable (but still sub-dominant) contributions from the hA^0, HA^0, hZ^0, HZ^0, $W^{\pm}H^{\mp}$, and (monochromatic) $\gamma\gamma$ or γZ^0 channels.

The ability of the LAT to constrain a given pMSSM model can be decomposed into two planes (displayed in Figure 6.4). The ϕ_{UL} (LAT flux upper limit) vs. LSP mass plane demonstrates the ability of the LAT to constrain the spectral shapes of various annihilation channels, while the $\phi_s \times (m_\chi^2/\langle \sigma v\rangle_{\mathrm{T}})$ vs. LSP mass plane describes the (scaled) signal flux expected from each channel. We see that subsets of models with nearly pure annihilation final state channels cluster tightly in both planes and,

---

[4] Loop-level annihilation to gluons can occur when the LSP co-annihilates with light flavored sfermions (e.g., $\tilde{u}$, $\tilde{d}$, $\tilde{e}$, $\tilde{\nu}$, etc..) in the early universe. In current dark matter halos, annihilation by exchange of the lightest sfermions is heavily helicity suppressed ($\sim m_f^2/m_\chi^2$) so that the loop-level process $\chi\chi \to gg$ may become the most efficient annihilation channel today.

with the exception of the dominantly Z^0Z^0 channel models,[5] extend down to their kinematic endpoints.[6]

The left panel of Figure 6.4 confirms that the LAT search is more sensitive to harder γ-ray spectra, as expected since astrophysical backgrounds fall rapidly with energy. In particular, we see that LAT constraints on spectra from nearly pure $\chi\chi \to \tau^+\tau^-$ annihilations are tighter, by about an order of magnitude, than those placed on nearly pure $\chi\chi \to b\bar{b}$ annihilations. One expects the relative shapes of these two "curves" to change as LAT data taking continues. The LAT sensitivity to hard spectra, which contribute a significant number of photons in the background-free regime ($\gtrsim 10\,\mathrm{GeV}$), is expected to increase more quickly than the sensitivity to softer spectra, which contribute in the background-dominated regime. Thus, the gap between limits on $\chi\chi \to \tau^+\tau^-$ and $\chi\chi \to b\bar{b}$ in the left panel of Figure 6.4 is expected to widen.

We note from the right panel of Figure 6.4 that nearly pure annihilations to $\tau^+\tau^-$ yield about an order of magnitude *fewer* signal photons than models with nearly pure annihilations to $b\bar{b}$, at the same LSP mass and $\langle\sigma v\rangle_{\mathrm{T}}$. This finding was discussed at length in Cotta *et al.* [150], where it was noted that, although the γ-ray spectra resulting from τ-like annihilations are harder (due to a large contribution from prompt π^0 decay), they are also flatter at low energies. This is demonstrated in Figure 6.5, where we display spectra (as calculated by DarkSUSY 5.0.4) for models that annihilate nearly purely into the $b\bar{b}$ and $\tau^+\tau^-$ final-state channels. The curves displayed here correspond to the integrand in Equation (6.5) and, when plotted in terms of the variable $x \equiv E_\gamma/m_\chi$, have a nearly universal shape (there is significant SUSY model

---

[5] While the subset of models with $(\langle\sigma v\rangle_{ZZ}/\langle\sigma v\rangle) > 0.42$ do not extend down to $m_\chi \approx m_Z$, the subset of models with $(\langle\sigma v\rangle_{ZZ}/\langle\sigma v\rangle) > 0.20$ do extend to this kinematic endpoint. T he highest purity for $\chi\chi \to Z^0Z^0$ annihilations in our model set is $(\langle\sigma v\rangle_{ZZ}/\langle\sigma v\rangle) \approx 0.45$, such models also annihilate to $\chi\chi \to W^+W^-$ with $(\langle\sigma v\rangle_{WW}/\langle\sigma v\rangle) \approx 0.55$.

[6] The set of $\mathcal{O}(10)$ orange points near the top threshold, $m_\chi \approx m_t$, are models that annihilate dominantly through the $\chi\chi \to t\bar{t}$ channel. They have very bino-like LSPs (suppressing many other channels) and currently annihilate dominantly through stop exchange. These models satisfy the WMAP relic abundance constraint either by co-annihilation with a light stop or via the exchange of very light sfermions (i.e., channels that were more efficient at freeze-out). Since they are forced to annihilate dominantly to $t\bar{t}$ with $m_\chi \approx m_t$, they are phase-space suppressed, $\langle\sigma v\rangle_{t\bar{t}} \propto (1 - m_t^2/m_\chi^2)^{1/2}$, and their fluxes are much lower than typical models that annihilate through this channel.

dependence at $E_\gamma \approx m_\chi$, due to internal bremsstrahlung [147]). Comparing the $b\bar{b}$ and $\tau^+\tau^-$ cases it is clear that, at a given LSP mass and $\langle\sigma v\rangle_{\mathrm{T}}$, the softer $b\bar{b}$ spectra will produce a much larger integrated flux of signal γ rays than the $\tau^+\tau^-$ spectra. We also observe that the vast majority of signal γ rays have energy $E_\gamma \ll m_\chi$, regardless of the particular final-state channel, so that the integrated signal flux depends sensitively on the lower limit of integration $x_{\min} \equiv E_{\min}/m_\chi$. Heavier LSPs allow integration to lower x values and thus a wider gap between the total flux from $b\bar{b}$ and $\tau^+\tau^-$ annihilations. This is reflected in the relative slope of the red and green "lines" in the right panel of Figure 6.4.

The two panels of Figure 6.4 describe two important factors in determining $\mathcal{B} \equiv \langle\sigma v\rangle_{\max}/\langle\sigma v\rangle_{\mathrm{T}} \equiv \phi_{\mathrm{UL}}/\phi_s$: (*i*) the ability to tightly constrain the flux from a given spectral shape (ϕ_{UL}) and (*ii*) the γ-ray flux expected from that particular spectral shape (ϕ_s). These pieces of information must be combined to determine the sensitivity of the LAT to a given final state channel, at fixed LSP mass and $\langle\sigma v\rangle_{\mathrm{T}}$.

In the left panels of Figure 6.6 we display points for our models in the $\mathcal{B} \times \langle\sigma v\rangle_{\mathrm{T}}/m_\chi^2$ vs. LSP mass plane, with models that annihilate largely into single final state channels colored as in Figure 6.4. Using $\mathcal{B} \times \langle\sigma v\rangle_{\mathrm{T}}/m_\chi^2$ is equivalent to using $\phi_{\mathrm{UL}}/(\phi_s \times (m_\chi^2/\langle\sigma v\rangle_{\mathrm{T}}))$, a ratio of the values found in the panels of Figure 6.4. We see that annihilations to a given final state are organized nicely in this plane. For comparison, in the right panels of Figure 6.6 we display points for each of our flat-prior models in the $\mathcal{B}$ vs. LSP mass plane using the same color scheme, where the colored points are seen to be highly mixed. Figure 6.6 allows us to predict whether it is easier to constrain annihilations to $\tau^+\tau^-$ or to $b\bar{b}$ (for example), at a given LSP mass, $\langle\sigma v\rangle_{\mathrm{T}}$, and with experimental thresholds $E_{\min}$ and $E_{\max}$. From the left panels we observe that annihilations to $\tau^+\tau^-$ are more difficult to constrain than annihilations to $b\bar{b}$ for LSP masses $m_\chi \gtrsim 50\,\mathrm{GeV}$, while the opposite is true for lighter LSPs. This crossover at $m_\chi \approx 50\,\mathrm{GeV}$ is the point at which there is a balance between the hard spectrum and the low photon flux from $\tau^+\tau^-$ annihilations. We expect this crossover to move toward higher masses as more LAT data is collected since the sensitivity to harder spectra is expected to increase more quickly than the sensitivity to softer spectra.

We emphasize that the gray points in the left panels of Figure 6.6 are as important

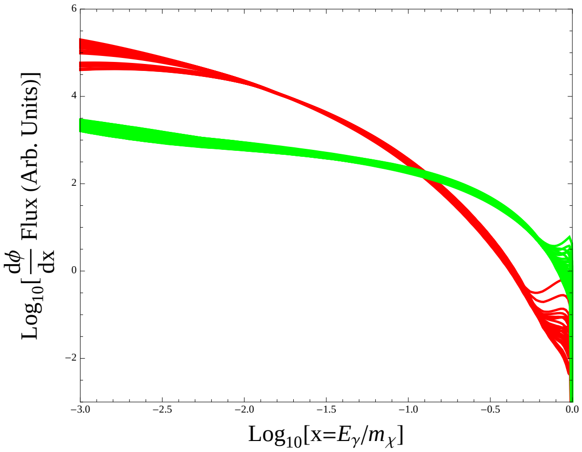

Figure 6.5 Gamma-ray spectra for the pMSSM models that annihilate into $b\bar{b}$ (red) and $\tau^+\tau^-$ (green) final states with purities as in Figure 6.4. Spectra have been scaled to remove the $\langle\sigma v\rangle_{\mathrm{T}}/m_\chi^2$ prefactor and plotted in terms of the variable $x = E_\gamma/m_\chi$ to emphasize the universality of the final state spectra.

as the colored bands. The regions filled by gray points represent the combination of annihilation final-state channels realized in the pMSSM model set and provide an estimate for the deviation from the special case of pure annihilations. For example, we observe that there is a special group of ~ 50 models with masses $m_\chi \approx 100\,\mathrm{GeV}$ that are constrained more tightly than the models annihilating purely to $b\bar{b}$, i.e., the points falling below the red "line" in the top left panel of Figure 6.6. These are models that have a significant enhancement of the γ-ray spectrum near the kinematic endpoint $x = E_\gamma/m_\chi \approx 1$. This enhancement is due to internal bremsstrahlung production a γ ray directly from the hard process $\chi\chi \to f\bar{f}\gamma$, in addition to radiation off of the final state particles created from the process $\chi\chi \to f\bar{f}$ [147, 151]. The cross section for the $2 \to 3$ process is naively much smaller than that for the $2 \to 2$ process as the $2 \to 3$ case is suppressed by a factor of the fine structure constant and by three-body phase space. However, the leading terms in the $2 \to 2$ process are helicity suppressed by a factor of $\sim (m_f/m_\chi)^2$ relative to the naive expectation, so that the $2 \to 3$ process, $\chi\chi \to f\bar{f}\gamma$, can be competitive with (or even dominate) the process $\chi\chi \to f\bar{f}$. This is especially true for annihilations to light final state particles, $(m_f/m_\chi) \ll 1$, through light superpartner mediators, $\tilde{f}$, such that $(m_{\tilde{f}}/m_\chi) \approx 1$. Here, we find that many

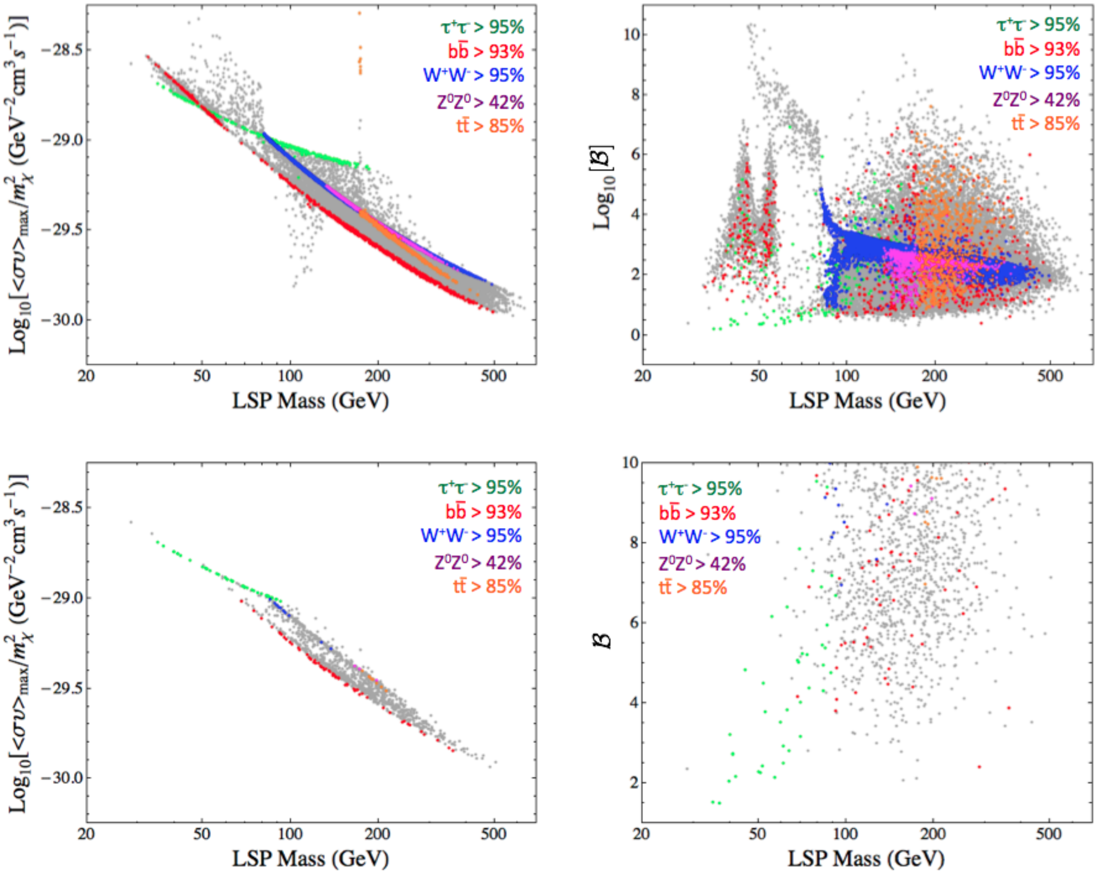

Figure 6.6 The distributions of the pMSSM models in the $\langle\sigma v\rangle_{\max}/m_\chi^2$ vs. LSP mass plane (left panels) and $\mathcal{B}$ vs. LSP mass plane (right panels). The full flat-prior model set is displayed as gray points and models whose annihilations occur predominantly through a given final state channel are overlaid in other colors, as denoted in the figure. In the left panels, one can see that removing the dependence on total annihilation rate and LSP mass (scaling $\mathcal{B}\times\langle\sigma v\rangle_{\mathrm{T}}/m_\chi^2 = \langle\sigma v\rangle_{\max}/m_\chi^2$) allows for tight localization of models with similar annihilation spectra, whereas it is comparatively difficult to predict where models fall in the $\mathcal{B}$ vs. LSP mass plane without such scaling. The upper panels display these relations for all pMSSM models while the lower panels focus on those models that are closest to constraint ($\mathcal{B} < 10$).

models in this group have SUSY mass spectra with very light sleptons, $m_{\tilde{e}} \approx m_\chi$ so that the would-be dominant annihilation channel $\chi\chi \rightarrow e^+e^-$ is heavily suppressed and the $2 \rightarrow 3$ channel $\chi\chi \rightarrow e^+e^-\gamma$ contributes heavily to the overall γ-ray spectrum.

6.4.3 Comparison to Direct Detection

It is expected that collider searches, direct detection experiments, and indirect-detection experiments will provide highly complementary information about the nature of dark matter. The set of pMSSM models discussed in this work has already been studied in the context of LHC searches [152, 153] and direct detection experiments [154]. We note that, essentially by construction, LHC searches are expected to rapidly exclude (or discover) most of the models in this set. Thus, a comparison of LAT and LHC results would be relatively unenlightening, since the most constraining LHC searches are typically only indirectly related to the detailed nature of the LSP. Therefore, we focus on a comparison between the prospects for future LAT dwarf analyses and the limits on spin-independent and spin-dependent scattering cross sections.

Since the LAT is presently very close to constraining part of the pMSSM parameter space, it is useful to estimate how constraints may improve over a 10 year mission lifetime. In the low-energy, background dominated regime, the LAT point source sensitivity increases as roughly the square-root of the integration time. However, in the high-energy, limited background regime (where many pMSSM models contribute), the LAT sensitivity increases more linearly with integration time. Thus, 10 years of data could provide a factor of $\sqrt{5}$ to 5 increase in sensitivity. Additionally, optical surveys such as Pan-STARRS [155] and the Dark Energy Survey [156] could discover a factor of 3 more dwarf spheroidal satellite galaxies [77], which would correspond to a sensitivity increase of $\sqrt{3}$ to 3. Ongoing improvements in LAT event reconstruction, a better understanding of background contamination, and an increased energy range are all expected to provide additional increases in the LAT sensitivity (see Appendix A). Thus, we find it plausible that the LAT constraints could improve by a factor of 10 compared to current constraints. Additionally, simulations predict that dark matter substructure within the dwarf spheroidals may increase their J-factors by factors of 2 to 10 [103, 157]. Such a boost would improve the current cross section sensitivity by a comparable factor. Thus, we choose to examine pMSSM models with $\mathcal{B} < 10$ in detail.

Direct detection experiments generally have an easier time setting limits on LSPs with low relic density since their sensitivity scales as ρ rather than ρ^2. In Figure 6.7, we display the set of pMSSM models in the spin-independent (left panel) and spin-dependent (right panel) scattering cross section vs. LSP mass planes, highlighting the models within reach of future LAT dwarf analyses (i.e., models with $\mathcal{B} < 10$). We note that spin-independent scattering bounds have become significantly more constraining since the era when the pMSSM models were generated. The current best bound has been set by the XENON100 Collaboration [158] and is depicted by the black curve on the left panel of Figure 6.7. An uncertainty of about a factor of four applies to this curve, due to uncertainty in the determination of matrix elements for nuclear scattering.

We observe that there are many models that both direct and indirect detection experiments are expected to be sensitive to. This is a fortunate scenario, potentially allowing us to infer relationships between the LSP mass, cross section, annihilation final state channels, and details about heavier SUSY particles. Additionally, we observe that there exist a number of models that will only be accessible to the LAT. These are models whose LSPs are dominantly bino and whose particle spectrum is somewhat hierarchical, including the light bino and one or more light sleptons. Such a scenario is essentially invisible in both direct detection experiments and at the LHC, due to a lack of accessible colored production channels.

6.5 Discussion

We have investigated the ability of the LAT instrument to detect a large set of phenomenologically-viable supersymmetric dark matter candidates. While the behavior of many of the pMSSM models in our set is consistent with the intuition developed from highly constrained SUSY scans, we find that some pMSSM models possess vastly

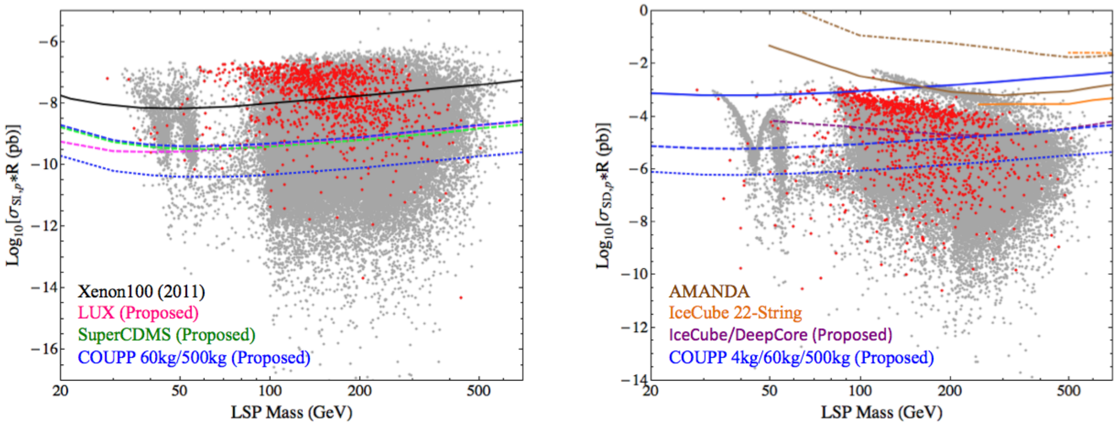

Figure 6.7 Comparison of the future sensitivities of LAT dwarf galaxy searches and direct detection experiments. We display all points in the flat-prior model set in gray and points having $\mathcal{B} < 10$ in red. In the left panel the black curve depicts the current best spin-independent scattering limit set by XENON100 [158]. Projected spin-independent sensitivities from LUX [159], SuperCDMS [160], COUPP 60kg and COUPP 500kg [161] are displayed as, magenta-dashed, green-dashed, blue-dashed and blue-dotted lines, respectively. In the right panel, current spin-dependent scattering limits from the AMANDA [162] and IceCube-22 [163] collaborations are displayed as brown and orange lines, respectively (with the assumption of soft or hard channel annihilations represented by dash-dotted or solid lines, respectively). Near-future projected sensitivities from the COUPP [164][161] 4kg, 60kg, and 500kg searches in blue- solid, dashed, and dotted lines, respectively. The projected IceCube/DeepCore sensitivity estimated in [165] is displayed as a magenta-dashed line (a more accurate IceCube/DeepCore analysis is presented in [144]).

different SUSY model-dependence. In particular, we have loosened the assumption of single-component dark matter composed entirely out of the lightest neutralino and have demonstrated that the LAT may still be sensitive to some of these models. Many models have unique annihilation channels and rates that are only observed in the broader context of the pMSSM and cannot be separated into just a few classes, as is expected in mSUGRA/CMSSM dark matter scenarios. We have investigated the ability of the LAT to constrain annihilations into various final-state channels, noting that the LAT analysis is most sensitive to light LSPs ($m_\chi < 50\,\mathrm{GeV}$) annihilating dominantly to $\tau^+\tau^-$ and heavier LSPs annihilating dominantly to $b\bar{b}$. Such behavior reflects a trade-off between the relative ease of constraining the spectral shape of annihilations to $\tau^+\tau^-$ with the relatively low number of γ rays produced as a result of these annihilations. The crossover point in sensitivity is expected to move toward higher LSP masses as the LAT continues to take data.

We have compared future expectations of the LAT dwarf search with those for direct detection experiments, finding examples of models that are accessible to combinations of the two experimental techniques. Indirect searches are invaluable due to their sensitivity to dark matter signals regardless of the SM states that the dark matter couples to most strongly (rather than requiring a strong coupling to quarks and gluons as in direct detection experiments and, to a large extent, colliders). Additionally, the indirect detection of dark matter would provide information about the cosmological dark matter abundance, rather than having to infer dark matter properties from neutral detector-stable particles produced at colliders.

Chapter 7

Unassociated Galactic Dark Matter Substructure[†]

7.1 Overview

Cosmological N-body simulations predict that the Milky Way should possess many more bound dark matter subhalos than are optically observed as satellite dwarf galaxies [12, 13]. This prediction allows for the possibility that the majority of these subhalos are composed solely of dark matter. While simulations have the resolution to recover all subhalos down to a mass of $\sim 10^6\,M_\odot$, the minimum mass of a bound subhalo orbiting the Milky Way may be as low as that of the Earth ($\sim 10^{-6}\,M_\odot$), a scale roughly set by the dark matter velocity at freeze-out [167, 168]. Massive dark matter subhalos located in the outer regions of the Galactic halo or lower mass subhalos located near to Earth may constitute spatially extended γ-ray sources that could be detected with the LAT. It has been suggested that a significant γ-ray flux from dark matter annihilation could arise from these dark matter subhalos within the Milky Way halo [108, 157, 169–173].

[†] This chapter represents work done with the Fermi-LAT Collaboration and is published as Ackermann *et al.* [166]. Special thanks to E. Bloom, S. Digel, R. Johnson, J. Knödlseder, J. Lande, L. Strigari, P. Wang, and S. Zalewski.

In this chapter, we report a search for dark matter subhalos among the unassociated γ-ray sources detected in one year of LAT data. We begin by examining the theoretical motivation for such a search. Then, we describe how unassociated, high-Galactic-latitude γ-ray sources were selected from both the First LAT Source Catalog (1FGL) [174] and an independent list of source candidates created with looser assumptions on the source spectrum. We discuss the likelihood ratio tests designed to distinguish dark matter subhalos from conventional astrophysical sources. No dark matter subhalo candidates were found in either the unassociated 1FGL sources or the additional list of candidate sources. Finally, the Aquarius [13] and Via Lactea II [12] simulations were used to derive upper limits on the annihilation cross section for a 100 GeV dark matter annihilating through the $b\bar{b}$ channel.

7.2 Dark Matter Subhalos

In this section, we discuss the use of ΛCDM simulations to derive models of the spatial and mass distributions of Galactic dark matter subhalos. We motivate the search for dark matter subhalos lacking optical counterparts by predicting the number of subhalos that are detectable, given the constraints on dark matter annihilation from dwarf spheroidal galaxies. We discuss how extrapolating the mass function of dark matter subhalos below the mass resolution of current numerical simulations impacts the LAT detection potential.

7.2.1 Numerical Simulations

The Aquarius [13] and Via Lactea II (VL-II) [12] projects are high resolution numerical simulations of dark matter substructure at the scale of Galactic halos. As part of the Aquarius project, six independent simulations of a Milky Way-mass dark matter halo were generated. The VL-II project provides an additional, independent simulation. These simulations model the formation and evolution of Milky Way-sized dark matter halos and their subhalos, possessing over one billion $\sim 10^3\,M_\odot$ particles. Each simulation resolves over 50,000 subhalos within its respective virial radius, which is defined as the radius enclosing an average density 200 times the cosmological mean matter density. Each bound subhalo has associated with it a position with respect to the main halo, a velocity, a tidal mass, $M_{\rm tidal}$, a maximum circular velocity, $V_{\rm max}$, and a radius of maximum circular velocity, $R_{V_{\rm max}}$.

The γ-ray flux from annihilating dark matter is generically described by Equation (2.6). However, for a localized dark matter distribution at a distance, D, that is large compared to the scale radius of the distribution, the integrated J-factor can be approximated as [175]

$$\begin{aligned} J &\equiv \int_{\Delta\Omega} \Big\{ \int_{\rm l.o.s.} \rho^2(\boldsymbol{r}) dl \Big\} d\Omega \\ &\approx \frac{1}{D^2} \int_V \rho^2(\boldsymbol{r}) dV \ . \end{aligned} \tag{7.1}$$

Here, the volume integration is performed out to the tidal radius of the dark matter distribution. This approximation proves useful when calculating J-factors for simulated Galactic subhalos since evaluating $\mathcal{O}(10^5)$ line-of-sight integrals is computationally intensive.

For the present analysis, the internal dark matter distribution of the subhalos was modeled by an NFW profile with scale radius, $r_{\rm s}$, and density normalization, ρ_0 (Equation (2.1)) [52]. The profile parameters of each simulated subhalo were uniquely assigned using the relations of Kuhlen *et al.* [56],

$$r_{\rm s} = \frac{R_{V_{\rm max}}}{2.163} \tag{7.2}$$

$$\rho_0 = \frac{4.625}{4\pi G} \left(\frac{V_{\rm max}}{r_{\rm s}} \right)^2 , \tag{7.3}$$

where $r_{\rm s}$ is in kpc and ρ_0 is in $M_\odot\,{\rm kpc}^{-3}$. The J-factors calculated by assuming an NFW profile account only for the annihilation flux from the smooth component of the dark matter distribution in each subhalo. The existence of dark matter substructure within the subhalos themselves would increase the J-factor; however, this contribution is expected to be no greater than a factor of a few [103, 157]. Thus, we conservatively excluded this enhancement when calculating J-factors.

Although the NFW model is widely used for its simplicity and is broadly consistent with the dark matter distribution in simulated subhalos [13], a few caveats should be mentioned. First, simulations with increased resolution have revealed that more scatter exists in the central dark matter density profile than is implied by the NFW profile [176]. In fact, these simulations indicate that the central dark matter density in subhalos is systematically shallower than the r^{-1} central density implied by the NFW model. However, these deviations occur at a scale of $\lesssim 10^{-3}$ of the halo virial radius [176], and thus do not strongly affect the predicted γ-ray flux given the angular resolution of the LAT. Second, subhalos are, in nearly all cases, more severely tidally truncated than the r^{-3} outer density scaling of the NFW profile. For subhalos with large $r_{\rm s}$, using the NFW profile will result in a slight ($< 10\%$) overestimation of the predicted flux.

7.2.2 Extrapolation to Low-Mass Subhalos

The subhalo mass functions for the Aquarius and VL-II simulations are complete down to masses of $\sim 10^6\,M_\odot$. However, theoretical arguments suggest that the mass function of subhalos may extend well beyond this resolution limit. Therefore, it is likely that the subhalos resolved in the Aquarius and VL-II simulations are only a small fraction of the total number of dark matter subhalos bound to our Galaxy. We refer to these unresolved dark matter subhalos with $M_{\rm tidal} < 10^6\,M_\odot$ as "low-mass" subhalos.

To estimate the contribution of low-mass subhalos to the LAT γ-ray search, we extrapolated the distribution of subhalos in VL-II down to $1\,M_\odot$. Assuming a power-law mass function for subhalos, $dN/dM_{\rm tidal} \propto M_{\rm tidal}^{-1.90}$ [173, 177], we calculated the number of subhalos at a given $M_{\rm tidal}$ within 50 kpc of the Galactic center. These low-mass subhalos were distributed within this 50 kpc radius in accordance to the radial distribution described in Madau *et al.* [177]. The cut at 50 kpc is conservative based on the null-detection of the Segue 1 dwarf spheroidal with a tidal mass of $\sim 10^7\,M_\odot$ at ~ 28 kpc from the Galactic center [178].

In order to parameterize the dark matter distribution of low-mass subhalos, we fit probability distributions for $V_{\max}$ and $R_{V_{\max}}$ dependent on M_{tidal}. For VL-II subhalos within 50 kpc of the Galactic center and with $M_{\text{tidal}} > 10^6\,M_\odot$, we found that

$$V_{\max} = V_0 \left(\frac{M_{\text{tidal}}}{M_\odot}\right)^{\beta} \tag{7.4}$$

with $V_0 = 10^{-1.20\pm0.05}\,\text{km}\,\text{s}^{-1}$, $\beta = 0.30 \pm 0.01$, and a log-normal scatter of $\sigma_{V_{\max}} = 0.063\,\text{km}\,\text{s}^{-1}$. Additionally, we found that

$$R_{V_{\max}} = R_0 \left(\frac{M_{\text{tidal}}}{M_\odot}\right)^{\delta} \tag{7.5}$$

with $R_0 = 10^{-3.1\pm0.4}\,\text{kpc}$, $\delta = 0.39 \pm 0.02$, and a log-normal scatter of $\sigma_{R_{V_{\max}}} = 0.136\,\text{kpc}$. Using these relationships, we randomly generated low-mass subhalos consistent with the VL-II simulation down to a tidal mass of $1\,M_\odot$.

7.2.3 Comparison to Dwarf Spheroidal Galaxies

The VL-II simulation, extrapolated as described above, provides a theoretical model for the population of Milky Way dark matter subhalos from $10^{10}\,M_\odot$ to $1\,M_\odot$. A simple estimate of the detectable fraction of these dark matter subhalos can be obtained from the 11-month limits on the dark matter annihilation flux from dwarf spheroidal galaxies [94]. The strongest individual limits on the annihilation cross section from 11 months of data result from the analysis of the Draco dwarf spheroidal, which has a J-factor (integrated over the solid angle of a cone with radius 0.5°) of $\sim 10^{19}\,\text{GeV}^2\,\text{cm}^{-5}$. The central mass of Draco is well known from stellar kinematics [11, 63, 64]; however, the total dark matter mass for Draco is less certain due to the lack of kinematic measurements in the outer regions of the halo. A conservative lower bound on the total dark matter halo mass of Draco is taken to be $10^8\,M_\odot$. Based on this lower bound, we determined the fraction of simulated subhalos that possess a J-factor larger than that of Draco.

The J-factor of a dark matter subhalos can be parameterized as a function of the subhalo mass and heliocentric distance,

$$J \propto \frac{r_{\rm s}^3 \rho_0^2}{D^2} \propto \frac{M_{\rm tidal}^{0.81}}{D^2} \,, \tag{7.6}$$

where we have used the relationships that $r_{\rm s} \propto M^{0.39}$ (from Equations (7.2) and (7.5)) and $\rho_0 \propto M^{-0.18}$ (from Equations (7.2), (7.3), and (7.4)). Equation (7.6) makes it possible to compare the relative astrophysical contribution to the γ-ray flux for different halos based solely on their tidal mass and heliocentric distance. The choice of particle physics annihilation model merely scales all subhalos by the same constant factor.

The J-factors of simulated subhalos are displayed in Figure 7.1, which serves as a guide for evaluating their detectability. While the total number of subhalos increases with decreasing mass, the J-factors of these low-mass subhalos tend to decrease. This means that low-mass subhalos, while dominating the local volume in number, are a sub-dominant contributor to the γ-ray flux at the Earth. Using the procedure discussed in Section 7.5, we verify that extending the VL-II mass function to low mass has a minimal effect ($< 5\%$) when setting upper limits on $\langle \sigma v \rangle$; consequently, we do not consider these subhalos in our primary analysis. For low-mass subhalos to dominate the γ-ray signal, a mechanism must be invoked to either increase the concentration for low-mass subhalos, or decrease the slope of the mass function. Of course, the above statements do not preclude the possibility that a low-mass subhalo with a high J-factor could be located close to Earth.

In the context of the ΛCDM simulations, the LAT may be sensitive to hundreds of dark matter subhalos. In addition to motivating our subhalo search, Figure 7.1 allows us to narrow our focus to those subhalos with the best prospects for detection. Using Equation (7.6), we omitted subhalos with J-factors more than an order of magnitude less than the lower bound on the J-factor for Draco.

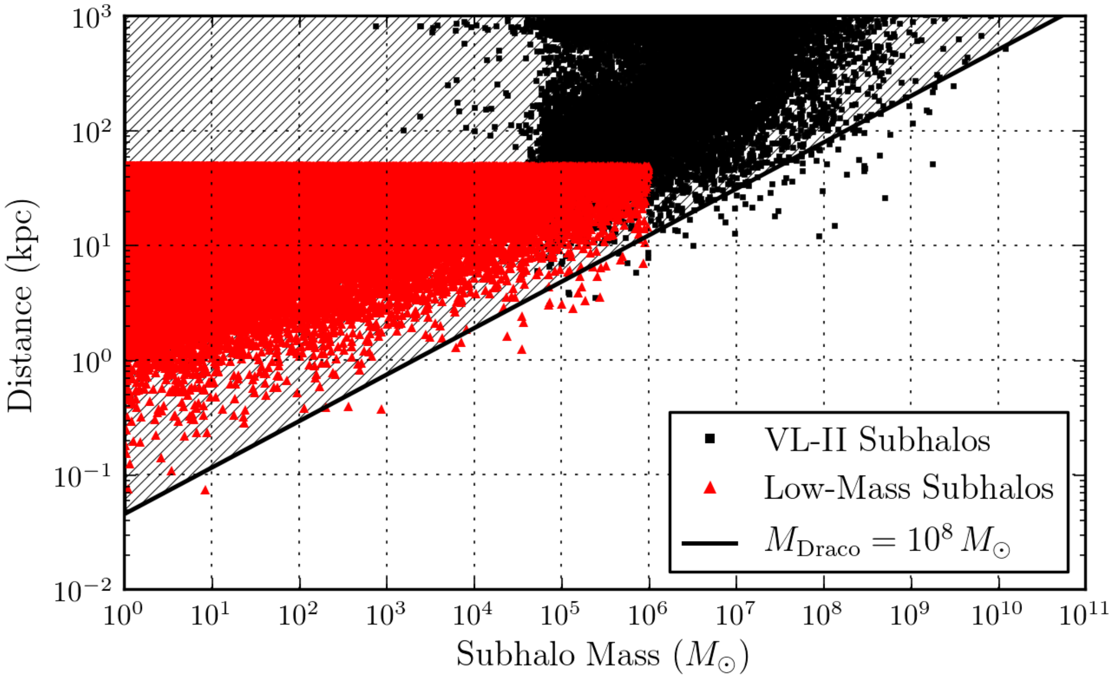

Figure 7.1 Distribution of subhalo mass and distance for the original VL-II subhalos (in black) and the extrapolation to low-mass subhalos (in red). Lower J-factors reside in the upper left while higher J-factors lie to the lower right. Parallel contours of constant J-factor ($J \propto \frac{M^{0.81}}{D^2}$) run from the upper right to the lower left. One such contour is shown for the Draco dwarf spheroidal galaxy assuming a mass of $10^8\,M_\odot$ at a distance of 80 kpc. Subhalos lying in the hatched region above this line have lower J-factors than that of Draco.

7.3 Methods

In this section, we review the analysis of LAT sources lacking associations in other wavelengths with the aim of determining whether any are consistent with being dark matter subhalos. First, we summarize our data set and give an overview of an independent search for LAT sources without spectral assumptions. Then, we describe our procedure for selecting candidate dark matter subhalos using the likelihood ratio test to evaluate the spatial extension and spectral shape of each source. The ability of the LAT to detect spatial extension and spectral shape depends on source flux and spectral hardness. Extensive Monte Carlo simulations were required to determine cuts for rejecting both sources with point-like spatial profiles and sources with power-law spectra at 99% confidence. When combined, these cuts allowed us to select extended, non-power-law sources in our sample of high-Galactic-latitude unassociated LAT source candidates with a contamination level of 1 in 10^4. The work presented in this section is discussed in more detail in Wang [179].

7.3.1 Data Selection

Our data sample consisted of `DIFFUSE` class events from the `Pass 6` processing of the first year of LAT data (2008-08-08 to 2009-08-07) and overlapped substantially with the data used for the 1FGL [87]. To reduce γ-ray contamination from the bright limb of the Earth, we rejected events with zenith angles larger than 105° and events collected during time periods when the rocking angle of the LAT was greater than 47° (the nominal LAT rocking angle was 35° during this time period). Due to calibration uncertainties at low energy and the statistical limitations in the study of the `Pass 6` instrument response functions (IRFs) above 300 GeV, we selected only photons with energies between 200 MeV and 300 GeV. This analysis was limited to sources with Galactic latitudes greater than 20°, since the Galactic diffuse emission complicates source detection and the analysis of spatial extension at lower Galactic latitudes. We modeled the diffuse γ-ray emission with standard 1-year Galactic (*gll_iem_v02.fit*) and isotropic (*isotropic_iem_v02.txt*) background models.[1] Throughout this analysis, we used the Fermi-LAT Collaboration `ScienceTools` `v9r18p1`[2] and the `P6_V3_DIFFUSE` IRFs.[3]

7.3.2 Source Selection

The 1FGL is a collection of high-energy γ-ray sources detected by the LAT during the first 11 months of data taking [87]. It contains 1451 sources, of which 806 are at high Galactic latitude ($|b| > 20°$). Of these high-latitude 1FGL sources, 231 are

---

[1] `http://fermi.gsfc.nasa.gov/ssc/data/access/lat/BackgroundModels.html`

[2] `http://fermi.gsfc.nasa.gov/ssc/data/analysis/software`

[3] `http://fermi.gsfc.nasa.gov/ssc/data/analysis/scitools/overview.html`

unassociated with sources at other wavelengths and constitute the majority of the sources tested for consistency with the dark matter subhalo hypothesis. However, the 1FGL spectral analysis, including the threshold for source acceptance, assumed that sources were point-like with power-law spectra. This decreased the sensitivity of the 1FGL to both spatially extended and non-power-law sources, which are both characteristics that dark matter subhalos are expected to possess. In an attempt to mitigate these biases, we augmented the unassociated sources in the 1FGL with an independent search of the high-latitude sky.

We performed a search for γ-ray sources using the internal Fermi-LAT Collaboration software package, `Sourcelike` [180, 181]. `Sourcelike` performs a binned likelihood fit in two dimensions of space and one dimension of energy. When fitting the spectrum of a source, `Sourcelike` fits the fraction of counts associated with the source in each energy bin independently. The overall likelihood is the product of the likelihoods in each bin. This likelihood calculation has more degrees of freedom than that performed by the `ScienceTool gtlike`, which nominally calculates the likelihood from all energy bins simultaneously according to a user-supplied spectral model. In this analysis, we used 11 energy bins logarithmically spaced from 200 MeV to 300 GeV.

Using `Sourcelike`, we searched for sources in 2496 regions of interest (ROIs) of dimension $10^\circ \times 10^\circ$ centered on `HEALPix` [182] pixels obtained from an order four tessellation of the high-latitude sky ($|b| > 20^\circ$). Each ROI was sub-divided into $0.1^\circ \times 0.1^\circ$ pixels, and for each pixel the likelihood of a point source at that location was evaluated by comparing the maximum likelihood of two hypotheses: (1) that the data were described by the standard LAT diffuse background models without any point sources (H_0), and (2) that the data were described by the existing model with an additional free parameter corresponding to the flux of a source at the target location (H_1). Utilizing the likelihood ratio test, we defined a test statistic (TS):

$$\mathrm{TS} = -2\ln\left(\frac{\mathcal{L}(H_0)}{\mathcal{L}(H_1)}\right) . \tag{7.7}$$

After generating a map of the test statistic over the entire high-latitude sky, we iteratively refit regions around potential source candidates more carefully. The flux normalizations, spectral indices, and emission centroids of candidate sources with TS $>$ 16 were refined while incorporating the flux normalizations of diffuse backgrounds and other candidate point sources (TS $>$ 16) within the ROI as free parameters in the fit. After refitting, only candidate sources with TS $>$ 24 were accepted into the list of source candidates.[4] Finally, to avoid duplicating sources in the 1FGL, we removed candidate sources with 68% localization errors overlapping the 95% error ellipse given for 1FGL sources.

Our search of the high-Galactic-latitude sky revealed 710 candidate sources, of which 154 were not in the 1FGL (36 of these candidate sources were subsequently included in the Second LAT Source Catalog [116]). We did not expect to recover all 806 high-Galactic-latitude 1FGL sources, since the 1FGL is a union of four different detection methods and external seeds from the BZCAT and WMAP catalogs [87]. However, since `Sourcelike` fits each energy bin independently, we expected to find source candidates that were excluded from the 1FGL, either because they had non-power-law spectra or they had hard spectra with too few photons to pass the 1FGL spectral analysis. We sacrificed some sample purity for detection efficiency in our candidate source list because stringent cuts on spatial extent and spectral shape were later applied. We obtained a final list of 385 high-Galactic-latitude unassociated LAT sources and source candidates by combining the 231 unassociated sources in the 1FGL with these 154 non-1FGL candidate sources.

To check for consistency with the source analysis of the 1FGL, we performed an unbinned likelihood analysis with `gtlike` assuming that the unassociated sources were point-like with power-law spectra ($dN/dE \propto E^{-\Gamma}$). Our fitted fluxes and spectral indices are in good agreement with those in the 1FGL for the 231 unassociated 1FGL sources. The values are plotted in Figure 7.2, where it can be seen that the unassociated LAT sources span a wide range of fluxes and spectral indices. The range of source characteristics was taken into account when designing selection criteria for candidate dark matter subhalos. The strong correlation between spectral

---

[4] Monte Carlo simulations show that 1 in 10^4 background fluctuations will be detected at TS $\geq$ 24 when fit with `Sourcelike` [179].

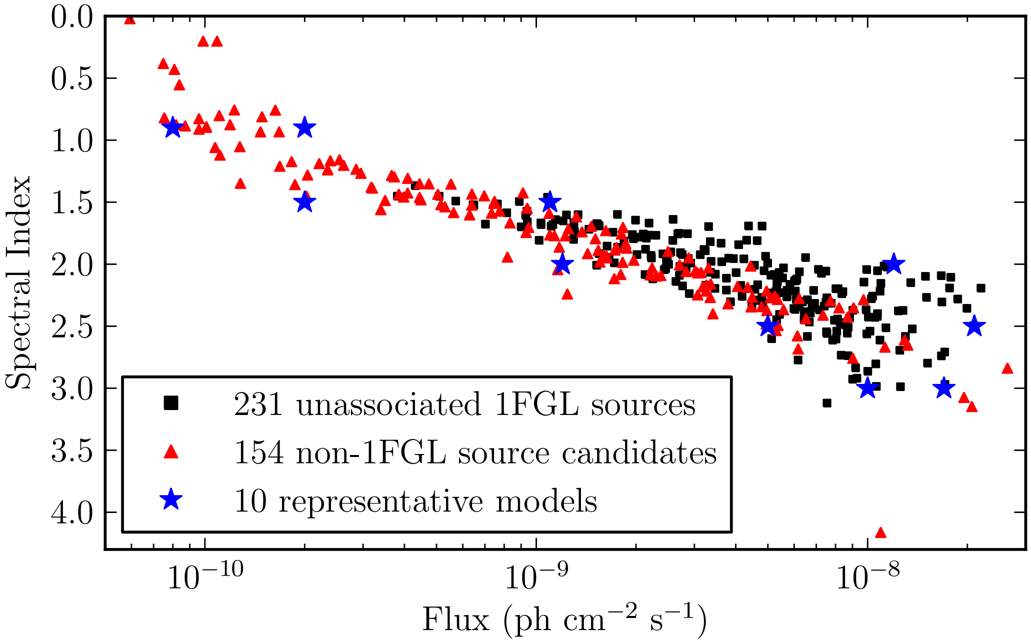

Figure 7.2 Distribution of spectral indices and integral fluxes from 200 MeV to 300 GeV for the 385 high-Galactic-latitude unassociated sources and source candidates. The squares are the 231 unassociated sources from the 1FGL catalog, while the triangles are the 154 additional source candidates detected with `Sourcelike`. The stars are the 10 representative power-law models in Table 7.1.

index and flux is due to the improvement of the point-spread function (PSF) of the LAT with increasing energy and the relatively soft spectrum of the diffuse Galactic γ-ray background. It is apparent that there are more non-1FGL source candidates in this sample with very hard spectra (spectral index $\Gamma \sim 1.0$) and very low fluxes ($\sim 10^{-10}$ ph cm^{-2} s^{-1}). Wang [179] show that these source candidates are very likely spurious.

7.3.3 Spatial Extension Test

The LAT has the potential to resolve some dark matter subhalos as spatially extended γ-ray sources. While the bulk of subhalos are not spatially resolvable by the LAT, spatial extension is an important feature for distinguishing large or nearby subhalos from point-like astrophysical sources (see Section 7.2). Assuming that the intrinsic spatial and spectral distributions of γ rays produced from dark matter annihilation factorize, the shape of the projected dark matter distribution is convolved with the LAT PSF (Equation (4.3)). For an NFW density profile with scale radius $r_{\rm s}$ at a distance D, the angular extent of a subhalo can be characterized by the parameter $\alpha_{\rm s} \equiv r_{\rm s}/D$, which defines a solid angle cone containing $\sim$90% of the integrated J-factor [183]. The LAT is expected to be sensitive to the spatial extension of subhalos with $\alpha_{\rm s} > 0.5°$ [184].

We used the likelihood ratio test, as implemented by `Sourcelike`, to test sources for spatial extension. We defined a test statistic for extension as,

$$\begin{aligned} \mathrm{TS}_{\rm ext} &= -2\ln\left(\frac{\mathcal{L}(H_{\rm point})}{\mathcal{L}(H_{\rm NFW})}\right) \qquad (7.8) \\ &= \mathrm{TS}_{\rm NFW} - \mathrm{TS}_{\rm point}\,, \qquad (7.9) \end{aligned}$$

where $\mathrm{TS}_{\rm point}$ was the test statistic of the candidate source assuming that it had negligible extension ($\alpha_{\rm s}$ much smaller than the LAT PSF) and $\mathrm{TS}_{\rm NFW}$ was the test statistic of the candidate source when $\alpha_{\rm s}$ was fit as a free parameter. In both cases, the position of the source was optimized during the fit.

We defined a cut on the value of $\mathrm{TS}_{\rm ext}$ to eliminate 99% of point sources over the range of spectral indices and fluxes found in the unassociated LAT sources (Figure 7.2). This cut was labeled $\mathrm{TS}_{\rm ext}^{99}$. While the point and extended hypotheses are nested and $\mathrm{TS}_{\rm ext}$ is cast as a likelihood ratio test, it is unclear whether this analysis satisfied all of the suitable conditions for the application the theorems of Wilks [85] or Chernoff [86]. Therefore, we relied on simulations to parameterize $\mathrm{TS}_{\rm ext}^{99}$ as a function of source flux and spectral index.

To evaluate $\mathrm{TS}_{\rm ext}^{99}$ over the pertinent range of source fluxes and spectral indices, the unassociated LAT sources were bracketed with 10 representative power-law models (Table 7.1 and blue stars in Figure 7.2). For each of the 10 representative models, 1000 independent sources were simulated at random locations in the high-Galactic-latitude sky using the LAT simulation tool, `gtobssim`, and the spacecraft pointing history for our one-year data set. To accurately incorporate imperfect modeling of

Table 7.1. Gamma-ray selection criteria for dark matter subhalo candidates.

Model Number	Spectral Index	Flux[(a)] ($\mathrm{ph\,cm^{-2}\,s^{-1}}$)	$\mathrm{TS}_{\mathrm{ext}}^{99}$	$\mathrm{TS}_{\mathrm{spec}}^{99}$
1	0.9	2.0×10^{-10}	6.18	2.38
2	0.9	8.0×10^{-11}	7.87	2.46
3	1.5	1.1×10^{-9}	5.09	4.96
4	1.5	2.0×10^{-10}	14.98	2.88
5	2.0	1.2×10^{-8}	5.11	2.24
6	2.0	1.2×10^{-9}	9.63	4.28
7	2.5	2.1×10^{-8}	6.74	1.78
8	2.5	0.5×10^{-8}	10.78	5.66
9	3.0	1.7×10^{-8}	9.81	2.14
10	3.0	1.0×10^{-8}	11.87	6.02

[(a)] Integral flux from 200 MeV to 300 GeV.

Note. — Cut values excluding point-like sources ($\mathrm{TS}_{\mathrm{ext}}^{99}$) and sources with power-law spectra ($\mathrm{TS}_{\mathrm{spec}}^{99}$) at 99% confidence. These values are independent of the TS > 24 cut and were calculated from Monte Carlo simulations of the 10 typical power-law point source models.

background point and diffuse sources, we embedded the simulated point sources in one year of LAT data and calculated $\mathrm{TS}_{\mathrm{ext}}$ for each simulated source. We defined $\mathrm{TS}_{\mathrm{ext}}^{99}$ for each representative model as the smallest value of $\mathrm{TS}_{\mathrm{ext}}$ that was larger than that calculated for 99% of simulated point sources. The values of $\mathrm{TS}_{\mathrm{ext}}^{99}$ for all 10 models were calculated independently of the TS > 24 detection cut and are listed in Table 7.1.

We used a bilinear interpolation to estimate the value of $\mathrm{TS}_{\mathrm{ext}}^{99}$ for any point in the space spanned by the grid of flux and spectral index. Since each measurement of source flux and spectral index has a statistical uncertainty, we interpolated to the largest value of $\mathrm{TS}_{\mathrm{ext}}^{99}$ that was consistent with the $\pm 1\sigma$ error for each source to derive a conservative estimate of $\mathrm{TS}_{\mathrm{ext}}^{99}$.

7.3.4 Spectral Test

We designed a test for spectral curvature in order to select sources that were spectrally consistent with dark matter annihilation. The continuum γ-ray emission from dark matter annihilation is composed of secondary photons from tree-level annihilations [172, 185] and additional photons from QED corrections – i.e., final state radiation (FSR) and virtual internal bremsstrahlung (VIB) [147]. For tree-level annihilations, the leading channels among the kinematically allowed final states are predicted to be $b\bar{b}$, $t\bar{t}$, W^+W^-, Z^0Z^0, and $\tau^+\tau^-$. The γ-ray spectra from these channels are quite similar, except for the τ-channel which is considerably harder [185]. We chose the $b\bar{b}$ channel as a representative proxy for the tree-level annihilation spectrum.

We defined a test statistic to evaluate the consistency of the data with dark matter and power-law spectra. This spectral test statistic,

$$\begin{aligned} \mathrm{TS}_{\mathrm{spec}} &= -2\ln\left(\frac{\mathcal{L}(H_{\mathrm{pwl}})}{\mathcal{L}(H_{b\bar{b}})}\right) \\ &= \mathrm{TS}_{b\bar{b}} - \mathrm{TS}_{\mathrm{pwl}}\,, \end{aligned} \tag{7.10}$$

was defined as the difference in source TS calculated with an unbinned analysis using `gtlike` assuming a $b\bar{b}$ dark matter spectral model ($\mathrm{TS}_{b\bar{b}}$) and a power-law spectral model ($\mathrm{TS}_{\mathrm{pwl}}$). These two hypotheses are not nested, and thus the significance of this test was evaluated with simulations. When performing our fits, we modeled candidate sources as point-like and left their fluxes and the fluxes of the diffuse backgrounds free.[5] Additionally, the power-law and dark matter spectral models each contain a spectral free parameter (the dark matter mass or power-law index).

Using the same representative simulations described in Section 7.3.3, we defined $\mathrm{TS}_{\mathrm{spec}}^{99}$ to be the value of $\mathrm{TS}_{\mathrm{spec}}$ which was larger than that calculated for 99% of simulated power-law sources (Table 7.1). When calculating $\mathrm{TS}_{\mathrm{spec}}^{99}$ for a particular source, we chose the largest value from a bilinear interpolation to the $\pm 1\sigma$ errors on fitted flux and spectral index (as discussed at the end of Section 7.3.3). These tests of spatial extension and spectral character allowed us to select non-point-like and

---

[5] From simulations, this has been found to be a conservative way to estimate $\mathrm{TS}_{\mathrm{spec}}$ [179].

non-power-law sources with a contamination of 1 in 10^4 assuming that theses tests were independent.

7.4 Results

7.4.1 Search for Dark Matter Subhalos

We applied the cuts on spatial extension and spectral character to select DM subhalo candidates from the 385 unassociated high-latitude LAT sources and source candidates. Two unassociated sources, 1FGL J1302.3−3255 and 1FGL J2325.8−4043, passed the cut on spatial extension. One of these, 1FGL J1302.3−3255, also passed our spectral test, preferring a $b\bar{b}$ spectrum to a power-law spectrum. As their names imply, both 1FGL J1302.3−3255 and 1FGL J2325.8−4043 are present in the 1FGL [87], and we summarize the γ-ray characteristics of each source in Table 7.2. However, we do not believe that either of these sources is a viable DM subhalo candidate for reasons discussed below.

While 1FGL J1302.3−3255 was unassociated when the 1FGL was published, and has previously been considered as a promising dark matter subhalo candidate [186], it has since been associated with a millisecond pulsar by radio follow-up observation [187]. The other possibly extended source, 1FGL J2325.8−4043, has a high probability of association with two AGN in the first LAT AGN Catalog [188]. 1FGL J2325.8−4043 is assigned a 70% probability of association to 1ES 2322−409 and a 55% probability of association with PKS 2322−411.

Since AGN are not expected to be spatially extended at an angular scale resolvable by the LAT, we cross checked 1FGL J2325.8−4043 against the Second LAT Source Catalog [116]. In two years of data, two sources were found within 0.5° of the location of 1FGL J2325.8−4043. In one year of data, these two sources could not be spatially resolved, but their existence was enough to favor an extended source hypothesis. Spurious measurements of a finite extent for point sources are not unexpected. Testing extension with a purity of 99%, the Poisson probability of finding at least one spurious source in our 385 tests is 98%. Since 1FGL J1302.3−3255 is associated with a pulsar

Table 7.2. Characteristics of two candidate high-latituded extended γ-ray sources.

Source Name	ℓ (deg)	b (deg)	Flux$^{(b)}$ (ph cm^{-2} s^{-1})	$\alpha_{\rm s}$ (deg)	TS$_{\rm ext}$	TS$_{\rm spec}$
1FGL J1302.3−3255	305.58	29.90	1.33×10^{-8}	1.2	9.3	4.6
1FGL J2325.8−4043	349.83	−67.74	2.12×10^{-8}	1.3	13.2	−19.1

Column Definitions. — (1) 1FGL source name, (2) Galactic longitude, (3) Galactic latitude, (4) integral flux from 200 MeV to 300 GeV interpolated from the best-fit power-law model, (5) best-fit spatial extension using an NFW profile, (6) TS-value from spatial extension test, and (7) TS-value from spectral test. Columns (1)–(4) are derived from Abdo *et al.* [87].

and 1FGL J2325.8−4043 does not appear to be truly extended, we conclude that there were no unassociated, high-latitude spatially extended γ-ray sources in the first year of LAT data. Thus, according to the criteria defined in Section 7.3, no viable dark matter subhalo candidates were found.

7.4.2 Contamination from Pulsars

To better understand possible misidentification of pulsars (i.e., 1FGL J1302.3−3255) as candidate dark matter subhalos, we applied our test of spectral shape to 25 high-latitude LAT-detected pulsars. Of these 25 pulsars, 14 were identified when the 1FGL was published and 11 were subsequently identified through follow-up observations by radio telescopes [187].

Interestingly, 24 of these pulsars passed our spectral cut, preferring a $b\bar{b}$ spectrum to a power-law spectrum. This can be understood by comparing the exponentially cutoff power-law model commonly used to fit pulsars with a $b\bar{b}$ annihilation spectrum. The exponentially cutoff power law has the form [189],

$$\frac{dN}{dE} = K \left(\frac{E}{1\,\mathrm{GeV}}\right)^{-\Gamma} \exp(-\frac{E}{E_{\rm cut}})\,, \tag{7.11}$$

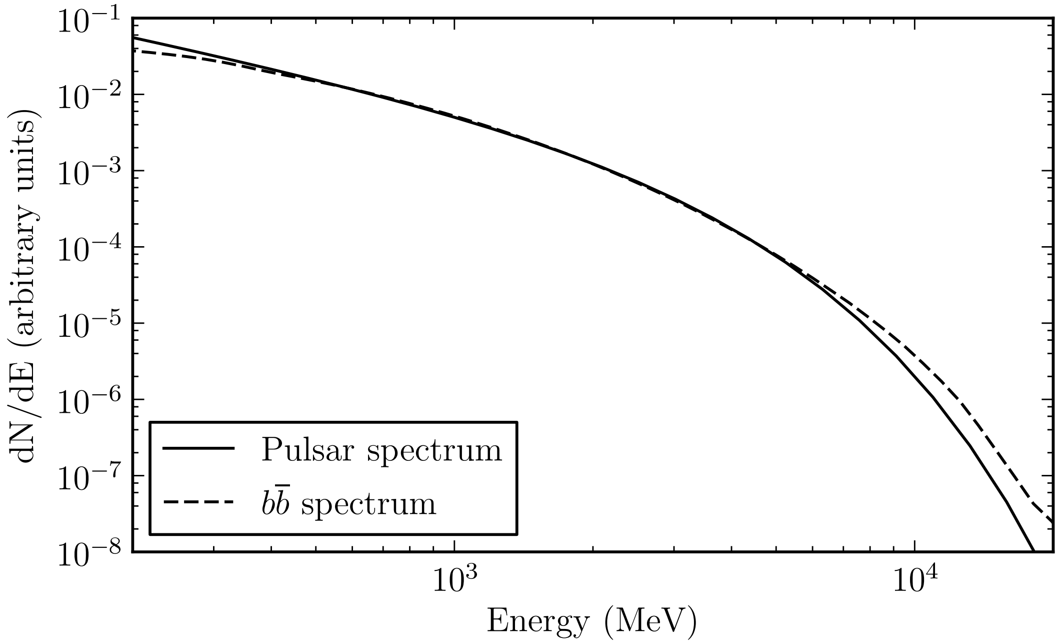

Figure 7.3 Best-fit exponentially cutoff power law (with $\Gamma = 1.22$ and $E_{\rm cut} = 1.8\,{\rm GeV}$) of the millisecond pulsar 1FGL J0030+0451 (solid line) and the best-fit $b\bar{b}$ spectrum (with $m_{\rm DM} = 25\,{\rm GeV}$) of this pulsar (dashed line).

where Γ is the photon index at low energy, $E_{\rm cut}$ is the cutoff energy, and K is a normalization factor (with units of ${\rm ph\,cm^{-2}\,s^{-1}\,MeV^{-1}}$). In Figure 7.3, we plot both the exponentially cutoff power-law model and a low-mass ($m_{\rm DM} \sim 25\,{\rm GeV}$) $b\bar{b}$ spectrum and show that for $E > 200\,{\rm MeV}$ the two curves are very similar.

By fitting $b\bar{b}$ spectra to the 25 LAT-detected pulsars, we found that they tend to be best fit by low dark matter masses (Figure 7.4). Although our statistics are limited, the distribution peaks around $m_{\rm DM} \sim 30\,{\rm GeV}$, with most pulsars having a best-fit dark matter mass $m_{\rm DM} < 60\,{\rm GeV}$. This suggests that unidentified, high-latitude pulsars can present a source of confusion in spectral searches for dark matter subhalos. In general, many unassociated LAT sources have spectra that are inconsistent with a power-law model [116, 190]. The fact that these sources passed our spectral test does not imply that they are best fit by $b\bar{b}$ spectra, merely that $b\bar{b}$ spectra fit better than a simple power law. These unassociated, non-power-law sources were not found

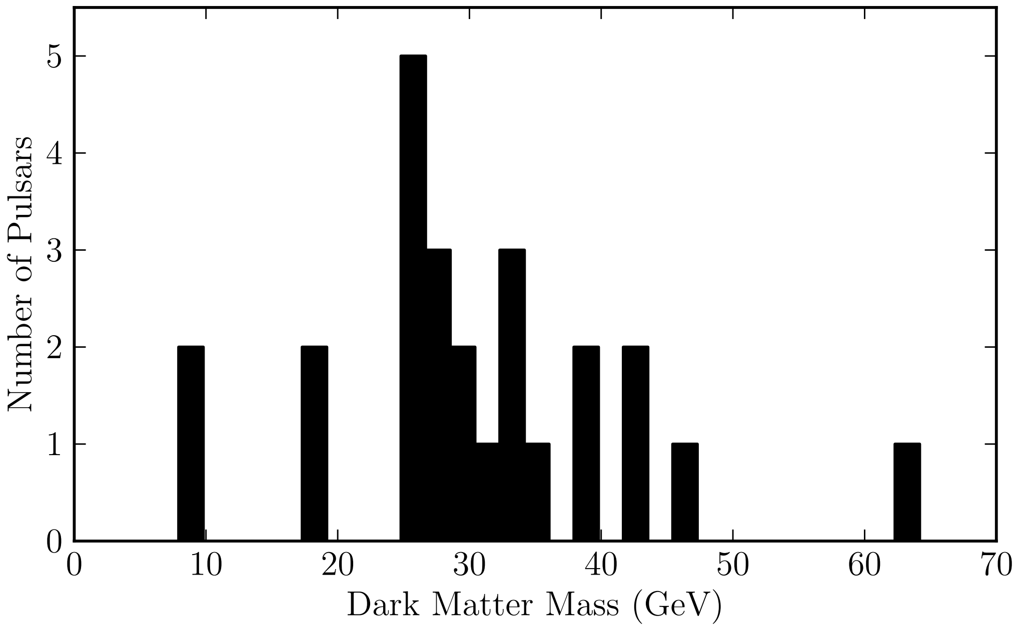

Figure 7.4 Best-fit dark matter mass derived by fitting 25 high-latitude ($|b| > 20°$) pulsars with $b\bar{b}$ annihilation spectra.

to share a consistent spectrum, as would be expected from dark matter annihilation.

The abundance of non-power-law γ-ray sources emphasizes the importance of testing for spatial extension when attempting to identify dark matter subhalos at high latitudes. Some concerns remain due to the fact that the LAT detects spatially extended pulsar wind nebulae coincident with some pulsars [191]. However, we do not expect the older pulsars at high Galactic latitudes to have nebulae that are spatially resolvable by the LAT. Of course, there is always a risk that a chance coincidence with a low-flux neighboring source will cause apparent source extension.

7.5 Interpretation Using N-body Simulations

No high-latitude unassociated LAT source candidates passed our dark matter subhalo selection criteria. We combined this result with the N-body simulations discussed in

Section 7.2 to constrain a conventional 100 GeV dark matter particle annihilating through the $b\bar{b}$ channel. Monte Carlo simulations were used to determine the detection efficiency for dark matter subhalos as a function of flux and spatial extension. For multiple realizations of each ΛCDM simulation, we calculated the probability of detecting no subhalos from the detection efficiency of each simulated subhalo. Averaging over these simulations and increasing $\langle\sigma v\rangle$ until the probability of detecting no subhalos drops below 5%, we were able to set an upper limit on $\langle\sigma v\rangle$ at 95% confidence.

7.5.1 Detection Efficiency

The detection efficiency of our selection was defined as the fraction of dark matter subhalos that passed the cuts in Section 7.3 and was calculated from Monte Carlo simulations. The efficiency for detecting a dark matter subhalo depended on spectral shape (i.e., dark matter mass and annihilation channel), flux, and spatial extension. For a 100 GeV dark matter particle annihilating through the $b\bar{b}$ channel, we examined the efficiency for subhalos with characteristic fluxes ranging from $5 \times 10^{-11}\,\mathrm{ph\,cm^{-2}\,s^{-1}}$ to $5 \times 10^{-8}\,\mathrm{ph\,cm^{-2}\,s^{-1}}$ and characteristic spatial extension (as described in Section 7.3.3) from 0.5° to 2.0°. These ranges were chosen to reflect the fluxes of the unassociated high-latitude LAT sources and angular extents to which the LAT is sensitive.[6]

For each set of characteristics listed in Table 7.3, we utilized `gtobssim` to simulate 200 dark matter subhalos with NFW profiles and spectra consistent with annihilation of a 100 GeV dark matter particle through the $b\bar{b}$ channel. These simulations were embedded in the LAT data at random high-latitude locations, and `Sourcelike` was used to compute $\mathrm{TS_{ext}}$, $\mathrm{TS_{spec}}$, and the detection TS for each. The subhalo detection efficiency was computed as the fraction of subhalos with `Sourcelike` TS > 24, $\mathrm{TS_{ext}} > \mathrm{TS^{99}_{ext}}$, and $\mathrm{TS_{spec}} > \mathrm{TS^{99}_{spec}}$. The first requirement was included as a proxy for the efficiency of the source finding algorithm. The creation of this efficiency table

---

[6] The 68% containment radius of the LAT PSF, which depends on photon energy and angle of incidence, can be approximated by the function, $0.8^\circ(\frac{E}{1\,\mathrm{GeV}})^{-0.8}$ [87], yielding $\sim 0.8^\circ$ at 1 GeV and $\sim 0.13^\circ$ at 10 GeV.

Table 7.3. Dark matter subhalo detection efficiency.

Flux		Extension	
($\mathrm{ph\,cm^{-2}\,s^{-1}}$)	0.5°	1.0°	2.0°
0.2×10^{-8}	<0.05	<0.05	<0.05
0.5×10^{-8}	0.16	0.28	0.31
1.0×10^{-8}	0.74	0.76	0.83
2.0×10^{-8}	0.99	1.0	0.99
5.0×10^{-8}	1.0	1.0	1.0

Column Definitions. — (1) Subhalo integral flux from 200 MeV to 300 GeV, (2)–(4) subhalo spatial extension parameterized by an NFW profile with $\alpha_{\mathrm{s}} \equiv r_{\mathrm{s}}/D$.

Note. — Subhalo detection efficiency as a function of flux and spatial extension for a 100 GeV dark matter particle annihilating through the $b\bar{b}$ channel.

(Table 7.3) was computationally intensive and model dependent, limiting this analysis to the examination of only the 100 GeV $b\bar{b}$ model. To expedite the generation of this table, we found the flux value with 5% efficiency and conservatively set the efficiency for sources with less flux to zero.

7.5.2 Simulated Subhalo Distributions

The VL-II and Aquarius simulations (described in Section 7.2) were used to predict the Galactic dark matter subhalo population. Picking a vantage point 8.5 kpc from the center of each simulation (the solar radius), we calculated the spatial extension and integrated J-factor for each simulated subhalo. To account for variation in the local subhalo population, we repeated this procedure, creating six realizations from maximally separated vantage points at the solar radius. It is important to note that while the VL-II and six Aquarius simulations are statistically independent, these different realizations are not – i.e., the same subhalos appear in multiple realizations.

Thus, we have seven independent simulations, each with six not-independent realizations (collectively referred to as 42 "visualizations").

After excluding undetectable subhalos with J-factors an order of magnitude less than the lower bound the J-factor of Draco (Section 7.2.2), we compared the distributions of J-factors and spatial extensions across the visualizations. We found reasonable agreement in the detectable subhalo distributions between the VL-II and Aquarius simulations. The variation in the number of subhalos in each bin of flux and spatial extension was much larger between different simulations than between realizations of the same simulation (as is expected due to the correlation between realizations). On average, subhalos with $\alpha_{\mathrm{s}} > 0.5^\circ$ make up ∼30% of the total integrated J-factor from subhalos in these simulations.

7.5.3 Upper Limits

For each of the 42 visualizations of VL-II and Aquarius, we calculated the γ-ray fluxes of all subhalos for a given $\langle \sigma v \rangle$ using Equation (2.6). With these fluxes and the true spatial extension for each subhalo, we performed a bilinear interpolation on Table 7.3 to determine the detection efficiency for each subhalo. The probability that the LAT would observe none of the subhalos in visualization i is

$$\mathcal{P}_i(\langle \sigma v \rangle) = \prod_j \left(1 - \epsilon_{i,j}(\langle \sigma v \rangle)\right) , \tag{7.12}$$

where $\epsilon_{i,j}$ is the detection efficiency for subhalo j in visualization i. Because there is no reason to favor any one visualization, we calculated the average null detection probability over the $N = 42$ visualizations as

$$\overline{\mathcal{P}}(\langle \sigma v \rangle) = \frac{1}{N} \sum_i^N \mathcal{P}_i(\langle \sigma v \rangle) \, . \tag{7.13}$$

To set an upper limit on the dark matter annihilation cross section, we increased $\langle \sigma v \rangle$ until the probability of a null observation was, $\overline{\mathcal{P}} = 0.05$. This corresponds to 95% probability that, for this $\langle \sigma v \rangle$, at least one subhalo would have passed our selection criteria. Using this methodology, the LAT null detection constrains $\langle \sigma v \rangle$ to be less than $1.95 \times 10^{-24}\,\mathrm{cm^3\,s^{-1}}$ for a 100 GeV dark matter particle that annihilates through the $b\bar{b}$ channel.

7.6 Discussion

We performed a search for unassociated dark matter subhalos using one year of LAT data. After completing an independent search for γ-ray sources, we constructed tests to evaluate both source extension and spectral shape. We distinguished dark matter subhalo candidates by selecting spatially extended sources with γ-ray spectra consistent with dark matter annihilation to $b\bar{b}$. Our initial scans selected two potentially extended sources; however, follow-up analyses revealed that neither of them was a valid dark matter subhalo candidate. Therefore, we concluded that, given our predefined search criteria, there were no signals of dark matter subhalos in the first year of LAT data.

Using the ΛCDM-based Aquarius and Via Lactea II simulations of the Galactic dark matter distribution, we estimated the number of dark matter subhalos that could be observed assuming a 100 GeV dark matter particle annihilating to $b\bar{b}$ with varying cross section. We quantified the detection efficiency for these subhalos, and used it to set an upper limit on the velocity averaged annihilation cross section of $1.95 \times 10^{-24}\,\mathrm{cm^3\,s^{-1}}$ for a 100 GeV dark matter particle annihilating to $b\bar{b}$. This limit is approximately 60 times greater than the expected value of the thermal relic cross section, and it is about an order of magnitude less stringent than the best one-year limit from known dwarf spheroidals [94]. This difference in upper limits can be accounted for by the fact that the analysis of dwarf spheroidals effectively probes the flux limit of the LAT detector, while our selection on spatial extension and spectral shape limits us to higher source fluxes.

Chapter 8

Outlook

Gamma-ray searches for Galactic dark matter substructure are currently one of the most sensitive and robust probes of dark matter annihilation. In this chapter, we consider ways to improve γ-ray searches for dark matter substructure through improvements to the LAT instrument performance and through upcoming wide-field optical surveys. We project that with increased γ-ray exposure and the discovery of 20 new dwarf spheroidal galaxies, it may be possible to probe the thermal relic cross section for dark matter particle masses of $\lesssim 300\,\mathrm{GeV}$. We expect the next decade to be an exciting time in the search for dark matter.

8.1 LAT Instrument Performance

The most obvious improvement to the LAT sensitivity will come from extended data taking. Figure 5.4 shows that the dwarf galaxy ROIs are currently limited by photon statistics at energies $\gtrsim 10\,\mathrm{GeV}$. The lack of background in the high-energy regime is the dominant reason that the LAT flux sensitivity is roughly an order of magnitude better for sources with hard γ-ray spectra than for their soft counterparts (Figure 6.4). Intuitively, in background-dominated regimes the source sensitivity will increase as the square root of the exposure, while in background-free regimes the source sensitivity will increase linearly with the exposure. Thus we expect the sensitivity to hard, high-mass dark matter models to increase more quickly than their soft low-mass counterparts.

The Fermi-LAT Collaboration has also undertaken a major effort, known as `Pass 8`, to radically expand the scientific capabilities of the LAT instrument (Appendix A). `Pass 8` will improve the LAT performance by increasing the effective area, improving the high-energy PSF, and decreasing the residual particle background. Improvements from `Pass 8` will increase the sensitivity of the LAT to faint sources and improve the ability of the LAT to identify spatially extended sources. Additionally, `Pass 8` will correct for systematic effects arising from charged particle pile-up at a more basic level than previous iterations of the event-level analysis. Thus, we expect both the study of dwarf galaxies and the search for unassociated dark matter subhalos to benefit from improvements in the LAT performance and extended operations.

The LAT sensitivity to dark matter annihilation in an individual dwarf spheroidal galaxy will scale roughly with the flux sensitivity of the LAT. However, the combined search for dwarf galaxies may benefit more from the ability to better characterize the LAT instrument than from increased sensitivity. Studies in Section 5.4.5 suggest that the ability of the LAT to confidently detect faint high-Galactic-latitude sources may be limited by systematic effects. Part of these systematics likely arises from inaccurate modeling of the instrument performance. For example, in `Pass 6`, out-of-time particle contamination was manifested as systematic difference between the instrument response functions derived from simulations and the true instrument performance. This offset has been mitigated at the level of event classification in `Pass 7`; however, recent studies of the inclusive photon spectrum suggest that pile-up may still contribute at the few percent level in the range from 1 GeV to 10 GeV [192]. Such a discrepancy would masquerade as an “excess” of photons in this energy regime when compared to the expectation from simulations. Upcoming improvements from `Pass 8` promise to correct for pile-up at the more basic level of event reconstruction (see Appendix A for more detail).

The sensitivity of LAT searches for unassociated subhalos will have a complicated dependence on improvements to the LAT instrument and increased data collection. Increased observation time will provide a longer baseline for identifying γ-ray sources through multi-wavelength studies of correlated variability, thus decreasing the background of unassociated sources with conventional astrophysical origin. A better PSF and increased photon statistics will allow for more efficient identification of spatially extended sources. Additionally, with greater photon statistics it will be possible to better characterize the spectra of unidentified sources. Improvements to the LAT instrument will combine to yield more efficient subhalo selection and a lower astrophysical background. Preliminary studies show that with an elevated selection efficiency, the search for unassociated subhalos could theoretically achieve a sensitivity similar to the current combined dwarf spheroidal analyses [193]. Of course, this is contingent on current dark-matter-only N-body simulations, which will themselves evolve over the coming years.

8.2 Optical Surveys

Perhaps one of the most exciting prospects in the search for Galactic dark matter substructure comes from new wide-field optical surveys. Over the last decade, the Sloan Digital Sky Survey (SDSS) [194] has revolutionized the discipline of near-field cosmology by nearly doubling the known population of Milky Way satellite galaxies [195]. In fact, the discovery of ultra-faint dwarf galaxies was only possible due to the deep, uniform, wide-field survey of SDSS ($\sim 11{,}000\,\mathrm{deg}^2$ to a limiting r-band magnitude of 22.2) [196]. Within the SDSS footprint, Walsh *et al.* [197] conclude the census of classical dwarf galaxies with $L_V \gtrsim 3 \times 10^5\,L_\odot$ is 99% complete; however, the completeness of current SDSS searches quickly degrades for low-luminosity galaxies. Additionally, surveys of the remaining $\sim 75\%$ of the sky not covered by SDSS may be incomplete for even the brightest classical dwarfs ($L_V \sim 2 \times 10^6\,L_\odot$) [198]. As new surveys begin to uniformly cover the entire sky to a greater depth than SDSS we are poised to enter yet another era of rapid dwarf spheroidal galaxy discovery.

The upcoming period of dwarf spheroidal satellite discovery will be driven by four new wide-field optical surveys. Pan-STARRS [155] and Southern Sky Survey [199] are two projects that have embarked on the ambitious tasks of performing surveys of the entire northern and southern skies, respectively, to the same limiting depth

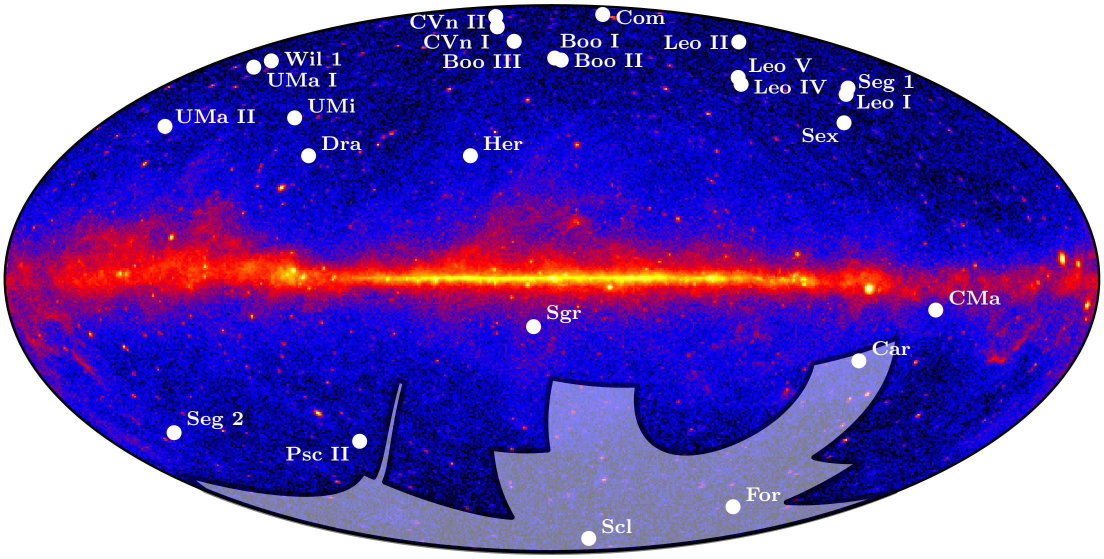

Figure 8.1 Known dwarf spheroidal satellite galaxies of the Milky Way overlaid on a 4-year, HAMMER-AITOFF projected, integrated γ-ray counts map ($E > 1$ GeV). The inhomogeneous distribution of dwarf galaxies reflects the incompleteness of current optical surveys. Near-future wide-field optical surveys will greatly improve upon this coverage over the coming decade. As an example, the proposed 5,000 deg^2 southern sky footprint of DES is overlaid in gray.

as SDSS. The Dark Energy Survey (DES) [156] promises a wide-field photometric survey of 5,000 deg^2 in the southern sky to a deeper limiting r-band magnitude of 24 (Figure 8.1). In addition to the nominal 5,000 deg^2 survey, the DES telescope and camera will be available for community observation time, likely increasing the total survey area significantly. Finally, the flagship of deep, large-field surveys is the Large Synoptic Survey Telescope (LSST) [200]. LSST proposes to cover $\sim$20,000 deg^2 to an unprecedented limiting r-band magnitude of 27.5; however, LSST trails the other three missions by $\sim$10 years [200].

8.3 Projections for Future Dwarf Spheroidal Galaxy Searches

These upcoming wide-field surveys may lead to the discovery of hundreds of new dwarf galaxies [77]. Within the duration of an extended LAT mission, Tollerud *et al.* [77] predict that DES may discover 19 to 37 new dwarf galaxies. Since DES will survey an unexplored region of the southern sky to unprecedented depth, we expect that many of the dwarfs found by DES will be similar in character to those recently discovered in SDSS. In other words, we expect to find a significant population of nearby, ultra-faint dwarf galaxies. The joint likelihood mechanism discussed in Chapter 5 will make it possible to directly incorporate these new galaxies into γ-ray searches for dark matter. The joint likelihood mechanism implies that the addition of a new set of dwarf galaxies will increase the sensitivity of the LAT dwarf galaxy search in a manner similar to increased exposure time.

The tools developed in Section 5.4.2 for generating expected sensitivity curves can easily be adapted to calculate the projected sensitivity of future LAT searches for dwarf galaxies. Here, we present projections for a future search using 35 dwarf spheroidal galaxies and 10 years of LAT γ-ray data. Our set of dwarf galaxies included the 15 known dwarf galaxies selected in Section 5.4 and was augmented by a projected set of 20 new dwarf galaxies possessing similar characteristics to the galaxies discovered in SDSS. In the interest of simplicity, the 20 new dwarf galaxies were chosen to duplicate the 10 SDSS-discovered dwarf galaxies possessing dynamically determined J-factors (i.e., Bootes I, Canes Venatici I, Canes Venatici II, Coma Berenices, Hercules, Leo IV, Segue 1, Ursa Major I, Ursa Major II, and Willman 1). We generated 500 independent 10-year simulations of LAT operation assuming the current instrument performance and models of the diffuse and point-like γ-ray backgrounds. For each simulation, we randomized the sky positions of all 35 dwarf galaxies, requiring that they be placed at high-Galactic-latitude ($|b| > 20^{\circ}$), far ($> 1^{\circ}$) from 2FGL sources, and in non-overlapping regions of the sky. We also randomized the J-factors of all dwarfs in accord with the posterior probability distribution determined from stellar kinematics. We followed the procedure in Chapter 5 to form a joint likelihood

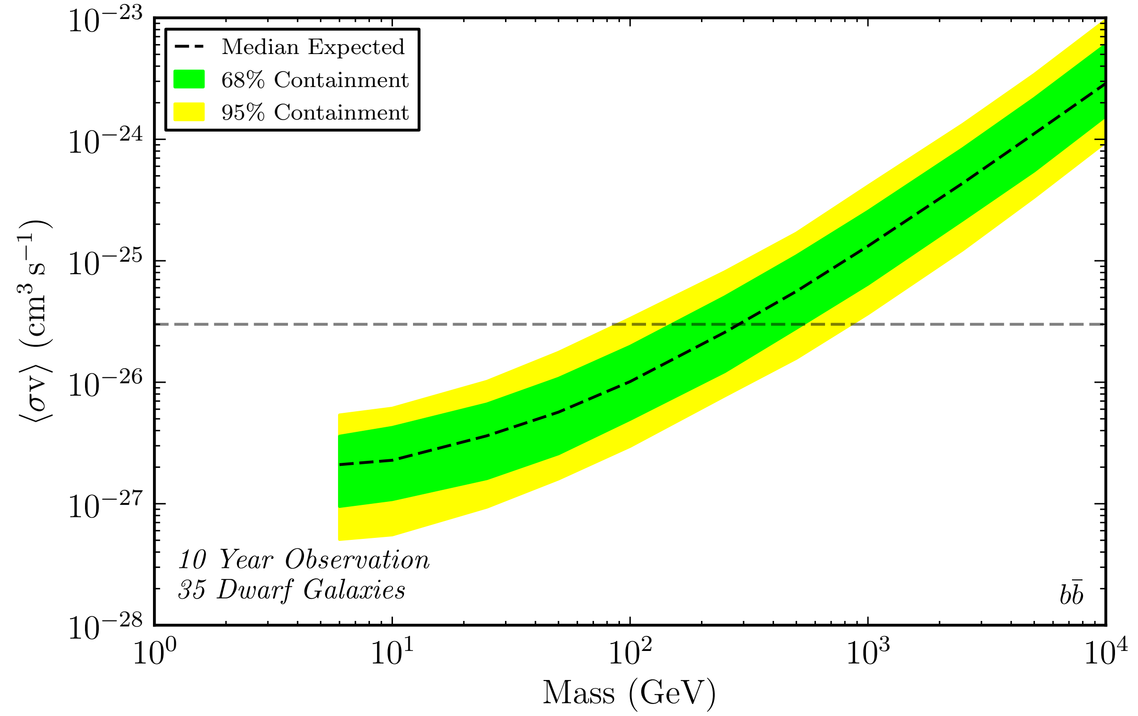

Figure 8.2 Projected sensitivity for a combined dwarf search using 10 years of LAT data and 35 dwarf spheroidal galaxies. The set of dwarf spheroidal galaxies is composed of the 15 dwarf galaxies studied in Section 5.4 and 20 additional dwarf galaxies selected to be consistent with those recently discovered in SDSS. 500 simulations of the LAT data are generated according to the same methodology as in Section 5.4 and assuming the current `Pass 7` instrument performance.

from all 35 dwarf galaxies and plot the expected sensitivity in Figure 8.2. For annihilation into $b\bar{b}$, we project that future LAT searches for dwarf galaxies will be able to probe the thermal relic cross section up to dark matter masses of $\sim 300\,\mathrm{GeV}$. We emphasize that our projections are based on two important assumptions: (1) that the 20 newly discovered dwarf spheroidal galaxies possess characteristics similar to those recently discovered in SDSS, and (2) that systematic effects associated with the LAT search in Section 5.4.5 can be mitigated by `Pass 8`. Our projections were somewhat conservative in that they did not include any improvements to the LAT instrument performance from `Pass 8`.

8.4 Summary

The LAT has begun to push the boundaries of fundamental physics by opening a new window on the γ-ray universe. We have used the LAT to search for γ rays produced from dark matter annihilation in Galactic dark matter substructures, including dwarf spheroidal satellite galaxies and unassociated Galactic dark matter subhalos. No significant γ-ray signal was found to be consistent with dark matter annihilation in these Galactic targets, allowing us to set some of the most robust and stringent limits on the microscopic character of dark matter. The combined study of Milky Way dwarf galaxies represents the first time that γ rays have been used to directly constrain the thermal relic annihilation cross section. This result signals the start of an exciting new era where indirect searches are able to probe popular theoretically-motivated models of dark matter. Over the next decade, we expect the sensitivity of γ-ray searches for Galactic dark matter substructure to increase both from improvements to the LAT instrument performance and from an improved understanding of the Galactic environment. At the same time, direct dark matter detection experiments will take a large step forward with new ton-scale detectors and collider searches for new physics will benefit from upgrades to the Large Hadron Collider. Thus, we expect the next decade to be an exciting and pivotal time in the search for dark matter.

Appendix A

Pass 8: Toward a Full Realization of the LAT Scientific Potential[†]

A.1 Introduction

The current[1] LAT event-level analysis framework was largely developed before launch using Monte Carlo simulations through a series of iterations that, for historical reasons, are called `Passes`. `Pass 6` was released at launch and was followed in August 2011 by `Pass 7`, which mitigated the impact of some of the limitations of its predecessor [81].

Though the current simulation and reconstruction framework has enabled a great deal of science during the primary mission phase, on-orbit experience with the fully integrated detector has revealed some neglected and overlooked issues—primarily the effect of the instrumental pile-up (hereafter *ghost events* or *ghost signals*, see Ackermann *et al.* [81] for more details). Shortly after launch, opportunities for clear improvements were identified in the three main areas of the event-level analysis: (i)

[†] This chapter represents work done with the Fermi-LAT Collaboration and is published as Atwood *et al.* [201]. Special thanks to W. Atwood, A. Albert, L. Baldini, J. Bregeon, P. Bruel, E. Charles, J. Cohen-Tanugi, A. Franckowiak, T. Jogler, M. Pesce-Rollins, L. Rochester, C. Sgrò, M. Tinivella, T. Usher, M. Wood, and S. Zimmer.

[1] We use the word *current* to refer to the specific event-level analysis and associated event classes publicly available at the time of writing, i.e., `Pass 7` as detailed in Ackermann *et al.* [81].

Monte Carlo simulation of the detector, (ii) event reconstruction, and (iii) background rejection [202]. These improvements have the potential to greatly expand the LAT science capabilities and are now being deployed in the context of the `Pass-8` iteration of the LAT event-level analysis. Once developed, `Pass 8` will be used to process all high-level science data collected by the LAT and will be applied retroactively to all data collected during the primary mission phase.

A.2 Event Reconstruction

The event reconstruction currently represents the most developed area of the `Pass-8` project. This section reviews the main improvements that have been implemented at the reconstruction level for each of the three LAT subsystems: the tracker, the calorimeter, and the anti-coincidence detector (ACD).

A.2.1 Tracker Reconstruction

The conceptual framework for the current LAT tracker reconstruction software is that a photon converts into an electron-positron pair. Each member of the electron-positron pair can be followed through the energy deposits (or "hits") that it leaves in the silicon strip detectors of the tracker. The present tracker reconstruction software uses a track-by-track *combinatoric* pattern-recognition algorithm to find and fit the two tracks representing the electron-positron pair, and then combines them to form a vertex representing the photon conversion point.

This approach is problematic in four general areas. First, the track-finding algorithm needs an initial direction to start the procedure of track finding. To reduce the number of potential hit combinations, the track-finding algorithm uses the reconstructed calorimeter energy centroid and axis of energy flow to choose the initial hits. This makes the efficiency of the track finding dependent on the accuracy of the calorimeter reconstruction (a situation that is confounded by ghost signals in the calorimeter). Second, the track model includes multiple Coulomb scattering, which requires an estimate of the track energy, also derived from the calorimeter. Third, electrons and positrons interact readily in the material of the tracker (in particular the converter foils and silicon planes), creating an electro-magnetic shower that rarely resembles clean two-track events. Finally, large energy deposits in the calorimeter, particularly from high-energy photons far off-axis, often result in *backsplash*—upward-moving particles that deposit excess energy in the lower planes of the tracker. As the number of backsplash hits increases, the current track finding algorithm can become very inefficient, particularly if the initial position and direction estimates from the calorimeter are not accurate. For photons that convert in the back (lower part) of the tracker, where the real γ-ray track can contain as few as three hits in each orthogonal view, there is a large probability of losing the real signal among the background of spurious hits.

Features of the current track finding manifest themselves in the high-level instrument performance in three main ways: decreased efficiency due to a complete failure to reconstruct some events, decreased efficiency resulting from mislabeling good γ-ray events as background, and decreased angular resolution due to poor tracking.

Tree-based Tracking

The `Pass-8` tracker reconstruction addresses the issues discussed in the previous section by introducing a *global* approach to track finding, called tree-based tracking. Tree-based tracking approaches photon conversion in the tracker as the start of an electromagnetic shower and proceeds to link hits together into one or more tree-like networks. For each tree, the primary and secondary branches, defined as the two longest and straightest, represent the primary electron and positron trajectories (if unique) and sub-branches represent associated hits as the electron and positron radiate energy while traversing the tracker. Once the tree has been constructed, its axis can be found by calculating the moments of inertia of the associated hits, with the “mass” of each hit taken as a function of the length and straightness of its branch. The tree axis can then be used to associate the tree to energy deposited in the calorimeter, which allows an estimate of the total energy associated with the tree. Once an energy is available, up to two tracks are extracted and fit from the tree by associating the hits along the primary and secondary branches. As the tracks are extracted, they are each assigned half of the total energy attributed to the tree and are fit using a Kalman Filter technique [203]. The Kalman Filter accounts for multiple scattering but also allows for kinks which exceed deviations expected from multiple scattering. The resulting tracks incorporate the best information about the axis of the tree, and provide the best resolution on the direction of the photon.

Tests with Monte Carlo simulations and flight data show that the new tracker pattern recognition has the potential to significantly reduce the fraction of mis-tracked event and provide a 15–20% increase of the high-energy acceptance, with even larger improvement in the off-axis effective area, especially for photons converting in the lower part of the tracker. Additionally, the tree-based tracking is expected to significantly reduce the tails of the PSF at high energy.

Vertexing

If two tracks are extracted from a given tree an attempt is made to combine the two tracks into the vertex expected from pair conversion. The track association in the vertexing stage exploits both the distance of closest approach of the projected tracks (typically 1 mm or less for pair conversions) and the number of layers that separate the heads of the tracks (either 0 or 1). The track fitting yields not only track parameters, but also the associated errors (see Section A.5.3 for more details). Accordingly, when two tracks are combined to form a vertex, these errors are used to properly weight the contributions of each track. The resulting vertex generally yields the best information on the photon direction.

Since multiple Coulomb scattering scales as E^{-1}, the weights input to the vertexing (in the scattering-dominated regime) are proportional to the square of the assigned track energies. Unfortunately the LAT has a very limited ability to determine the individual track energies, since the calorimeter is usually unable to distinguish the energy deposits associated with each individual track. In the context of `Pass 8`, the strategy to determine the energy ordering of the tracks has been completely reworked and we anticipate that the improvement achieved over the current ordering scheme will be reflected in a better overall PSF.

A.2.2 Calorimeter Reconstruction

Similar to the tracker, the calorimeter reconstruction has been extensively revisited at all levels—including the crystal simulation (e.g., better modeling of the light collection), the energy and direction reconstruction, and the background-rejection algorithms.

Clustering

The single most radical change to the calorimeter reconstruction is the introduction of a multi-cluster architecture. The `Pass-6` and `Pass-7` event reconstruction treated the energy deposited in the calorimeter as a monolithic entity, with all hit crystals grouped together. In a low-occupancy environment, such as the one in which the LAT operates, this approach proved to be adequate to support science during the primary phase of the mission. However residual ghost signals that are spatially separated from the γ-ray shower can introduce substantial errors in the measurement of the energy, centroid, and direction of the shower itself. Since agreement between the tracker and the calorimeter is one of the main inputs to the background rejection, this results in a net loss of effective area from genuine γ-ray events misclassified as background.[2]

In `Pass 8` we have introduced a clustering stage in the calorimeter reconstruction aimed at identifying ghost signals and recovering the aforementioned loss in effective area. This presents some unique challenges, mostly connected with the fact that the LAT is designed to trigger on events over a huge field of view and therefore the calorimeter is seldom projective. We take advantage of the intrinsically three-dimensional calorimeter readout and exploit a Minimum Spanning Tree (MST)—a concept borrowed from graph theory with a long standing connection with clustering applications [204].

Tests performed on Monte Carlo simulations and flight data confirm the effectiveness of this approach and indicate a 5–10% increase in the effective area above $\sim 1\,\mathrm{GeV}$. Calorimeter clustering may have a much larger impact below a few hundred

---

[2] This loss was quantified and accounted for (but not recovered) in the generation of the post-launch IRFs, both in the `Pass-6` and `Pass-7` iterations.

MeV, where the energy in the ghost signal can be of the same order of magnitude or larger than that of the triggering γ ray.

Energy Reconstruction

The other crucial calorimeter-related development area is the energy reconstruction at very high energy. Above a few GeV, our primary energy reconstruction method is a three-dimensional profile fit to the energy in each layer of the calorimeter. This approach has proven to be nearly optimal up to $\sim 1\,\mathrm{TeV}$, where the average energy-deposited per crystal at the shower maximum starts to saturate the readout electronics.

In order to overcome saturation limitations, the profile fit has been extensively reworked by breaking up the layer contributions into individual crystal energies. Monte Carlo simulations indicate that the energy deposited in the saturated channels can be recovered to some extent by using the information from the nearby (non-saturated) crystals, achieving an energy resolution of $\lesssim 20\%$ for off-axis showers up to $\sim 3\,\mathrm{TeV}$ [80].

A.2.3 ACD Reconstruction

The ACD reconstruction has been fully re-written in the context of `Pass 8`. The first major improvement comes from the novel incorporation of calorimeter information when associating incident particle direction with energy deposition in the ACD. Directional information derived from calorimeter clusters is now propagated to the ACD in addition to tracks found in the tracker. This additional calorimeter information is particularly important for identifying background events at high energies or large incident angles, which are more susceptible to tracking errors (see Section A.2.1). In these cases, the calorimeter provides more robust directional information.

The second major improvement is to utilize event-by-event directional uncertainties when associating tracks and clusters with energy depositions in the ACD (Section A.5.3). Previously, the ACD reconstruction scaled the tracking uncertainty in an *ad hoc* manner based on an estimate of the total event energy. However, widely varying event topologies can lead to large differences in the quality of directional reconstruction for events of the same energy. Capturing this information in the event-by-event uncertainties provides substantially more information for background rejection.

The third major improvement comes from utilizing the fast ACD electronics designed for the LAT hardware trigger to mitigate the impact of ghost signals in the slower ACD pulse-height measurements. This improvement is especially important at low energies, where calorimeter backsplash is minimal and a small deposition of energy in the ACD can lead to the rejection of an event. The use of trigger information in the background rejection removes out-of-time signals from the ACD and can provide a $\sim 20\%$ increase in effective area below 100 MeV (see Appendix C for more details).

A.3 Event Selection

As the `Pass-8` event reconstruction is nears completion, the Fermi-LAT Collaboration is beginning to focus on event classification and background rejection. Following previous iterations of the event-level analysis, we use Classification Trees (CTs) to select candidate γ-rays on the basis of the reconstruction outputs. The particle classification CTs are trained using variables from all the three LAT subsystems. One noticeable difference is the use of the `TMVA` multivariate analysis framework [205]. Compared to the software used in the current event classification, `TMVA` is capable of handling much larger data sets and allows for an overall faster development cycle (see Appendix B for more details). The CT performance is evaluated from the combination of background rate and γ-ray acceptance that can be achieved for a given cut on the output signal probability. We note here that a differential background rate equal to or slightly lower than the extragalactic γ-ray background (EGB) rate is desirable for point-source analysis.

We have studied several candidate `Pass-8` event classes defined by event selections that allow varying levels of background contamination relative to the EGB. Each event class is composed of the following cuts: a selection on events with a reconstructed

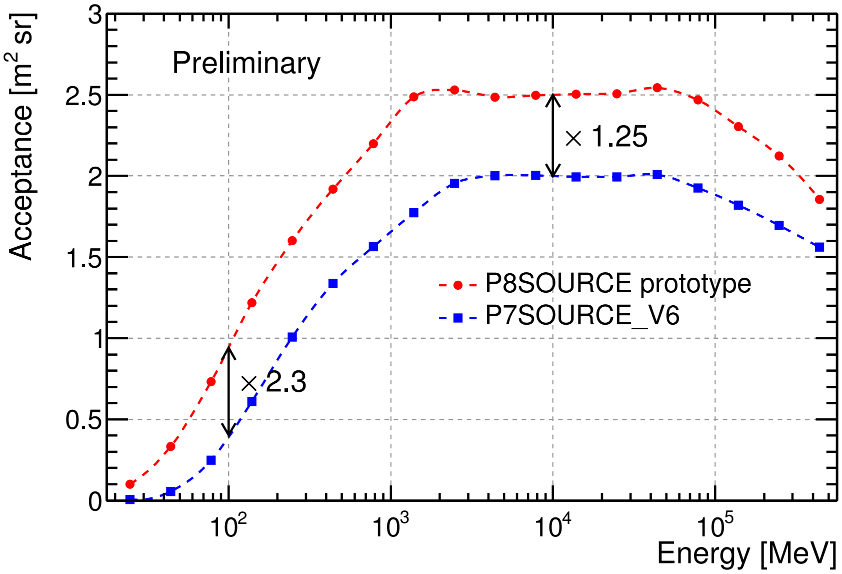

Figure A.1 Gamma-ray acceptance versus photon energy for the `Pass-7` source class and a candidate `Pass-8` event class.

track that deposits at least 5 MeV in the calorimeter, an ACD pre-selection on events for which the reconstructed track points to an activated section of the ACD, and an energy-dependent cut on CT variables for the particle type and the quality of the angular reconstruction. As shown in Figure A.1, at high energy we find a $\sim 25\%$ increase in acceptance relative to the `Pass-7` source event class while at low energies (below ~ 300 MeV) the increase in acceptance can be as high as a factor three.

A.4 Extended Event Classes

In the current photon analysis, events with no track in the tracker or depositing less than 5 MeV in the calorimeter are discarded from the standard event classes (some events are used in non-standard analyses such as the LAT Low-Energy technique (LLE) described in Pelassa *et al.* [206]). One of the areas of improvement which is being explored in the context of `Pass 8` is the development of extended photon classes, e.g. tracker-only and calorimeter-only events. Although these events have worse energy resolution and/or PSF with respect to those in the standard photon classes, they can provide a significant increase to the effective area in some regions of the LAT phase space.

A.4.1 Tracker-only Events

Below ~ 100 MeV many electron-positron pairs range out in the tracker and deposit no energy in the calorimeter. In the current event selection we require a minimum (5 MeV) energy deposit in the calorimeter, since agreement between the reconstructed direction of calorimeter clusters and tracker tracks is a powerful discriminator for well-reconstructed events and for hadronic background. However, the success of the LLE analysis for bright transients has made it clear that tracker-only events carry useful information that can be used in science analysis.

As the entire event selection process is being re-assessed in the context of `Pass 8`, tracker-only events provide the potential for a substantial increase in the effective area below 100 MeV, opening a new regime of LAT low-energy science.

A.4.2 Calorimeter-only Events

While almost a half of the events above ~ 50 GeV have no usable tracker information (either due to calorimeter conversion or due to mis-tracking),[3] at these energies the LAT calorimeter provides a directional capability at the level of a few degrees or better. Although the directional estimate of the calorimeter is much less precise than the typical tracker PSF, calorimeter-only events constitute a very promising event class for those analyses where the pointing accuracy is not critical. Preliminary studies show that calorimeter-only events might provide as much as ~ 30% increase in the high-energy acceptance, with an even larger enhancement of the effective area at large off-axis angles. The rejection of particle backgrounds in the absence of usable tracker information must still be investigated in detail and constitutes one of the main challenges connected with the use of calorimeter-only events.

---

[3] Technically, a significant fraction of calorimeter-only events would be discarded by the onboard filter; however, it is disengaged for events depositing more than 20 GeV in the calorimeter. At these energies shower leakage is such that the 20 GeV (of deposited energy) high-pass threshold translates into a smooth effective threshold of ~ 50 GeV, when measured in reconstructed energy.

A.4.3 Compton Events

Although the LAT was not designed as a Compton scattering telescope, it does have significant acceptance for Compton interactions—around $\sim 200\,\mathrm{cm}^2\,\mathrm{sr}$ at $\sim 5\,\mathrm{MeV}$ and $\sim 2000\,\mathrm{cm}^2\,\mathrm{sr}$ at $\sim 20\,\mathrm{MeV}$. Since the tungsten converters significantly degrade both the spatial and energy resolution for Compton interactions, extracting useful information involves selecting the events that are least affected by multiple scattering—such as front-converting events, or events which convert after the final tungsten layer and leave signals in the last three tracker layers. The significant power of the Compton events for measuring polarization makes this event class particularly interesting.

A.5 New Analysis Techniques

`Pass 8` will extend the scientific reach of the LAT in areas that are simply not accessible in the current event-level analysis. The new event reconstruction and selection are being designed with these scientific targets in mind and therefore in this section we provide a few illustrative examples.

A.5.1 Multi-photon Events

One of the most striking aspects of the LAT capability compared to prior missions is its high *shutter speed*. When viewed as a camera, the LAT has a shutter speed approximately equal to its trigger window width ($\sim 600\,\mathrm{ns}$) and a frame advance time set by the readout dead time ($\sim 26.5\,\mu\mathrm{s}$). When this is considered in combination with its large effective area the possibility of recording simultaneous photons becomes tantalizing. It was suggested long before launch that some astrophysical sources could produce coherent bunches of high-energy γ rays [207]. In addition, extraordinarily bright bursts (e.g., from black-hole evaporation) could also result in multi-photon events [208]. However, searches for such exotic events are not possible with the current reconstruction algorithms. The lack of calorimeter clustering along with a background rejection tuned on single-photon events almost completely eliminate any efficiency the LAT might have to see such events. With the re-write of the LAT event-level analysis currently underway, both of these deficiencies are being addressed. The combination of the new calorimeter clustering algorithm and the more robust tree-based tracking will enable a search for multi-photon events. The Monte Carlo generator has been reworked to produce multi-photon events, which is an important step towards designing and testing this novel analysis technique.

A.5.2 Polarization Measurements

The idea of using the azimuthal distribution of the electron-positron opening plane to perform γ-ray polarimetry in the pair-production regime dates back more than 60 years and has been a topic of extensive theoretical study [209]. The primary limitation is that fully polarized radiation yields only a small (10–20%) overall modulation in the electron-positron opening plane. Additionally, in a typical pair-conversion telescope this modulation is strongly suppressed (exponentially with the converter thickness) due to multiple Coulomb scattering.

The LAT is much more sensitive to polarization than any of its predecessors due to its excellent hit resolution and large effective area . The LAT polarimetric capabilities are being investigated in detail in the context of `Pass 8`—particularly in conjunction with the possibility of using γ-ray conversions in the silicon detectors to limit the effect of multiple scattering. Preliminary studies indicate that the LAT might be sensitive to linear polarization of the strongest γ-ray sources.

A.5.3 Event-by-event Errors

The image resolution of the LAT is strongly energy-dependent: the PSF improves roughly as $E^{-0.8}$ in the multiple-scattering regime (i.e., below $\sim 10\,\mathrm{GeV}$). Other factors also influence the image resolution, namely the conversion point in the tracker and the incident angle.

The current IRFs average over various event topologies to capture some of these effects. However, the track reconstruction software provides a full treatment of directional errors in the form of an event-by-event covariance matrix constructed from the hit composition and the material crossed by the initial electron and positron tracks.

For example, if a track is missing an early hit due to the transversal of a gap between silicon sensors, the PSF associated with this individual event is degraded by up to a factor of two. In addition, the current IRF formalism assumes the error for each event is circular on the sky, an assumption which becomes increasing inaccurate far off axis where the real photon error is highly elliptical.

`Pass 8` will make the full event-by-event covariant information available in a form that can be readily used for science analysis. Individual event-by-event errors will be key for source localization (especially for short transients) and for the study of individual extended sources. The utilization of the event-by-event errors for large-area or long-duration observations may prove computationally infeasible; however, it should be possible to approximate the event-by-event errors by binning events based on the size of their covarient error ellipses.

A.6 Conclusions

`Pass 8` will come close to realizing the full scientific potential of the LAT. It will incorporate the knowledge gained from the primary phase of the mission and complete the development process that was time-limited prior to launch. The basic ingredients of the new event simulation and reconstruction are in place, and the reprocessing of LAT data from the primary mission phase has already begun. New background rejection and event classification analyses are now being developed. We anticipate `Pass 8` will begin to be tested on real science analyses at the end of 2013.

We anticipate that many of the performance improvements will benefit all LAT science analyses. Specifically, we anticipate larger acceptance, better high-energy PSF, lower backgrounds, and better control over systematic uncertainties. The new event reconstruction will allow us to extend the energy reach of the LAT both below 100 MeV and above 1 TeV. The extended event classes will provide significant enhancements in the acceptance for specific analyses. Finally, `Pass 8` will allow for new science topics which are precluded by the current event-level analysis, such as the search for multi-photon events and γ-ray polarization measurements.

Appendix B

TMine: A Tool for Multivariate Event Classification[†]

B.1 Introduction

The LAT operates in a low Earth orbit, where thousands of particles trigger the detector every second. After on-board filtering, the recorded data from these triggers are transmitted to the ground and undergo full event reconstruction. The final stage of LAT reconstruction is the event analysis, which combines information from each detector subsystem (the anticoincidence detector, tracker, and calorimeter) to create a picture of the event as a whole. From the event picture, high-level science variables (i.e., event energy and incident direction) are assigned. The event analysis must also address the challenging task of separating the desired γ-ray signal events from charged particle backgrounds [39].

The assignment of fundamental quantities such as particle type, energy, and incident direction is a complex task, since the LAT accepts particles over a wide range in parameter space (both in energy and incident angle) and event topology (close to detector edges and gaps). In addition, discrimination against background at a level of 1 part in 10^6 is required to fulfill the LAT science goals. Classic cut-based analyses

---

[†] This chapter represents work done with the Fermi-LAT Collaboration and is published as Drlica-Wagner and Charles [210]. Special thanks to Eric Charles.

lack sufficient accuracy and signal efficiency to meet these goals. To achieve the required instrument performance, the LAT event analysis applies classic cuts followed by multivariate classification trees [211].

Classification trees (and decision trees in general) belong to the larger family of data mining and machine learning algorithms [82]. Classification in the context of machine learning focuses on associating an observation to a sub-population based on the traits present in a set of training observations (where the true sub-population is known). Training of classification trees is performed through binary recursive partitioning, an algorithm that develops a set of logical cuts by iteratively splitting the training data to maximize the separation of the true sub-populations. For the LAT event analysis, the training of classification trees is performed on sets of γ-ray and cosmic-ray events generated from Monte Carlo simulation of the LAT detector. These logical cuts are trained on variables describing the physical character of an event shower (e.g., the transverse shower size in the calorimeter, the number of excess hits surrounding the primary particle track, etc.), while the output is a classification of the event (e.g., the type of particle, the quality of direction reconstruction, etc.).

We introduce `TMine`, a new tool for implementing both cut-based and multivariate classification algorithms. The goal of `TMine` is to enhance the event level analysis to improve the performance of the LAT instrument (i.e., effective area, energy resolution, and point spread function). Additionally, `TMine` has been used for studying LAT charged particle events (electrons, positrons, and protons) and for the classification of unassociated LAT γ-ray sources.

B.2 The TMine Analysis Tool

`TMine` is an interactive software tool for developing and processing complex event classification analyses. `TMine` is based on `ROOT` [212], the de-facto data analysis framework for current high energy physics experiments. In particular, `TMine` uses the data indexing and linking functionality of `ROOT` to associate newly calculated variables with pre-existing quantities and keep only the minimal set of information necessary for data processing. Thus, `TMine` handles large data sets in a quick and efficient manner,

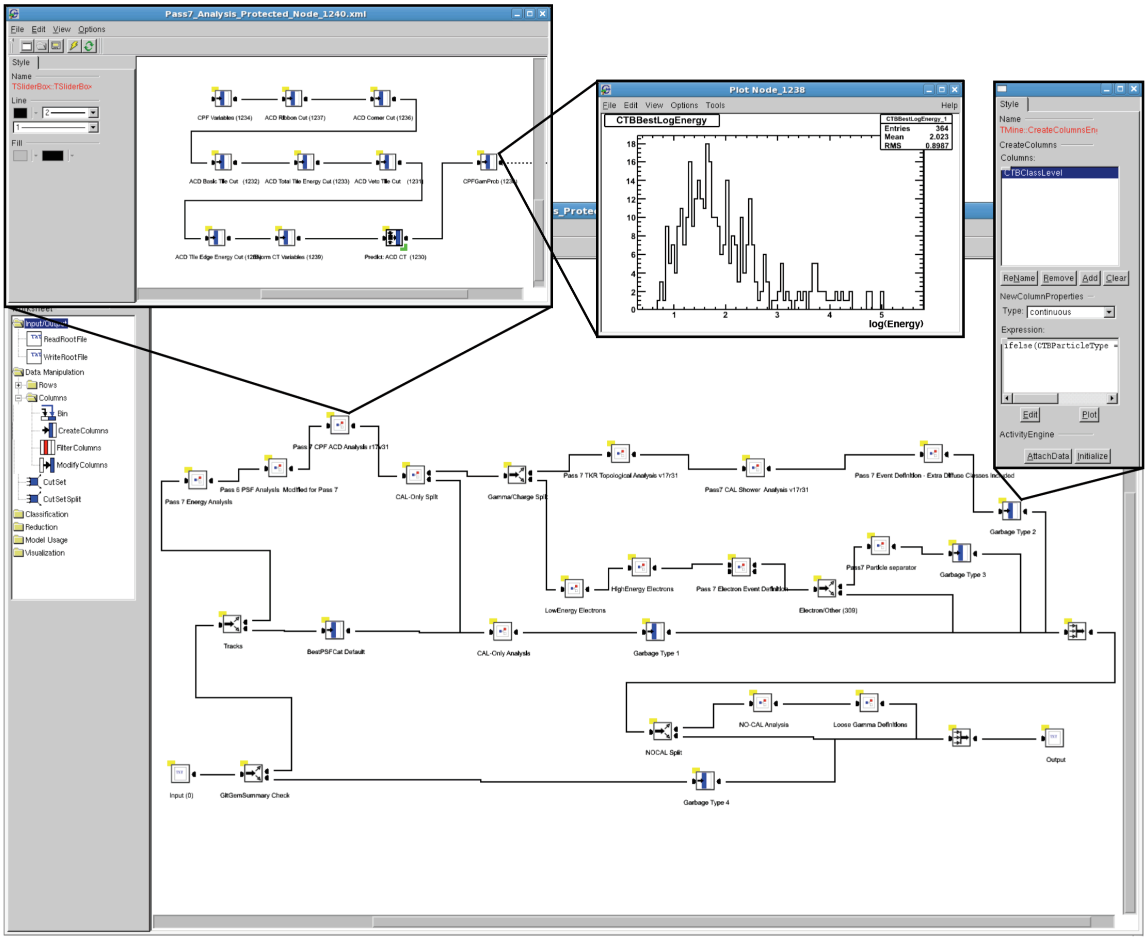

Figure B.1 The `Pass-7` iteration of the LAT event analysis as viewed by `TMine`. Many nodes contain sub-analyses (inset top left), while the functionality of each node can be plotted (inset top middle) and edited through a GUI editor (inset top right). A `TMine` analysis can combine classical cut-based selections with multivariate classification.

especially when some variables are only defined for a small subset of the events.

`TMine` applies classic event-selection cuts in the standard `ROOT` manner through `TFormulas`, `TCuts`, and event indexing. For the processing and parallel evaluation of sophisticated multivariate classification algorithms, `TMine` utilizes the `ROOT` Toolkit for Multivariate Analysis (`TMVA`) [205]. Through `TMVA`, `TMine` has access to many multivariate classification algorithms including, but not limited to, boosted decision trees and artificial neural networks. While the command-line functionality of `ROOT` is preserved, the graphical user interface of `TMine` allows the user to harness the power of `ROOT` and `TMVA` in a visual work environment. `TMine` was specifically designed to address problems faced in high energy physics, though it need not be restricted to these.

A `TMine` analysis consists of a network of directionally linked nodes controlling work flow and operation (Figure B.1). Nodes both alter event characteristics (i.e., variable definition, assignment, and selection) and direct events through the network. Specialized nodes are used for training, testing, and implementing `TMVA` classification algorithms. Using the machinery of `ROOT`, `TMine` is able to split, manipulate, and recombine large quantities of data without excessive duplication of information. Structuring the event analysis in a visual manner has been found to be conceptually powerful when designing the LAT event analysis [39].

B.3 Applications of TMine

B.3.1 The Pass-8 Reconstruction Effort

The primary application of `TMine` is in the development and implementation of the `Pass-8` event analysis (Appendix A). The `Pass-8` effort is a complete reworking of the LAT simulation and reconstruction software, benefiting from the analysis of flight data (which was unavailable before launch). `TMine` will improve the interface between event reconstruction and event classification. It also provides improvements to the structure and validation of the `Pass-8` event analysis. `TMine` has built-in functionality for comparing real and simulated data (Figure B.2), an essential step prior to training multivariate classification algorithms. Additionally, the `TMine` interface to `TMVA` allows for the training of multivariate classification algorithms using larger data sets than was possible with the software tools previously used by the Fermi-LAT Collaboration.

B.3.2 LAT Charged-Particle Analyses

In addition to the `Pass-8` effort, `TMine` has been utilized for a variety of scientific analyses. Since electromagnetic showers are common to photon, electron, and positron

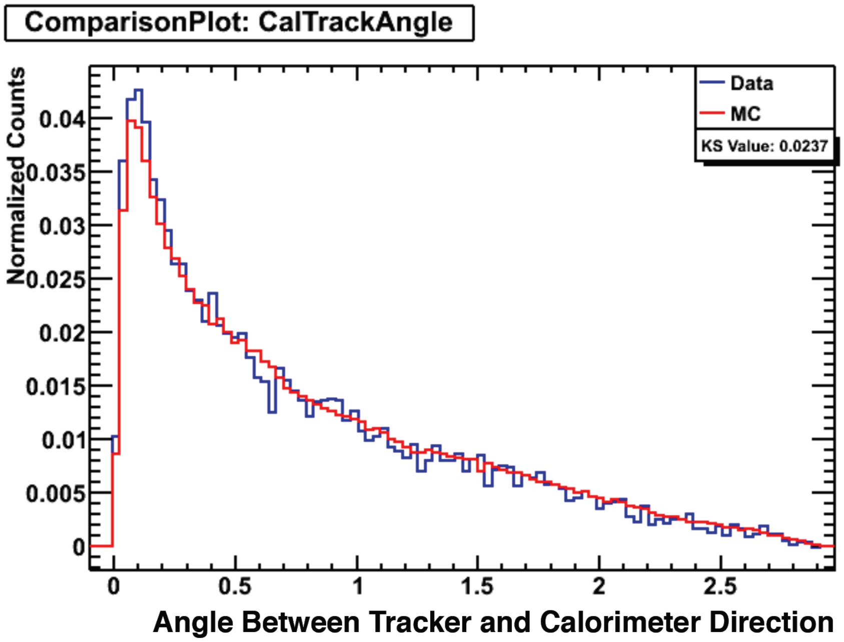

Figure B.2 Comparisons between a statistical sample of photons from flight data (blue) and simulations (red). Only variables with good agreement should be used for classification.

events, the LAT is naturally sensitive to cosmic-ray electrons and positrons [213–215]. For the majority of LAT analyses, these charged particles present a background for γ-ray science. Thus, the study of electrons and positrons requires a non-standard event analysis and a reprocessing of the LAT data (the analysis of electrons and positrons has subsequently been appended to the standard event analysis). `TMine` was used for this reprocessing because it is a stand-alone program that is free from the overhead of the full LAT reconstruction software.

A similar effort is underway to study cosmic-ray proton events in more detail [216]. For this task, `TMine` was used both to design a proton event classification and to reprocess LAT data. The analysis of proton events presents an excellent example of how `TMine` can be used for event classification. Figure B.3 shows a simple event analysis for distinguishing hadrons from leptons. This worksheet is read from left to right, with the training data set input on the left and the predicted particle type output on the right. A classical cut selecting charged particles is applied first, followed

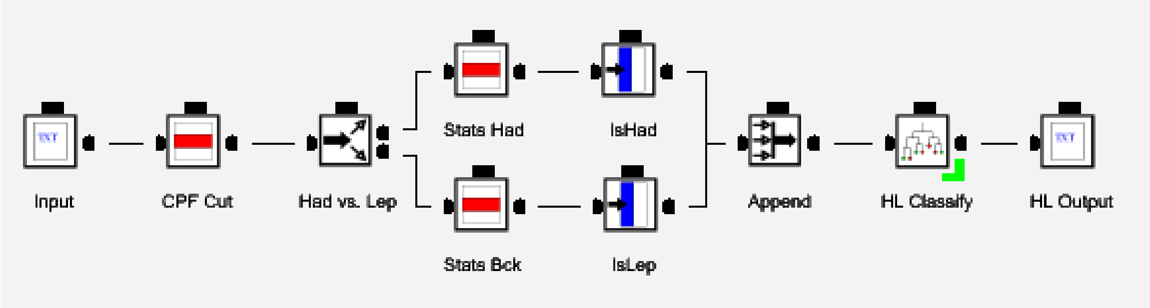

Figure B.3 A simple `TMine` worksheet for discriminating cosmic-ray hadron events from cosmic-ray lepton events. Data is input on the left, has a classical charged particle cut applied, and is used to train a `TMVA` classifier.

by a split and tagging of the true particle type. Events are then recombined and used to train `TMVA` boosted decision trees. The preliminary performance of this classifier when discriminating simulated hadrons from simulated electrons and positrons is shown in Figure B.4.

B.3.3 Classifying Unassociated LAT Sources

While `TMine` was originally developed for use with the LAT event analysis, it is not limited to that purpose. Notably, `TMine` has been utilized to classify unassociated γ-ray sources [174]. Of the 1451 γ-ray sources in the First LAT Source Catalog (1FGL) [87], 630 are unassociated with counterparts in other wavelengths. In an attempt to classify these sources, `TMine` was used to input individual source characteristics, such as spectral index, spectral curvature, and fractional variability into a forest of `TMVA` boosted decision trees. These input variables were selected to be independent of source flux, location, or significance, since these distributions differ between associated and unassociated sources. The `TMVA` decision trees were trained on the set of 1FGL sources already associated with active galactic nuclei (AGN) and pulsars. The output of this analysis was a predictor representing the probability that a source is an AGN versus a pulsar.

Unassociated sources were separated into AGN candidates and pulsar candidates by cutting on the output of the classifier. This cut was designed to have 80% efficiency

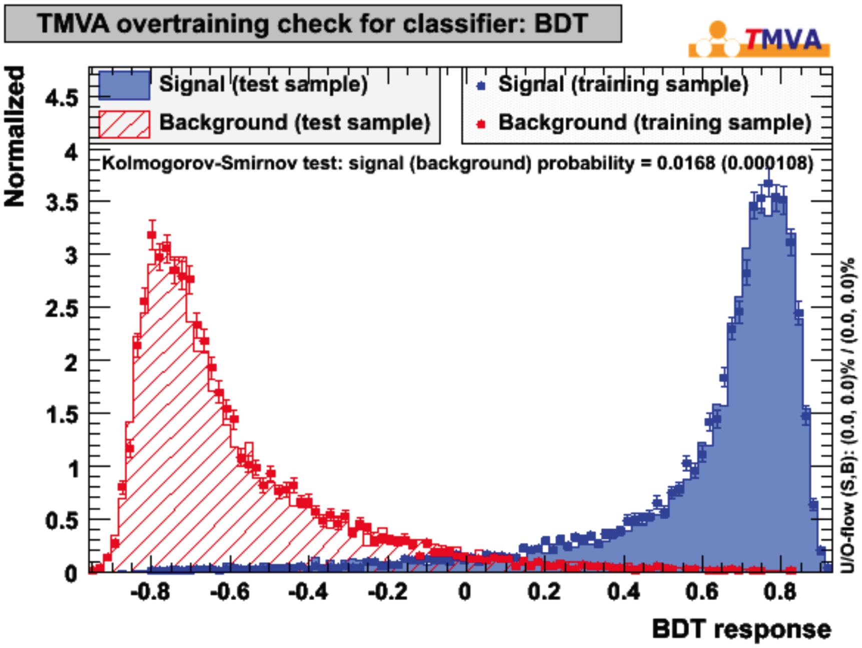

Figure B.4 Classifier output from the `TMine` implementation of a `TMVA` boosted decision tree. Simulated hadrons (marked signal) are distinguished from simulated electrons and positrons (marked background). Events that are hadron-like are assigned positive predictor values, while events that are lepton-like are assigned negative values. The two event classes are well separated, and an independent sample of test events (filled histograms) agrees with the distribution of events used to train the classifier (data points).

when applied to an independent set of sources associated to AGN and pulsars in the 1FGL. The Galactic latitude of the unassociated sources was explicitly omitted from the classifier training, but the spatial distribution of candidate AGN was found to be isotropically distributed, while the pulsar candidates were distributed along the Galactic plane (Figure B.5). From follow-up observations on a subset of the unassociated sources, the cut placed on the multivariate classifier is found to be $\sim 70\%$ efficient with a contamination of $\sim 5\%$ for both AGN and pulsars [174].

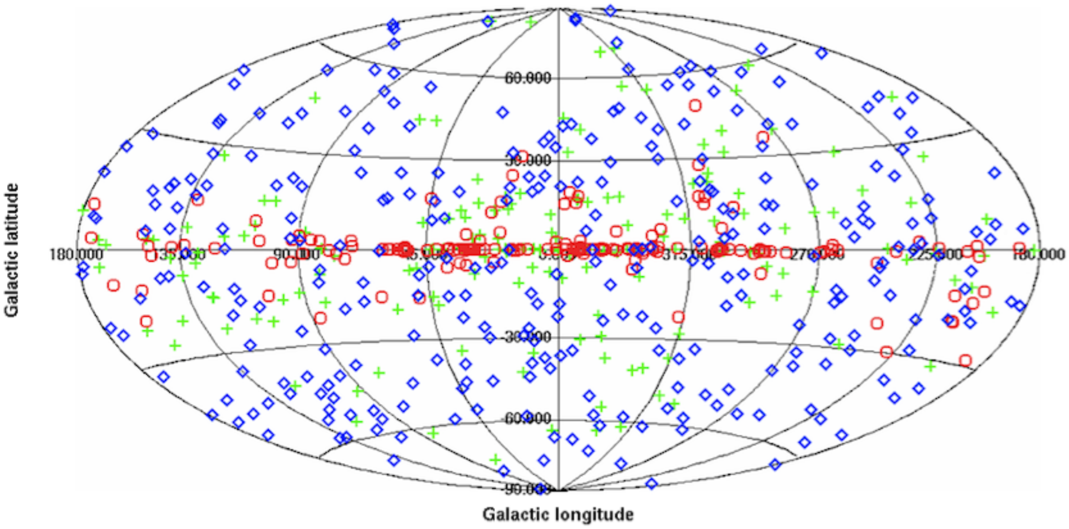

Figure B.5 Spatial distribution, in Galactic coordinates, for 1FGL unassociated sources classified as AGN candidates (blue diamonds) and pulsar candidates (red circles). As expected, pulsar candidates are distributed primarily along the Galactic plane, while AGN candidates are distributed isotropically. The sources left unclassified are shown as green crosses.

B.4 Conclusions

We present `TMine`, a new tool for developing and processing complex classification tasks. `TMine` is a `ROOT`-based tool utilizing the multivariate classification package, `TMVA`. While the primary application of `TMine` is to the LAT event analyses (specifically the `Pass-8` iteration), it has a wide range of possible applications.

Appendix C

Correcting for Pile-up in the LAT Anticoincidence Detector[†]

C.1 Introduction

The pre-launch LAT simulation and reconstruction software has performed admirably, allowing for extensive scientific analysis. However, the unexpected presence of particle pile-up, remnant detector response to particles that are nearly contemporaneous with the triggered event (Figure C.1), has had a negative impact on the LAT performance. These pile-up (or "ghost") particles affect all LAT subsystems, leading to an overall degradation in signal efficiency and background rejection power. In the LAT anticoincidence detector (ACD), ghosts are manifested as out-of-time depositions of energy in the scintillating fiber tiles and ribbons. As part of the `Pass-8` effort (Appendix A), we have developed a technique to utilize information from the ACD fast hardware trigger, rather than from the slower analog electronics, to identify and mitigate the effect of ghosts in the ACD and improve γ-ray selection efficiency.

[†] This chapter represents work done with the Fermi-LAT Collaboration. Special thanks to Eric Charles and Melissa Pesce-Rollins.

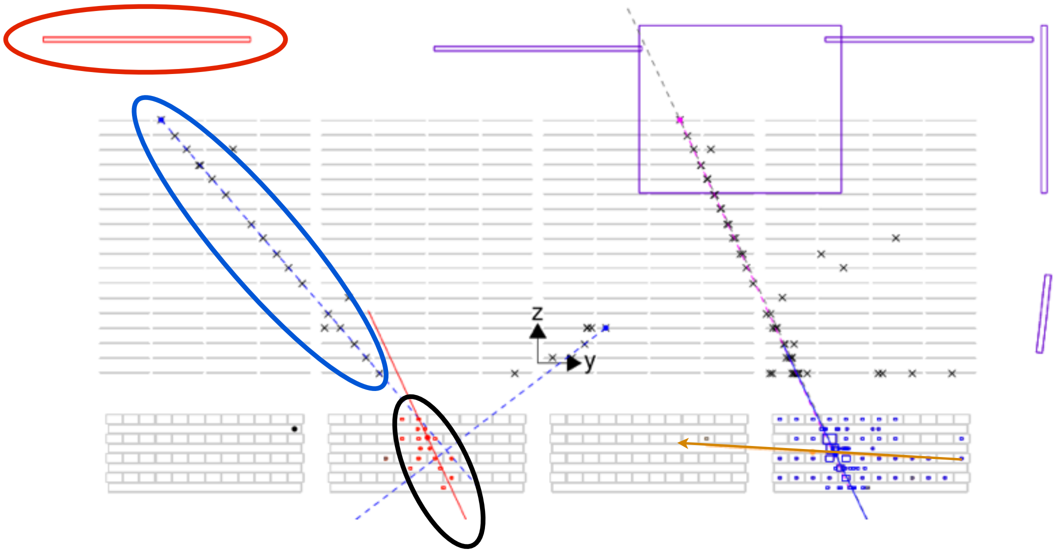

Figure C.1 LAT event display of a good γ-ray event (right) accompanied by an out-of-time ghost event (left). Pile-up energy is deposited as an extra calorimeter cluster (black ellipse), an extra track in the tracker (blue ellipse), and an additional hit in the ACD (red ellipse). Additionally, with a monolithic treatment of the calorimeter, the ghost energy skews the direction of the calorimeter axis (gold arrow). Together, these ghosts signals lead to the rejection of otherwise well-reconstructed γ rays.

C.2 The Anticoincidence Detector (ACD)

The ACD is responsible for providing 0.9997% rejection power for singly charged particles entering the top or sides of the LAT [78]. At the same time, the ACD must avoid self-vetoes from the backsplash of energetic γ rays. To achieve these goals, the ACD has two sets of electronic readouts: (1) a fast discriminator based on the output voltage threshold, which is used in the hardware trigger, and (2) a slower and more accurate pulse height analysis (PHA), which is used in software reconstruction After launch it was discovered that pile-up from out-of-time events and solar flares was contaminating the PHA signals and leading to the false rejection of γ-ray events [81].

C.3 Pile-up Effects

Events that arrive nearly contemporaneously with the triggered event can leave residual energy in the detector (Figure C.1). Some common examples are: (1) hits in the tiles and ribbons of the ACD, (2) hits in the silicon strips of the tracker, and (3) energy deposition in the calorimeter. This ghost energy confounds the event reconstruction algorithms, leading to the rejection of otherwise good γ-ray events. This decrease in efficiency is largest at low energy where ghost signals make up a significant fraction of the total event energy. The slower shaping electronics of the ACD are especially susceptible to ghost pile-up

X-rays can also deposit energy in the scintillating fibers of the ACD tiles and ribbons. Under normal circumstances, X-rays represent a negligible below-threshold background for the ACD electronics. However, during energetic solar flares, a high flux of keV X-rays can bombard the LAT instrument, depositing an appreciable amount of energy in the large scintillating tiles at the base of the ACD. Because of the slow rise time of the PHA electronics, the energy deposited by X-rays can gradually accumulate without triggering the fast discriminator veto. Since the high-purity photon classification currently rely on the PHA energy readout alone, X-ray pile-up can lead to the rejection of good γ-ray events. For some solar flares this effect can lead to a drastic decrease in γ-ray-class event rates (Figure C.4).

C.4 Mitigating Pile-up Effects in the ACD

The ACD PHA electronics provide a measure of the energy deposited in an ACD element scaled to the deposition of a single minimally ionizing particle (MIP). The PHA electronics have two primary disadvantages: (1) they have a slow return to baseline and can remain active between events, and (2) they have a slow rise time, so low-energy X-rays can slowly accumulate to a large signal. On the other hand, the ACD fast discriminator ("trigger") electronics return a simple veto when the channel voltage exceeds a threshold value (0.45 MIP or ~ 25 photo-electrons). While the trigger electronics provide no additional information about the amount of energy

Table C.1. ACD pile-up mitigation scheme.

	Trigger Veto = True	Trigger Veto = False
PHA $> 0.45\,\mathrm{MIP}$	In-Time	Out-of-Time
PHA $< 0.45\,\mathrm{MIP}$	—	Ambiguous

deposited in an ACD element, they have the advantages that: (1) they have a fast rise time and return to baseline, and (2) it is unlikely that the trigger will be activated by out-of-time event. Thus, requiring that the fast discriminator fires (a "trigger veto") should provide a mechanism for eliminating ACD pile-up.

As can be seen from Table C.1, there are three classes of hits: (1) in-time hits possessing an above-threshold PHA signal and a trigger veto, (2) out-of-time hits possessing an above-threshold PHA signal but lacking a trigger veto, and (3) ambiguous hits which are below the trigger threshold. To investigate how the use of the trigger information can impact the ACD cumulative energy determination, we define 3 different ACD cumulative energy quantities: (1) the "Total Energy" includes all ACD hits, (2) the "Cleaned Energy" removes hits that are above the trigger threshold but lack a veto, and (3) the "Trigger Energy" removes all hits that do not possess a trigger veto. The impact of these ACD energy estimators is shown for in-time and out-of-time event samples in Figure C.2. By using the "Trigger Energy" it is possible to remove $\sim 95\%$ of the out-of-time hits while negligibly impacting in-time hits.

C.5 Improvements to the Gamma-ray Acceptance

C.5.1 Low-Energy Gamma-ray Efficiency

Because of imperfect tracking, it is not always possible to correctly determine which ACD hit is associated with the entry point of a charged particle. This becomes

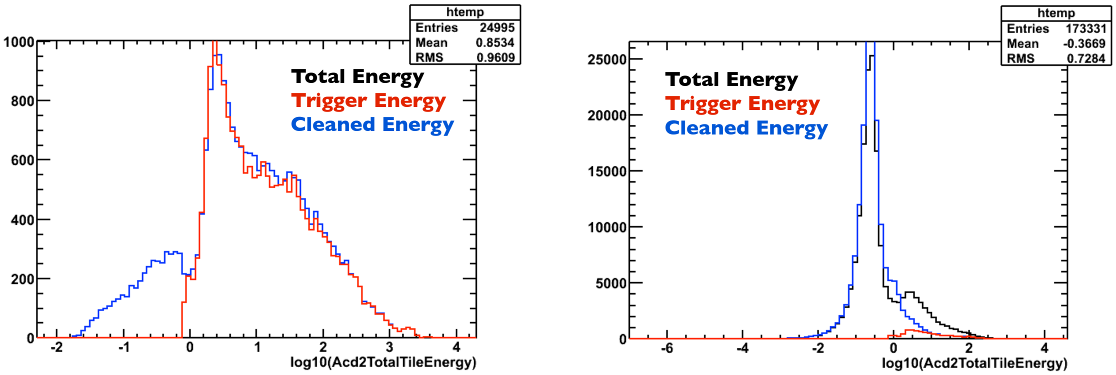

Figure C.2 Three different measurements of the cumulative ACD energy calculated for in-time Monte Carlo background events (left) and out-of-time periodic triggers (right). The "Total Energy" contains all hits (including pile-up), the "Cleaned Energy" removes high-energy hits without a trigger veto, and the "Trigger Energy" removes all events without a trigger veto. It can be seen that by requiring a trigger veto, it is possible to drastically reduces the energy contribution of out-of-time events while minimally impacting in-time events.

especially problematic at low-energy where Coulomb scattering leads to inaccurate direction reconstruction. To reject mis-tracked charged particles, a cut is applied on the ratio of the energy deposited in the ACD to the total event energy. As discussed in Section C.4, the current estimate of the total ACD energy contains large contributions from out-of-time pile-up. The added pile-up energy leads to the incorrect rejection of otherwise clean γ rays and a reduction of the low energy γ-ray efficiency. By instead using only the energy associated with hits possessing trigger vetoes, it is possible to improve the ACD γ-ray selection efficiency by $\sim 20\%$ below 100 MeV (Figure C.3).

C.5.2 Gamma-ray Rate During Solar Flares

Energy from X-rays emitted during solar flares accumulates in the ACD causing the rejection of γ-ray events. Using the ACD total energy leads to periods of 10 to 30 minutes coincident with solar flare where the LAT is effectively blind. By instead calculating the ACD energy from only hits possessing a trigger veto, it is possible to completely restore the γ-ray efficiency during these time periods (Figure C.4).

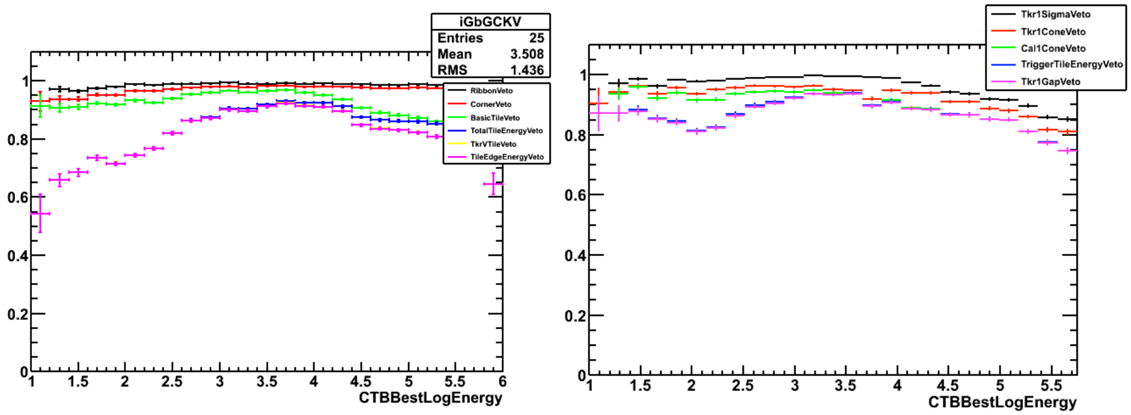

Figure C.3 Gamma-ray selection efficiency after various stages of the ACD background rejection for the `Pass-7` (left) and preliminary `Pass-8` (right) event analyses. The mitigation of ACD pile-up leads to a $\sim 20\%$ increase in acceptance at low energy.

C.6 Conclusions

By using information from the fast ACD descriminator electronics, we have successfully mitigate the impact of out-of-time pile-up in the ACD. We have shown that by incorporating trigger veto information, it is possible to increase the γ-ray efficincy below 100 MeV and to restore the γ-ray acceptance during solar flares. Mitigating pile-up in the ACD is just one small piece of the `Pass-8` effort, which promises substantial improvements to the LAT instrument performance in the years to come.

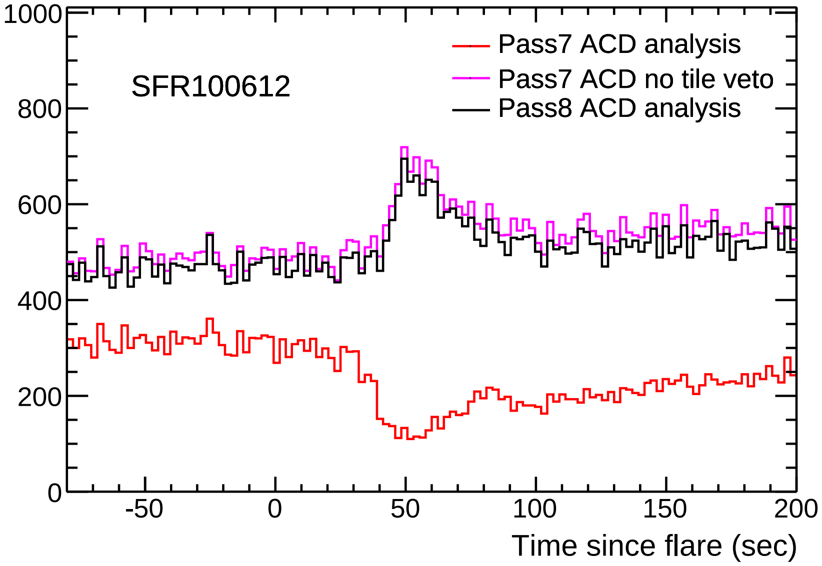

Figure C.4 Pile-up from solar flare X-rays leads to a drop in the transient event rate (red). By requiring an ACD trigger (purple) this rate can be restored. The preliminary `Pass-8` ACD analysis (black) no longer suffers from X-ray pile-up.

References

[1] M. Davis, G. Efstathiou, C. S. Frenk, and S. D. White, ApJ **292**, 371 (1985).

[2] M. Tegmark *et al.* (SDSS Collaboration), ApJ **606**, 702 (2004), arXiv:astro-ph/0310725 [astro-ph].

[3] W. J. Percival *et al.* (SDSS Collaboration), MNRAS. **401**, 2148 (2010), arXiv:0907.1660 [astro-ph.CO].

[4] G. F. Smoot, C. Bennett, A. Kogut, E. Wright, J. Aymon, *et al.*, ApJ **396**, L1 (1992).

[5] D. Spergel *et al.* (WMAP Collaboration), ApJS **148**, 175 (2003), arXiv:astro-ph/0302209 [astro-ph].

[6] P. Ade *et al.* (Planck Collaboration), (2013), arXiv:1303.5076 [astro-ph.CO].

[7] F. Zwicky, Helv.Phys.Acta **6**, 110 (1933).

[8] S. Allen, R. Schmidt, H. Ebeling, A. Fabian, and L. van Speybroeck, MNRAS **353**, 457 (2004), arXiv:astro-ph/0405340 [astro-ph].

[9] A. Vikhlinin, A. Kravtsov, W. Forman, C. Jones, M. Markevitch, *et al.*, ApJ **640**, 691 (2006), arXiv:astro-ph/0507092 [astro-ph].

[10] V. C. Rubin and J. Ford, W. Kent, ApJ **159**, 379 (1970).

[11] L. E. Strigari, J. S. Bullock, M. Kaplinghat, J. D. Simon, M. Geha, *et al.*, Nature **454**, 1096 (2008), arXiv:0808.3772 [astro-ph].

[12] J. Diemand, M. Kuhlen, P. Madau, M. Zemp, B. Moore, *et al.*, Nature **454**, 735 (2008), arXiv:0805.1244 [astro-ph].

[13] V. Springel, J. Wang, M. Vogelsberger, A. Ludlow, A. Jenkins, *et al.*, MNRAS. **391**, 1685 (2008), arXiv:0809.0898 [astro-ph].

[14] B. Paczynski, ApJ **304**, 1 (1986).

[15] C. Alcock *et al.* (MACHO Collaboration), ApJ **542**, 281 (2000), arXiv:astro-ph/0001272 [astro-ph].

[16] M. Milgrom, ApJ **270**, 365 (1983).

[17] D. Clowe, M. Bradac, A. H. Gonzalez, M. Markevitch, S. W. Randall, *et al.*, ApJ **648**, L109 (2006), arXiv:astro-ph/0608407 [astro-ph].

[18] M. Bradac, S. W. Allen, T. Treu, H. Ebeling, R. Massey, *et al.*, ApJ **687**, 959 (2008), arXiv:0806.2320 [astro-ph].

[19] R. Peccei and H. R. Quinn, Phys.Rev.Lett. **38**, 1440 (1977).

[20] A. Kusenko, Phys.Rept. **481**, 1 (2009), arXiv:0906.2968 [hep-ph].

[21] S. P. Martin, in *Perspectives on Supersymmetry II*, edited by G. L. Kane (World Scientific, 1998) pp. 1–153, arXiv:hep-ph/9709356 [hep-ph].

[22] E. W. Kolb and M. S. Turner, *The Early Universe*, Frontiers in Physics, Vol. 69 (Westview Press, 1990).

[23] G. Jungman, M. Kamionkowski, and K. Griest, Phys. Rep. **267**, 195 (1996), arXiv:hep-ph/9506380 [hep-ph].

[24] G. Aad *et al.* (ATLAS Collaboration), Phys.Lett. **B716**, 1 (2012), arXiv:1207.7214 [hep-ex].

[25] S. Chatrchyan *et al.* (CMS Collaboration), Phys.Lett. **B716**, 30 (2012), arXiv:1207.7235 [hep-ex].

[26] M. W. Goodman and E. Witten, Phys.Rev. **D31**, 3059 (1985).

[27] Z. Ahmed *et al.* (CDMS-II Collaboration), Science **327**, 1619 (2010), arXiv:0912.3592 [astro-ph.CO].

[28] E. Aprile *et al.* (XENON100 Collaboration), Phys.Rev.Lett. **109**, 181301 (2012), arXiv:1207.5988 [astro-ph.CO].

[29] E. A. Baltz, M. Battaglia, M. E. Peskin, and T. Wizansky, Phys.Rev. **D74**, 103521 (2006), arXiv:hep-ph/0602187 [hep-ph].

[30] G. Aad *et al.* (ATLAS Collaboration), JINST **3**, S08003 (2008).

[31] S. Chatrchyan *et al.* (CMS Collaboration), JINST **3**, S08004 (2008).

[32] J. Gunn, B. Lee, I. Lerche, D. Schramm, and G. Steigman, ApJ **223**, 1015 (1978).

[33] F. Stecker, ApJ **223**, 1032 (1978).

[34] L. Bergstrom and H. Snellman, Phys.Rev. **D37**, 3737 (1988).

[35] L. Bergstrom, P. Ullio, and J. H. Buckley, Astropart. Phys. **9**, 137 (1998), arXiv:astro-ph/9712318 [astro-ph].

[36] L. Watkins, N. Evans, and J. An, MNRAS **406**, 264 (2010), arXiv:1002.4565 [astro-ph.GA].

[37] A. W. McConnachie, AJ **144**, 1 (2012), arXiv:1204.1562 [astro-ph.CO].

[38] M. Boylan-Kolchin, J. S. Bullock, and M. Kaplinghat, MNRAS **415**, L40 (2011), arXiv:1103.0007 [astro-ph.CO].

[39] W. Atwood *et al.* (Fermi-LAT Collaboration), ApJ **697**, 1071 (2009), arXiv:0902.1089 [astro-ph.IM].

[40] T. Weekes, H. Badran, S. Biller, I. Bond, S. Bradbury, *et al.*, Astropart. Phys. **17**, 221 (2002), arXiv:astro-ph/0108478 [astro-ph].

[41] J. Hinton (HESS Collaboration), New Astron.Rev. **48**, 331 (2004), arXiv:astro-ph/0403052 [astro-ph].

[42] E. Lorenz (MAGIC Collaboration), New Astron.Rev. **48**, 339 (2004).

[43] G. F. Bignami *et al.*, Space Sci. Inst. **1**, 245 (1975).

[44] C. E. Fichtel *et al.*, ApJ **198**, 163 (1975).

[45] D. Thompson, D. Bertsch, C. Fichtel, R. Hartman, R. Hofstadter, *et al.*, ApJS **86**, 629 (1993).

[46] M. Tavani *et al.* (AGILE Collaboration), A&A **502**, 995 (2009), arXiv:0807.4254 [astro-ph].

[47] X. Xue *et al.* (SDSS Collaboration), ApJ **684**, 1143 (2008), arXiv:0801.1232 [astro-ph].

[48] R. Catena and P. Ullio, JCAP **1008**, 004 (2010), arXiv:0907.0018 [astro-ph.CO].

[49] P. J. McMillan, MNRAS **414**, 2446 (2011), arXiv:1102.4340 [astro-ph.GA].

[50] J. Bovy and S. Tremaine, ApJ **756**, 89 (2012), arXiv:1205.4033 [astro-ph.GA].

[51] F. Iocco, M. Pato, G. Bertone, and P. Jetzer, JCAP **1111**, 029 (2011), arXiv:1107.5810 [astro-ph.GA].

[52] J. F. Navarro, C. S. Frenk, and S. D. White, ApJ **490**, 493 (1997), arXiv:astro-ph/9611107 [astro-ph].

[53] A. Burkert, ApJ **447**, 25 (1995), arXiv:astro-ph/9504041 [astro-ph].

[54] J. Einasto, Trudy Astrozicheskogo Instituta Alma-Ata **5**, 87 (1965).

[55] J. An and H. Zhao, MNRAS **428**, 2805 (2012), arXiv:1209.6220 [astro-ph.CO].

[56] M. Kuhlen, J. Diemand, and P. Madau, ApJ **686**, 262 (2008), arXiv:0805.4416 [astro-ph].

[57] L. E. Strigari, S. M. Koushiappas, J. S. Bullock, M. Kaplinghat, J. D. Simon, *et al.*, ApJ **678**, 614 (2008), arXiv:0709.1510 [astro-ph].

[58] M. G. Walker and J. Penarrubia, ApJ **742**, 20 (2011), arXiv:1108.2404 [astro-ph.CO].

[59] A. A. Klypin, A. V. Kravtsov, O. Valenzuela, and F. Prada, ApJ **522**, 82 (1999), arXiv:astro-ph/9901240 [astro-ph].

[60] B. Moore, S. Ghigna, F. Governato, G. Lake, T. R. Quinn, *et al.*, ApJ **524**, L19 (1999), arXiv:astro-ph/9907411 [astro-ph].

[61] L. E. Strigari, J. S. Bullock, M. Kaplinghat, J. Diemand, M. Kuhlen, *et al.*, ApJ **669**, 676 (2007), arXiv:0704.1817 [astro-ph].

[62] A. V. Kravtsov, Adv.Astron. **2010**, 281913 (2010), arXiv:0906.3295 [astro-ph.CO].

[63] M. G. Walker, M. Mateo, E. W. Olszewski, J. Penarrubia, N. Evans, *et al.*, ApJ **704**, 1274 (2009), arXiv:0906.0341 [astro-ph.CO].

[64] J. Wolf, G. D. Martinez, J. S. Bullock, M. Kaplinghat, M. Geha, *et al.*, MNRAS **406**, 1220 (2010), arXiv:0908.2995 [astro-ph.CO].

[65] T. Sjöstrand, S. Mrenna, and P. Z. Skands, Comput.Phys.Commun. **178**, 852 (2008), arXiv:0710.3820 [hep-ph].

[66] J. F. Beacom, N. F. Bell, and G. Bertone, Phys.Rev.Lett. **94**, 171301 (2005), arXiv:astro-ph/0409403 [astro-ph].

[67] A. Birkedal, K. T. Matchev, M. Perelstein, and A. Spray, (2005), arXiv:hep-ph/0507194 [hep-ph].

[68] J. R. Primack, D. Seckel, and B. Sadoulet, Ann.Rev.Nucl.Part.Sci. **38**, 751 (1988).

[69] G. Steigman, B. Dasgupta, and J. F. Beacom, Phys.Rev. **D86**, 023506 (2012), arXiv:1204.3622 [hep-ph].

[70] R. E. Smith and K. Markovic, Phys.Rev. **D84**, 063507 (2011), arXiv:1103.2134 [astro-ph.CO].

[71] A. Boyarsky, J. Lesgourgues, O. Ruchayskiy, and M. Viel, JCAP **0905**, 012 (2009), arXiv:0812.0010 [astro-ph].

[72] A. Boyarsky, O. Ruchayskiy, and D. Iakubovskyi, JCAP **0903**, 005 (2009), arXiv:0808.3902 [hep-ph].

[73] K. Griest and M. Kamionkowski, Phys.Rev.Lett. **64**, 615 (1990).

[74] B. W. Lee and S. Weinberg, Phys.Rev.Lett. **39**, 165 (1977).

[75] M. Mateo, Ann.Rev.Astron.Astrophys. **36**, 435 (1998), arXiv:astro-ph/9810070 [astro-ph].

[76] J. Grcevich and M. E. Putman, ApJ **696**, 385 (2009), arXiv:0901.4975 [astro-ph.GA].

[77] E. J. Tollerud, J. S. Bullock, L. E. Strigari, and B. Willman, ApJ **688**, 277 (2008), arXiv:0806.4381 [astro-ph].

[78] A. A. Moiseev, R. Hartman, J. Ormes, D. Thompson, M. Amato, *et al.*, Astropart.Phys. **27**, 339 (2007), arXiv:astro-ph/0702581 [ASTRO-PH].

[79] W. Atwood, R. Bagagli, L. Baldini, R. Bellazzini, G. Barbiellini, *et al.*, Astropart. Phys. **28**, 422 (2007).

[80] P. Bruel, J.Phys.Conf.Ser. **404**, 012033 (2012), arXiv:1210.2558 [astro-ph.IM].

[81] M. Ackermann *et al.* (Fermi-LAT Collaboration), ApJS **203**, 4 (2012), arXiv:1206.1896 [astro-ph.IM].

[82] L. Breiman, J. Friedman, C. J. Stone, and R. Olshen, *Classification and Regression Trees* (Chapman and Hall/CRC, 1984).

[83] M. Bartlett, Biometrika **40**, 306 (1953).

[84] J. Neyman and E. Pearson, Phil. Trans. R. Soc. A **231**, 289 (1933).

[85] S. S. Wilks, Ann.Math.Statist. **9**, 60 (1938).

[86] H. Chernoff, Ann.Math.Statist. **25**, 573 (1954).

[87] A. Abdo *et al.* (Fermi-LAT Collaboration), ApJS **188**, 405 (2010), arXiv:1002.2280 [astro-ph.HE].

[88] J. Neyman, Phil. Trans. R. Soc. A **236**, 333 (1937).

[89] O. Helene, Nucl.Instrum.Meth. **212**, 319 (1983).

[90] G. J. Feldman and R. D. Cousins, Phys.Rev. **D57**, 3873 (1998), arXiv:physics/9711021 [physics.data-an].

[91] B. P. Roe and M. B. Woodroofe, Phys.Rev. **D60**, 053009 (1999), arXiv:physics/9812036 [physics].

[92] W. A. Rolke, A. M. Lopez, and J. Conrad, Nucl.Instrum.Meth. **A551**, 493 (2005), arXiv:physics/0403059 [physics].

[93] M. Ackermann *et al.* (Fermi-LAT Collaboration), Phys.Rev.Lett. **107**, 241302 (2011), arXiv:1108.3546 [astro-ph.HE].

[94] A. Abdo *et al.* (Fermi-LAT Collaboration), ApJ **712**, 147 (2010), arXiv:1001.4531 [astro-ph.CO].

[95] P. Scott, J. Conrad, J. Edsjo, L. Bergstrom, C. Farnier, *et al.*, JCAP **1001**, 031 (2010), arXiv:0909.3300 [astro-ph.CO].

[96] A. Geringer-Sameth and S. M. Koushiappas, Phys.Rev.Lett. **107**, 241303 (2011), arXiv:1108.2914 [astro-ph.CO].

[97] M. Mazziotta, F. Loparco, F. de Palma, and N. Giglietto, Astropart. Phys. **37**, 26 (2012), arXiv:1203.6731 [astro-ph.IM].

[98] A. Geringer-Sameth and S. M. Koushiappas, Phys.Rev. **D86**, 021302 (2012), arXiv:1206.0796 [astro-ph.HE].

[99] A. Baushev, S. Federici, and M. Pohl, Phys.Rev. **D86**, 063521 (2012), arXiv:1205.3620 [astro-ph.HE].

[100] Y.-L. S. Tsai, Q. Yuan, and X. Huang, JCAP **1303**, 018 (2013), arXiv:1212.3990 [astro-ph.HE].

[101] J. Binney and S. Tremaine, *Galactic Dynamics* (Princeton University Press, 2008).

[102] N. Evans, F. Ferrer, and S. Sarkar, Phys.Rev. **D69**, 123501 (2004), arXiv:astro-ph/0311145 [astro-ph].

[103] G. D. Martinez, J. S. Bullock, M. Kaplinghat, L. E. Strigari, and R. Trotta, JCAP **0906**, 014 (2009), arXiv:0902.4715 [astro-ph.HE].

[104] A. Charbonnier, C. Combet, M. Daniel, S. Funk, J. Hinton, *et al.*, MNRAS **418**, 1526 (2011), arXiv:1104.0412 [astro-ph.HE].

[105] G. D. Martinez *et al.*, (2013), in preparation.

[106] S. E. Koposov, G. Gilmore, M. Walker, V. Belokurov, N. W. Evans, *et al.*, ApJ **736**, 146 (2011), arXiv:1105.4102 [astro-ph.GA].

[107] J. D. Simon and M. Geha, ApJ **670**, 313 (2007), arXiv:0706.0516 [astro-ph].

[108] M. Kuhlen, P. Madau, and J. Silk, Science **325**, 970 (2009), arXiv:0907.0005 [astro-ph.GA].

[109] J. D. Simon, M. Geha, Q. E. Minor, G. D. Martinez, E. N. Kirby, *et al.*, ApJ **733**, 46 (2011), arXiv:1007.4198 [astro-ph.GA].

[110] T. E. Jeltema and S. Profumo, JCAP **0811**, 003 (2008), arXiv:0808.2641 [astro-ph].

[111] F. James and M. Roos, Comput.Phys.Commun. **10**, 343 (1975).

[112] N. F. Bell, J. B. Dent, T. D. Jacques, and T. J. Weiler, Phys.Rev. **D78**, 083540 (2008), arXiv:0805.3423 [hep-ph].

[113] P. Ciafaloni, D. Comelli, A. Riotto, F. Sala, A. Strumia, *et al.*, JCAP **1103**, 019 (2011), arXiv:1009.0224 [hep-ph].

[114] J. Bregeon *et al.* (Fermi-LAT Collaboration), (2013), arXiv:1304.5456 [astro-ph.HE].

[115] M. Ackermann *et al.* (Fermi-LAT Collaboration), In preparation.

[116] P. Nolan *et al.* (Fermi-LAT Collaboration), ApJS **199**, 31 (2012), arXiv:1108.1435 [astro-ph.HE].

[117] M. P. Hobson, A. H. Jaffe, A. R. Liddle, P. Mukeherjee, and D. Parkinson, *Bayesian Methods in Cosmology* (2010).

[118] J. Diemand, M. Kuhlen, and P. Madau, ApJ **657**, 262 (2007), arXiv:astro-ph/0611370 [astro-ph].

[119] S. Koposov, V. Belokurov, N. Evans, P. Hewett, M. Irwin, *et al.*, ApJ **686**, 279 (2008), arXiv:0706.2687 [astro-ph].

[120] J. Skilling, in *American Institute of Physics Conference Series*, American Institute of Physics Conference Series, Vol. 735, edited by R. Fischer, R. Preuss, and U. V. Toussaint (2004) pp. 395–405.

[121] J. Mattox, D. Bertsch, J. Chiang, B. Dingus, S. Digel, *et al.*, ApJ **461**, 396 (1996).

[122] M. Su, T. R. Slatyer, and D. P. Finkbeiner, ApJ **724**, 1044 (2010), arXiv:1005.5480 [astro-ph.HE].

[123] M. Su and D. P. Finkbeiner, ApJ **753**, 61 (2012), arXiv:1205.5852 [astro-ph.HE].

[124] . F. Aharonian (HESS Collaboration), Astropart. Phys. **29**, 55 (2008), arXiv:0711.2369 [astro-ph].

[125] P. M. Frinchaboy, S. R. Majewski, R. R. Munoz, D. R. Law, E. L. Lokas, *et al.*, ApJ **756**, 74 (2012), arXiv:1207.3346 [astro-ph.GA].

[126] M. Dall'Ora, G. Clementini, K. Kinemuchi, V. Ripepi, M. Marconi, *et al.*, ApJ **653**, L109 (2006), arXiv:astro-ph/0611285 [astro-ph].

[127] M. G. Walker, M. Mateo, and E. Olszewski, AJ **137**, 3100 (2009), arXiv:0811.0118 [astro-ph].

[128] R. R. Muñoz, P. M. Frinchaboy, S. R. Majewski, J. R. Kuhn, M.-Y. Chou, *et al.*, ApJ **631**, L137 (2005), arXiv:astro-ph/0504035 [astro-ph].

[129] M. Mateo, E. W. Olszewski, and M. G. Walker, ApJ **675**, 201 (2007), arXiv:0708.1327 [astro-ph].

[130] A. Koch, J. Kleyna, M. Wilkinson, E. Grebel, G. Gilmore, *et al.*, AJ **134**, 566 (2007), arXiv:0704.3437 [astro-ph].

[131] B. Willman, M. Geha, J. Strader, L. E. Strigari, J. D. Simon, *et al.*, AJ **142**, 128 (2011), arXiv:1007.3499 [astro-ph.GA].

[132] L. Demortier, *PHYSTAT 2003 Proceedings*, eConf **C030908**, WEMT003 (2003), arXiv:physics/0312100 [physics].

[133] E. Gross (ATLAS Collaboration), "Frequentist Limit Recommendation," ATLAS Statistics Forum (2011).

[134] F. de Palma, T. Brandt, G. Johannesson, and L. Tibaldo (Fermi-LAT Collaboration), (2013), arXiv:1304.1395 [astro-ph.HE].

[135] M. Ackermann *et al.* (Fermi-LAT Collaboration), ApJ **750**, 3 (2012), arXiv:1202.4039 [astro-ph.HE].

[136] J.-M. Casandjian and I. Grenier (Fermi-LAT Collaboration), (2009), arXiv:0912.3478 [astro-ph.HE].

[137] M. Wolleben, ApJ **664**, 349 (2007), arXiv:0704.0276 [astro-ph].

[138] R. Cotta, A. Drlica-Wagner, S. Murgia, E. Bloom, J. Hewett, *et al.*, JCAP **1204**, 016 (2012), arXiv:1111.2604 [hep-ph].

[139] A. H. Chamseddine, R. L. Arnowitt, and P. Nath, Phys.Rev.Lett. **49**, 970 (1982).

[140] G. L. Kane, C. F. Kolda, L. Roszkowski, and J. D. Wells, Phys.Rev. **D49**, 6173 (1994), arXiv:hep-ph/9312272 [hep-ph].

[141] C. F. Berger, J. S. Gainer, J. L. Hewett, and T. G. Rizzo, JHEP **0902**, 023 (2009), arXiv:0812.0980 [hep-ph].

[142] A. Djouadi, J.-L. Kneur, and G. Moultaka, Comput.Phys.Commun. **176**, 426 (2007), arXiv:hep-ph/0211331 [hep-ph].

[143] G. D'Ambrosio, G. Giudice, G. Isidori, and A. Strumia, Nucl.Phys. **B645**, 155 (2002), arXiv:hep-ph/0207036 [hep-ph].

[144] R. Cotta, K. Howe, J. Hewett, and T. Rizzo, Phys.Rev. **D85**, 035017 (2012), arXiv:1105.1199 [hep-ph].

[145] E. Komatsu *et al.* (WMAP Collaboration), ApJS **180**, 330 (2009), arXiv:0803.0547 [astro-ph].

[146] P. Gondolo, J. Edsjo, P. Ullio, L. Bergstrom, M. Schelke, *et al.*, JCAP **0407**, 008 (2004), arXiv:astro-ph/0406204 [astro-ph].

[147] T. Bringmann, L. Bergstrom, and J. Edsjo, JHEP **0801**, 049 (2008), arXiv:0710.3169 [hep-ph].

[148] V. Barger, Y. Gao, W. Y. Keung, and D. Marfatia, Phys.Rev. **D80**, 063537 (2009), arXiv:0906.3009 [hep-ph].

[149] H. Goldberg, Phys.Rev.Lett. **50**, 1419 (1983).

[150] R. Cotta, J. Conley, J. Gainer, J. Hewett, and T. Rizzo, JHEP **1101**, 064 (2011), arXiv:1007.5520 [hep-ph].

[151] L. Bergstrom, Phys.Lett. **B225**, 372 (1989).

[152] J. A. Conley, J. S. Gainer, J. L. Hewett, M. P. Le, and T. G. Rizzo, Eur.Phys.J. **C71**, 1697 (2011), arXiv:1009.2539 [hep-ph].

[153] J. A. Conley, J. S. Gainer, J. L. Hewett, M. P. Le, and T. G. Rizzo, (2011), arXiv:1103.1697 [hep-ph].

[154] R. Cotta, J. Gainer, J. Hewett, and T. Rizzo, New J.Phys. **11**, 105026 (2009), arXiv:0903.4409 [hep-ph].

[155] N. Kaiser, H. Aussel, H. Boesgaard, K. Chambers, J. N. Heasley, *et al.*, Proc.SPIE Int.Soc.Opt.Eng. **4836**, 154 (2002).

[156] T. Abbott *et al.* (DES Collaboration), (2005), arXiv:astro-ph/0510346 [astro-ph].

[157] B. Anderson, M. Kuhlen, J. Diemand, R. P. Johnson, and P. Madau, ApJ **718**, 899 (2010), arXiv:1006.1628 [astro-ph.HE].

[158] E. Aprile *et al.* (XENON100 Collaboration), Phys.Rev.Lett. **105**, 131302 (2010), arXiv:1005.0380 [astro-ph.CO].

[159] D. McKinsey, D. Akerib, S. Bedikian, A. Bernstein, A. Bolozdynya, *et al.*, J.Phys.Conf.Ser. **203**, 012026 (2010).

[160] T. Bruch (CDMS Collaboration), (2010), arXiv:1001.3037 [astro-ph.IM].

[161] J. Collar, C. E. Dahl, D. Fustin, A. Robinson, E. Behnke, *et al.*, (2010), `www-coupp.fnal.gov/public/500kg%20PAC%20Proposal.pdf`.

[162] J. Braun and D. Hubert (IceCube Collaboration), (2009), arXiv:0906.1615 [astro-ph.HE].

[163] R. Abbasi *et al.* (IceCube Collaboration), Phys.Rev.Lett. **102**, 201302 (2009), arXiv:0902.2460 [astro-ph.CO].

[164] E. Behnke, J. Behnke, S. Brice, D. Broemmelsiek, J. Collar, *et al.*, Phys.Rev.Lett. **106**, 021303 (2011), arXiv:1008.3518 [astro-ph.CO].

[165] C. Wiebusch (IceCube Collaboration), (2009), arXiv:0907.2263 [astro-ph.IM].

[166] M. Ackermann *et al.* (Fermi-LAT Collaboration), ApJ **747**, 121 (2012), arXiv:1201.2691 [astro-ph.HE].

[167] S. Hofmann, D. J. Schwarz, and H. Stoecker, Phys.Rev. **D64**, 083507 (2001), arXiv:astro-ph/0104173 [astro-ph].

[168] A. Loeb and M. Zaldarriaga, Phys.Rev. **D71**, 103520 (2005), arXiv:astro-ph/0504112 [astro-ph].

[169] A. Tasitsiomi and A. Olinto, Phys.Rev. **D66**, 083006 (2002), arXiv:astro-ph/0206040 [astro-ph].

[170] S. M. Koushiappas, A. R. Zentner, and T. P. Walker, Phys.Rev. **D69**, 043501 (2004), arXiv:astro-ph/0309464 [astro-ph].

[171] L. Pieri, G. Bertone, and E. Branchini, MNRAS. **384**, 1627 (2008), arXiv:0706.2101 [astro-ph].

[172] E. Baltz, B. Berenji, G. Bertone, L. Bergstrom, E. Bloom, *et al.*, JCAP **0807**, 013 (2008), arXiv:0806.2911 [astro-ph].

[173] V. Springel, S. White, C. Frenk, J. Navarro, A. Jenkins, *et al.*, Nature **456N7218**, 73 (2008).

[174] A. Abdo *et al.* (Fermi-LAT Collaboration), ApJ **753**, 83 (2012), arXiv:1108.1202 [astro-ph.HE].

[175] C. Tyler, Phys.Rev. **D66**, 023509 (2002), arXiv:astro-ph/0203242 [astro-ph].

[176] J. F. Navarro, A. Ludlow, V. Springel, J. Wang, M. Vogelsberger, S. D. M. White, A. Jenkins, C. S. Frenk, and A. Helmi, MNRAS **402**, 21 (2010).

[177] P. Madau, J. Diemand, and M. Kuhlen, ApJ **679**, 1260 (2008), arXiv:0802.2265 [astro-ph].

[178] M. Geha, B. Willman, J. D. Simon, L. E. Strigari, E. N. Kirby, *et al.*, ApJ **692**, 1464 (2009), arXiv:0809.2781 [astro-ph].

[179] P. Wang, Ph.D. Thesis, Stanford University (2011).

[180] A. Abdo *et al.* (Fermi-LAT Collaboration), ApJ **712**, 459 (2010), arXiv:1002.2198 [astro-ph.HE].

[181] M.-H. Grondin, S. Funk, M. Lemoine-Goumard, A. Van Etten, J. Hinton, *et al.*, ApJ **738**, 42 (2011), arXiv:1106.0184 [astro-ph.HE].

[182] K. M. Górski, E. Hivon, A. J. Banday, B. D. Wandelt, F. K. Hansen, M. Reinecke, and M. Bartelmann, ApJ **622**, 759 (2005), arXiv:astro-ph/0409513.

[183] L. E. Strigari, S. M. Koushiappas, J. S. Bullock, and M. Kaplinghat, Phys.Rev. **D75**, 083526 (2007), arXiv:astro-ph/0611925 [astro-ph].

[184] J. Lande, M. Ackermann, *et al.*, ApJ **756**, 5 (2012), arXiv:1207.0027 [astro-ph.HE].

[185] A. Cesarini, F. Fucito, A. Lionetto, A. Morselli, and P. Ullio, Astropart. Phys. **21**, 267 (2004), arXiv:astro-ph/0305075 [astro-ph].

[186] M. R. Buckley and D. Hooper, Phys.Rev. **D82**, 063501 (2010), arXiv:1004.1644 [hep-ph].

[187] J. W. Hessels, M. S. Roberts, M. A. McLaughlin, P. S. Ray, P. Bangale, *et al.*, AIP Conf.Proc. **1357**, 40 (2011), arXiv:1101.1742 [astro-ph.HE].

[188] A. Abdo *et al.* (Fermi-LAT Collaboration), ApJ **715**, 429 (2010), arXiv:1002.0150 [astro-ph.HE].

[189] A. Abdo *et al.* (Fermi-LAT Collaboration), ApJS **187**, 460 (2010), arXiv:0910.1608 [astro-ph.HE].

[190] E. Bonamente, Ph.D. Thesis, Universita degli Studi di Perugia (2010).

[191] M. Ackermann *et al.* (Fermi-LAT Collaboration), ApJ **726**, 35 (2011), arXiv:1011.2076 [astro-ph.HE].

[192] M. Ackermann *et al.* (Fermi-LAT Collaboration), (2013), arXiv:1305.5597 [astro-ph.HE].

[193] M. Sanchez-Conde, A. Klein, Q. Zeng, A. Drlica-Wagner, E. Bloom, S. Funk, F. Massaro, and M. Wood, *Fermi Cycle-6* GI proposal.

[194] D. G. York *et al.* (SDSS Collaboration), AJ **120**, 1579 (2000), arXiv:astro-ph/0006396 [astro-ph].

[195] B. Willman, Adv.Astron. **2010**, 285454 (2010), arXiv:0907.4758 [astro-ph.CO].

[196] K. N. Abazajian *et al.* (SDSS Collaboration), ApJS **182**, 543 (2009), arXiv:0812.0649 [astro-ph].

[197] S. Walsh, B. Willman, and H. Jerjen, AJ **137**, 450 (2009), arXiv:0807.3345 [astro-ph].

[198] B. Willman, F. Governato, J. Dalcanton, D. Reed, and T. R. Quinn, MNRAS. **353**, 639 (2004), arXiv:astro-ph/0403001 [astro-ph].

[199] S. Keller, B. Schmidt, and M. Bessell, PASA **24**, 1 (2007), arXiv:0704.1339 [astro-ph].

[200] Z. Ivezic, J. Tyson, R. Allsman, J. Andrew, and R. Angel (LSST Collaboration), (2008), arXiv:0805.2366 [astro-ph].

[201] W. Atwood *et al.* (Fermi-LAT Collaboration), (2013), arXiv:1303.3514 [astro-ph.IM].

[202] L. Rochester, T. Usher, R. P. Johnson, and B. Atwood, (2010), arXiv:1001.5005 [astro-ph.IM].

[203] R. Frühwirth, *Data Analysis Techniques for High-Energy Physics*, Cambridge Monographs on Particle Physics, Nuclear Physics and Cosmology (Cambridge University Press, 2000).

[204] J. C. Gower and G. J. S. Ross, Appl.Stats. **18**, 54 (1969).

[205] A. Hoecker, J. Stelzer, F. Tegenfeldt, H. Voss, K. Voss, *et al.*, PoS **ACAT**, 040 (2007), arXiv:physics/0703039 [PHYSICS].

[206] V. Pelassa, R. Preece, F. Piron, N. Omodei, and S. Guiriec (Fermi-LAT Collaboration, GBM Collaboration), (2010), arXiv:1002.2617 [astro-ph.HE].

[207] P. Goldreich and D. A. Keeley, ApJ **170**, 463 (1971).

[208] D. B. Cline and W. Hong, Astropart.Phys. **5**, 175 (1996).

[209] C. N. Yang, Physical Review **77**, 722 (1950).

[210] A. Drlica-Wagner and E. Charles (Fermi-LAT Collaboration), (2011), arXiv:1111.2352 [astro-ph.IM].

[211] W. Atwood, in *Advances in Machine Learning and Data Mining for Astronomy*, edited by M. J. W. Way, J. D. Scargle, K. M. Ali, and A. N. Srivastava (Chapman and Hall/CRC, 2012).

[212] R. Brun and F. Rademakers, Nucl.Instrum.Meth. **A389**, 81 (1997).

[213] A. Abdo *et al.* (Fermi-LAT Collaboration), Phys.Rev.Lett. **102**, 181101 (2009), arXiv:0905.0025 [astro-ph.HE].

[214] M. Ackermann *et al.* (Fermi-LAT Collaboration), Phys.Rev. **D82**, 092004 (2010), arXiv:1008.3999 [astro-ph.HE].

[215] M. Ackermann *et al.* (Fermi-LAT Collaboration), Phys.Rev.Lett. **108**, 011103 (2012), arXiv:1109.0521 [astro-ph.HE].

[216] M. E. Monzani *et al.* (Fermi-LAT Collaboration), in *AAS/High Energy Astrophysics Division #11*, Bulletin of the AAS, Vol. 42 (2010) p. 716.